STUDY OF CLOUD PROPERTIES FROM SINGLE–SCATTERING, RADIATIVE FORCING, AND RETRIEVAL PERSPECTIVES

A Dissertation

by

YONG-KEUN LEE

Submitted to the Office of Graduate Studies of
Texas A&M University
in partial fulfillment of the requirements for the degree of

DOCTOR OF PHILOSOPHY

August 2006

Major Subject: Atmospheric Sciences

STUDY OF CLOUD PROPERTIES FROM SINGLE–SCATTERING, RADIATIVE FORCING, AND RETRIEVAL PERSPECTIVES

A Dissertation

by

YONG-KEUN LEE

Submitted to the Office of Graduate Studies of
Texas A&M University
in partial fulfillment of the requirements for the degree of

DOCTOR OF PHILOSOPHY

Approved by:

Chair of Committee,	Ping Yang
Committee Members,	Thomas Wilheit
	Gerald North
	George W. Kattawar
	Hung-Lung Huang
Head of Department,	Richard Orville

August 2006

Major Subject: Atmospheric Sciences

ABSTRACT

Study of Cloud Properties from Single-scattering, Radiative Forcing,

and Retrieval Perspectives. (August 2006)

Yong-Keun Lee, B.S., Seoul National University;

M.S., Seoul National University

Chair of Advisory Committee: Dr. Ping Yang

This dissertation reports on three different yet related topics in light scattering computation, radiative transfer simulation, and remote sensing implementation, regarding the cloud properties and the retrieval of cloud properties from satellite-based infrared radiometric measurements. First, the errors associated with the use of circular cylinders as surrogates for hexagonal columns in computing the optical properties of pristine ice crystals at infrared (8-12 μm) wavelengths are investigated. It is found that the differences between the results for circular cylinders and hexagonal columns are on the order of a few percent at infrared wavelengths. Second, investigated in this dissertation are the outgoing broadband longwave and window channel radiances at the top-of-atmosphere under clear-sky conditions on the basis of the data acquired by the Cloud and the Earth's Radiant Energy System (CERES) instrument onboard the NASA Terra satellite platform. Based on the comparison of the observed broadband radiances with those obtained from rigorous radiative transfer simulations, it is found that the theoretical results tend to be larger than their measured counterparts. Extensive

sensitivity studies regarding the uncertainties of various parameters were carried out. Within the considered uncertainties of various factors, the computed radiances are still larger than the observed radiances if thin cirrus clouds are excluded. Thus, a potential cause for the differences could be associated with the presence of thin cirrus clouds whose visible optical thickness is smaller than approximately 0.3. Third, presented in this dissertation is an illustration of the application of hyperspectral infrared channel observations to the retrieval of the cloud properties. Specifically, the hyperspectral measurements acquired from the Atmospheric Infrared Sounder (AIRS) aboard the NASA Aqua platform are used to infer cloud top pressure, effective cloud amount, cloud thermodynamic phase, cloud optical thickness, and the effective size of cloud particles. The AIRS-based retrievals are compared with the counterparts of the operational cloud products derived from the Moderate Resolution Imaging Spectroradiometer (MODIS). The two retrievals agree reasonably well except for the retrieved cloud effective particle size. Furthermore, the diurnal and seasonal contrasts of cloud properties are also investigated on the basis of the cloud properties retrieved from the AIRS data.

DEDICATION

This dissertation is dedicated to my friends and family who have always helped and supported me throughout my life.

ACKNOWLEDGEMENTS

I would like to thank my advisor, Dr. Ping Yang, for his guidance and support. I would like to thank him for giving me the opportunity to continue my education, and for the encouragement to continue further. I would also like to thank Heli Wei who offered a lot of help throughout this project. Without him, this study would never have been completed. I would like to thank the members of my committee, Dr. Thomas Wilheit, Dr. Gerald North, Dr. George Kattawar, and Dr. Hung-Lung Huang, for supporting my research and for giving their time to edit this dissertation.

This study was supported by the National Science Foundation Physical Meteorology Program managed by Dr. Andrew Detwiler (ATM-0239605), the NASA Radiation Sciences Program managed by Dr. Hal Maring (previously by Dr. Donald Anderson) (NNG04GL24G), and a subcontract (G066010) issued by the University of Wisconsin-Madison to Texas A&M University.

Data were obtained from the NASA Goddard Earth Science (GES) Distributed Active Archive Center (DAAC).

Finally, I would like to thank my family and friends for all their support throughout the years. I would like to thank my wife, WonSil Song, for all her love, support, and encouragement.

TABLE OF CONTENTS

Page

ABSTRACT…….. iii

DEDICATION…….. v

ACKNOWLEDGEMENTS…….. vi

TABLE OF CONTENTS…….. vii

LIST OF FIGURES…… ix

LIST OF TABLES…… xiv

CHAPTER

I INTRODUCTION…… 1

II USE OF CIRCULAR CYLINDERS AS SURROGATES FOR HEXAGONAL PRISTINE ICE CRYSTALS IN SCATTERING CALCULATIONS AT INFRARED WAVELENGTHS ..……. 3

2.1 Background…… 3
2.2 Approach…… 6
2.3 Numerical results and discussions……...…. 17

III POTENTIAL NIGHTTIME CONTAMINATION OF CERES CLEAR-SKY FIELDS OF VIEW BY OPTICALLY THIN CIRRUS DURING THE CRYSTAL-FACE CAMPAIGN…….…… 33

3.1 Background…… 33
3.2 Data and methodology…….. 34
3.3 Results…….……. 43
3.4 Sensitivity study……..... 56

IV RETRIEVAL OF CLOUD PROPERTIES USING ATMOSPHERIC INFRARED SOUNDER (AIRS) ……...… 62

CHAPTER Page

4.1 Background……. 62
4.2 Data availability and method……..… 64
4.2.1 AIRS products……. 64
4.2.2 Single scattering properties of ice and water clouds…… 66
4.2.3 Lookup libraries of transmittance and reflectance for ice and water clouds……. 69
4.2.4 One layer FIRTM……...……. 73
4.2.5 Determination of cloud properties…….……. 82
4.2.6 The simulated annealing method ……..……. 89
4.3 Results…….……...……..... 93
4.3.1 Retrieval of cloud properties derived from AIRS observations and comparison with the corresponding MODIS products …… 93
4.3.2 Diurnal and seasonal contrast of cloud properties …….. 107

V CONCLUSIONS…… 144

5.1 Use of circular cylinders as surrogates for hexagonal pristine ice crystals in scattering calculations at infrared wavelengths …….. 144
5.2 Potential nighttime contamination of CERES clear-sky fields of view by optically thin cirrus during the CRYSTAL-FACE campaign ……..…… 146
5.3 Retrieval of cloud properties using Atmospheric Infrared Sounder (AIRS) data …….……..... 148

REFERENCES…….…….. 151

VITA…….…. 169

LIST OF FIGURES

FIGURE Page

2.1 The radii and lengths of circular cylinders defined as having the same volume, surface area, or the ratio of volume to surface area as hexagonal columns, when the same length or aspect ratio is applied to the two geometries. The left panel is for the case when the lengths of circular cylinders and hexagonal columns are the same. The middle and right panels are for the case when the aspect ratio is kept as constant in defining the equivalence..... 16

2.2 The comparison of phase functions of circular cylinders and hexagonal columns. The circular cylinders are defined to have the same volume and length as hexagonal columns. The results for circular cylinders are computed by using Mishchenko's T-matrix code [1991]. For hexagonal columns, the finite-difference time domain method is used for small particles (L=10, 20 and 40 μm) whereas an improved geometric optics method is used for L=140 μm..... 18

2.3 The comparison of the extinction efficiencies at a wavelength of 8.5 μm for hexagonal columns and various equivalent circular cylinders. The results for hexagonal particles are taken from *Yang et al.* [2001]..... 21

2.4 The absorption efficiencies corresponding to the extinction efficiencies shown in Fig. 2.3..... 22

2.5 The asymmetry factors corresponding to the efficiencies shown in Figs. 2.3 and 2.4. 23

2.6 Same as Fig. 2.3, except the calculations are performed at a wavelength of 11 μm..... 26

2.7 Same as Fig. 2.4, except the calculations are performed at a wavelength of 11 μm..... 27

2.8 Same as Fig. 2.5, except the calculations are performed at a wavelength of 11 μm..... 28

FIGURE Page

2.9 Comparison of absorption efficiencies of pristine hexagonal ice columns and aggregate ice crystals. The procedure of computing the optical properties of aggregates is explained in *Yang et al.* [2002]. …….. 30

3.1 Averaged extinction efficiency, absorption efficiency and asymmetry factor for droxtal ice crystals with sizes of 10, 20, 40, and 60 μm in the spectral region from 50 to 2000 cm^{-1}.…….……. 41

3.2 (a) The observed and calculated TOA outgoing longwave band radiances, (b) the relative differences for the computed and observed outgoing longwave band radiances, (c) the window band radiance, (d) relative differences for the computed and observed outgoing window band radiances. CERES FOVs flagged as cloud free have been chosen, which are located within 0.25 degree in both latitude and longitude over 4 atmospheric sounding locations during CRYSTAL-FACE period (July 2002). The error bars are 0.6 $Wm^{-2}Sr^{-1}$ for the LW band CERES measurement and 0.3 $Wm^{-2}Sr^{-1}$ for the WIN band and the error bars are ±0.2% for the LW band and WIN band simulation……..…….. 44

3.3 Similar to Fig. 3.2, except that the x-axis is for the viewing zenith angle in Fig. 3.3…… 45

3.4 Anisotropy factors provided by the CERES SSF products in comparison with the present simulations. Panel (a) is for the longwave band and panel (b) is for the window band…….…… 48

3.5 Optical depths of thin cirrus retrieved from the difference of the observed radiances and the simulated counterparts by assuming various effective particle sizes. Panel (a): retrieval from use of the longwave band data; panel (b) retrieval from use of the window band.….. 50

3.6 Distributions of the optical depths of thin cirrus clouds retrieved from the differences of the observed and simulated radiances by assuming various effective particle sizes. Left panels are based on the longwave band data; right panels are based on the window band data.…… 51

3.7 (a) Clear-srong coverage percent and clear-weak coverage percent and (b) the ratio clear-weak coverage to clear-strong coverage.……. 53

FIGURE Page

3.8 (a) The observed and calculated TOA outgoing longwave band flux, (b) the relative differences for the computed and observed outgoing longwave band flux, (c) the window band flux, (d) relative differences between the computed and observed outgoing window band flux. ……. 54

3.9 (a) The observed and calculated TOA outgoing longwave band radiances, (b) the relative differences for the computed and observed outgoing longwave band radiances, (c) the window band radiance, (d) relative differences between the computed and observed outgoing window band radiances. The radiances are calculated with a bias of ±2% in the surface emissivity. The error bars 0.6 $Wm^{-2}Sr^{-1}$ for the longwave band CERES measurement and 0.3 $Wm^{-2}Sr^{-1}$ for the window band…….. 58

3.10 Similar to Fig. 3.9, except that the radiances are calculated with a bias of ±1 K in the surface temperature……..…….. 59

3.11 Similar to Fig. 3.9, except that the radiances are calculated with a bias of ±1 K in the vertical atmospheric temperature profile. …….. 60

3.12 Similar to Fig. 3.9, except that the radiances are calculated with a bias of ±5% in lower atmospheric water vapor amount in conjunction with a ±50% in upper atmospheric water vapor amount. Biases of the same sign are considered together. (L) indicates the lower troposphere and (U) indicates the upper troposphere……..….. 61

4.1 Mean single scattering properties of ice clouds (left panels) and water clouds (right panels). ……..…….. 68

4.2 The transmittance and reflectance of ice and water clouds ……..……. 74

4.3 Radiative transfer in one layer FIRTM. ……...…….. 77

4.4 Brightness temperature from one layer FIRTM simulations for cloud several optical thickness; τ=0, 1, 3, 5, and 10 on the left panel. The brightness temperature difference between one layer cloud FIRTM and the DISORT simulations for several cloud optical thickness. Vertical profiles of temperature, water vapor from an AIRS FOV are used. Cloud top temperature is assumed as 220 K, and the surface temperature is 307 K. ……..…. 81

FIGURE Page

4.5 Dependence of brightness temperature on ice cloud. Optical thickness (τ) with De = 10 μm (left) and effective particle size (De) with τ=1 (right) using atmospheric environment of a pixel from AIRS granule.…….……. 85

4.6 Flow chart for the retrieval of cloud optical thickness and effective particle size…….. 88

4.7 NEDT (K) at 250 K used in this study……..88

4.8 The accuracy to retrieve the cloud optical thickness (left panel) and effective particle size (right panel) for high clouds (above 440 hPa). Viewing zenith angle less than 30° (10°) for cloud optical thickness (effective particle size) is considered. Among the three solid lines in each panel, two solid lines on the top and bottom are 60 % relative error lines, and the center line represents a line of y=x.……..…… 92

4.9 Retrieved cloud top pressure, effective cloud amount, and cloud phase from AIRS and corresponding MODIS products……..... 95

4.10 Retrieved cloud optical thickness and effective particle size from AIRS and corresponding MODIS products.
For AIRS cloud optical thickness and effective particle size, high cloud (above 440 hPa) is considered.…… 99

4.11 Scatter plots of cloud top pressure, effective cloud amount, cloud optical thickness and effective particle size between AIRS and MODIS. For cloud optical thickness, the viewing zenith angle below 30° is considered, and for effective particle size, the viewing zenith angle below 10° and cloud optical thickness less than 5 are considered …….……..…… 103

4.12 ISCCP cloud classification in *Rossow and Schiffer* [1999]. …… 108

4.13 Distribution of brightness temperature at 10.4 μm as a function of AIRS effective cloud amount..……. 123

4.14 Distribution of cloud optical thickness retrieved from AIRS (upper panel) and MODIS (lower panel) as a function of AIRS brightness temperature at 10.4 μm. Nighttime MODIS is not available. …….. 125

FIGURE Page

4.15 Distribution of cloud optical thickness retrieved from AIRS (upper panel) and MODIS (lower panel) as a function of effective cloud amount. Nighttime MODIS is not available.…….…. 132

4.16 Retrieved cloud fraction from AIRS as a function of effective cloud amount……..…… 138

4.17 Distribution of cloud effective particle size retrieved from AIRS (upper panel) and MODIS (lower panel) as a function of effective cloud amount. Nighttime MODIS is not available. …… 140

LIST OF TABLES

TABLE Page

2.1 Minimum and maximum relative errors of the approximation of hexagonal column by circular cylinder using T-matrix compared to *Yang et al*. [2001]. The upper panel is for calculations performed at a wavelength of 8.5 μm and the lower panel is for calculations performed at 11.0 μm. …….. 29

3.1 The average optical depths of thin cirrus clouds retrieved from the differences of the observed and calculated longwave and window band radiances for four effective diameters. ……. 53

4.1 Number of pixels at daytime and nighttime for spring (sum of 15th March, April, and May) in the selected oceanic region (145-170E, 5S-2N). ……..……. 110

4.2 Number of pixels at daytime and nighttime for summer (sum of 16th June, 15th July, and August) in the selected oceanic region (145-170E, 5S-2N). ……..……. 111

4.3 Number of pixels at daytime and nighttime for autumn (sum of 15th September, October, and November) in the selected oceanic region (145-170E, 5S-2N). ……..……. 114

4.4 Number of pixels at daytime and nighttime for winter (sum of 15th December, January, and February) in the selected oceanic region (145-170E, 5S-2N). ……..……. 115

4.5 Classification of high clouds (above 440 hPa) in the daytime and nighttime by the visible cloud optical thickness (3.6) retrieved from AIRS and corresponding MODIS products…..……. 119

4.6 Classification of high clouds (above 440 hPa) in the daytime and nighttime by the visible cloud optical thickness (1.4) retrieved from AIRS and corresponding MODIS products…..……. 120

4.7 Classification of high clouds (above 440 hPa) in the daytime and nighttime by the effective cloud amount (0.5) retrieved from AIRS and corresponding MODIS products……..……. 121

CHAPTER I

INTRODUCTION

Clouds cover approximately two thirds of the globe and have a significant impact on the earth's climate through their effects on the radiation energy budget of the earth-atmosphere and the terrestrial hydrological cycle. While substantial efforts have been made to investigate clouds, both spatial and temporal scales of cloud formation and their subsequent evolution are not yet well understood. Specifically, simulations based on General Circulation Model (GCM) are significantly affected by the range of cloud parameterization [*Cess et al.*, 1996, 1997]. The amount and vertical structure of clouds cause changes in atmospheric circulations [*Sinha and Shine*, 1995; *Stubenrauch et al.*, 1997]. Heating or cooling can be produced by clouds through their radiative effects [*Stephens and Webster*, 1981; *Stephens et al.*, 1990]. *Moore et al.* [2001] reported that clouds are the single largest source of the uncertainties in the climate sensitivity studies. Although there have been significant improvements in understanding clouds, the uncertainty of climate change associated with cloud feedbacks has apparently not been removed yet and it is a challenge to determine cloud impacts on the climate system [*Moore et al.*, 2001]. Previous studies suggest that accurate information of cloud properties is important for the understanding of atmospheric circulation and the climate.

This dissertation follows the style of *Journal of Geophysical Research*.

Since clouds are global phenomena and using satellite observation data is the only way to get global cloud coverage, the work reported in this dissertation depends largely on satellite observations.

In this dissertation, three distinct aspects of cloud properties are investigated from the perspectives of light scattering computation, radiative transfer simulation and remote sensing implementation. Chapter II reports on the approximation of hexagonal ice crystals as circular cylinders in light scattering computations in a spectral region of 8-12 μm. Chapter III reports on the effects of thin cirrus clouds on the radiance and flux at the top of atmosphere over the Florida region during the CRYSTAL-FACE period. Specifically, the outgoing longwave (5-200 μm) and window (8-12 μm) band radiances under clear sky conditions are investigated. Chapter IV investigates the applicability of hyperspectral infrared measurements to the retrieval of cloud properties. Additionally, the diurnal and seasonal contrasts of cloud properties retrieved from AIRS satellite observations are also investigated. Finally, the conclusions of this study are given in Chapter V.

CHAPTER II

USE OF CIRCULAR CYLINDERS AS SURROGATES FOR HEXAGONAL PRISTINE ICE CRYSTALS IN SCATTERING CALCULATIONS AT INFRARED WAVELENGTHS*

2.1 Background

It is quite challenging to assess quantitatively the radiative effect of cirrus clouds in the atmosphere [*Liou*, 1986; *Stephens et al*., 1990; *Kristjansson et al*., 2000]. One of the major difficulties encountered in modeling the radiative properties of cirrus clouds is that these clouds are almost exclusively composed of nonspherical ice crystals. Although various ice crystal configurations, including hexagonal columns, plates, hollow columns, bullet rosettes, and aggregates, have been observed [*Heymsfield and Iaquinta*, 2000; *Heymsfield et al*., 2002; *Arnott et al*., 1994; *Mitchell et al*., 1996], it is a common practice to assume that the geometry of ice crystals is that of hexagonal columns in climate and remote-sensing applications [*Takano and Liou*, 1989a; *Takano and Liou*, 1989b; *Ebert and Curry*, 1992; *Fu*, 1996]. If a complicated particle shape is approximated with a simpler particle shape, it would decrease demand on computer resources in terms of computing time and memory. In the present study, the accuracy of using circular cylinders as surrogates for the computation of the scattering properties of hexagonal ice crystals at infrared wavelengths is assessed. Hexagonal geometry is

regarded as more complex than the circular cylinder geometry, as the former has a lower degree of symmetry. The accuracy of using a simpler geometry as a surrogate for a more complex geometry in light scattering computation has been investigated in several previous studies. *Liou and Takano* [1994] showed that an equivalent sphere with the same surface area or the same volume does not reproduce the proper single-scattering properties of hexagonal ice crystals at infrared wavelengths. *Chylek and Videen* [1994] also showed that the equivalent spheres of equal volume or equal surface area are not suitable for approximating hexagonal columns or plates. *Macke and Mishchenko* [1996] investigated the accuracy of approximating a hexagonal geometry by using ellipsoidal and circular cylinders in light scattering calculations at visible and near-infrared wavelengths. These authors found substantial differences in light scattering calculations for three geometries (hexagonal, ellipsoidal, and circular cylinder particles) at a nonabsorbing wavelength (e.g., 0.55 μm) and recommended against the substitution of the hexagonal structure by ellipsoidal and circular cylinder geometries. However, for the integrated scattering properties, such as the asymmetry factor at absorbing wavelengths (e.g., 1.6 μm and 3.7 μm), the overall differences between the three geometries are much smaller in magnitude. *Kahnert et al*. [2002] investigated the accuracy of approximating an ensemble of wavelength-sized prisms by spheroids and cylinders in light scattering calculations based on the extended boundary condition method. Their results show that the optical properties of cylinders are closer to those of prisms than spheroids. *Baran et al*. [2002] investigated the accuracy of using a size/shape distribution of randomly oriented circular ice cylinders to simulate scattering from a distribution of randomly

oriented ice aggregates. *Grenfell and Warren* [1999] suggested that a nonspherical particle can be approximated by a collection of monodisperse spheres having the same volume-to-surface area (V/A) ratio. Those authors also carried out intensive validation studies regarding the accuracy of their method for calculating the bulk optical properties of ice crystals and modeling radiative transfer processes involving ice clouds.

Motivated by the computational efficiency of the T-matrix method when it is applied to a circular cylinder geometry with small and moderate size parameters, one may inquire whether a hexagonal geometry can be approximated by a circular cylinder at infrared wavelengths with acceptable errors in the scattering properties. From physical intuition, one may expect that the detailed sharp edges of side faces of a hexagon may not be important in light scattering calculations in the infrared region because of strong absorption within the particle and also the fact that the wavelength is of the same order as the particle size. In addition, in the atmosphere the surface edges of pristine ice crystals may be rounded due to sublimation or riming processes [*Macke and Mishchenko*, 1996]. Thus, an investigation of the scattering properties of circular cylinders may be interesting in its own right. The efficient computation of single-scattering properties for circular cylinders by the T-matrix method may provide the optical properties of small ice crystals and also provide a dataset for constructing the approximate optical properties of large particles based on the composite method developed by *Fu et al.* [1998, 1999], which is one of the most practical approaches available to cover a wide range of size parameters.

2.2 Approach

In the present study the T-matrix computation program developed by *Mishchenko* [1991] is employed to calculate the single-scattering properties of randomly oriented circular cylinders. The documentation of the computational program have been reported previously by *Mishchenko and Travis* [1998]. The T-matrix method pioneered by *Waterman* [1965] can be applied in principle to any arbitrary geometry. The application of the T-matrix method based on the extended boundary condition method for rotationally symmetric shapes can be traced back to the studies of *Wiscombe and Mugnai* [1986], *Barber and Hill* [1990], and *Mishchenko and Travis* [1998]. Recently, the numerical implementation of this method has been extended to other geometries other than axisymmetric particles [*Wriedt and Doicu*, 1998;, *Laitinen and Lumme*, 1998; *Mackowski and Mishchenko*, 1996]. *Havemann and Baran* [2001] employed the T-matrix method to compute the single-scattering properties of hexagonal ice crystals with size parameters up to 40. In the numerical computation, the applicable size parameter region of the T-matrix, if implemented to a non-axisymmetric geometry, is usually narrower when compared to the case for axisymmetric particles. A combination of the T-matrix method and other numerical light scattering computational methods, such as discrete dipole approximation (DDA) and finite difference time domain (FDTD), may shed new light on efficient computation of the optical properties of nonspherical particles [*Mackowski*, 2002; G. *Videen*, personal communication]. In practice, the analytical approach of averaging the effect of particle orientations in the T-matrix method [*Videen*, 2002] can substantially speed up numerical computations.

Here the theoretical basis for the T-matrix method is outlined. The incident, scattered, and internal electromagnetic waves can be expanded in terms of the vector spherical functions as follows:

$$E^{inc}(\mathbf{R}) = \sum_{n=1}^{\infty}\sum_{m=-n}^{n}[a_{mn}M^{*}{}_{mn}(k\mathbf{R}) + b_{mn}N^{*}{}_{mn}(k\mathbf{R})], \tag{2.1}$$

$$E^{sca}(\mathbf{R}) = \sum_{n=1}^{\infty}\sum_{m=-n}^{n}[p_{mn}M_{mn}(k\mathbf{R}) + q_{mn}N_{mn}(k\mathbf{R})], \tag{2.2}$$

$$E^{\mathrm{int}}(\mathbf{R}) = \sum_{n=1}^{\infty}\sum_{m=-n}^{n}[c_{mn}M^{*}{}_{mn}(mk\mathbf{R}) + d_{mn}N^{*}{}_{mn}(mk\mathbf{R})], \tag{2.3}$$

where M_{mn} and N_{mn} are vector spherical functions involving spherical Hankel functions; M^{*}_{mn} and N^{*}_{mn} are similar to M_{mn} and N_{mn} except that the former functions involve spherical Bessel functions instead of spherical Hankel functions; a_{mn} and b_{mn} are the expansion coefficients of the incident wave; p_{mn} and q_{mn} are the expansion coefficients of the scattered wave; c_{mn} and d_{mn} are the expansion coefficients of the internal wave; m is the refractive index of the particle relative to that of the surrounding medium; and **R** is the radius vector from the origin of the reference system. The superscripts “inc”, “sca”, and “int” indicate the “incident”, “scattered”, and “internal” fields, respectively. For the first summation in Eqs. (2.1)-(2.3), n should be truncated at a finite value, although n is infinite in the equation. The relationship between the incident field coefficients and the scattered field coefficients is linear and given by the following equation due to the linearity of Maxwell’s equations and boundary conditions:

$$p_{mn} = \sum_{l=1}^{\infty}\sum_{k=-l}^{l}[a_{kl}T^{11}{}_{mnkl} + b_{kl}T^{12}{}_{mnkl}], \tag{2.4}$$

$$q_{mn} = \sum_{l=1}^{\infty} \sum_{k=-l}^{l} [a_{kl} T^{21}{}_{mnkl} + b_{kl} T^{22}{}_{mnkl}]. \tag{2.5}$$

Eqs. (2.4) and (2.5) can be written in a matrix form as follows:

$$\begin{bmatrix} \mathbf{p} \\ \mathbf{q} \end{bmatrix} = \mathbf{T} \begin{bmatrix} \mathbf{a} \\ \mathbf{b} \end{bmatrix} = \begin{bmatrix} T^{11} & T^{12} \\ T^{21} & T^{22} \end{bmatrix} \begin{bmatrix} \mathbf{a} \\ \mathbf{b} \end{bmatrix}. \tag{2.6}$$

Eq. (2.6) is the main equation in the T-matrix method.

A major merit of the T-matrix method is that the expansion coefficients of the incident, internal and scattered waves are computed with the knowledge of the T-matrix components, and they are related linearly through the T-matrix.

To determine the T-matrix components, one can use the internal wave equation (2.3) expanded in vector spherical functions similar to Eqs. (2.1) and (2.2). The expansion coefficients of the incident wave and the internal wave are related as follows:

$$\begin{bmatrix} \mathbf{a} \\ \mathbf{b} \end{bmatrix} = \begin{bmatrix} Q^{11} & Q^{12} \\ Q^{21} & Q^{22} \end{bmatrix} \begin{bmatrix} \mathbf{c} \\ \mathbf{d} \end{bmatrix}, \tag{2.7}$$

where the elements of the Q matrix are surface integrals over the particle and depend on the particle's features, such as size, shape, and refractive index. By inverting Eq. (2.7) and using (2.6), the relation between the expansion coefficients of the internal and scattered waves can be obtained as follows:

$$\begin{bmatrix} \mathbf{p} \\ \mathbf{q} \end{bmatrix} = -\begin{bmatrix} Q^{*11} & Q^{*12} \\ Q^{*21} & Q^{*22} \end{bmatrix} \begin{bmatrix} \mathbf{c} \\ \mathbf{d} \end{bmatrix}, \tag{2.8}$$

where the elements of the Q^* matrix are surface integrals over the particle. From Eqs. (2.6) and (2.8), the T-matrix is solved as follows:

$$\mathbf{T} = -\mathbf{Q}^* \mathbf{Q}^{-1}. \tag{2.9}$$

From the T-matrix components for an arbitrary orientation of a nonspherical particle, the extinction and scattering cross sections of randomly oriented particles are written as follows:

$$C_{ext} = -\frac{2\pi}{k^2}\mathrm{Re}\sum_{n=1}^{\infty}\sum_{m=-n}^{n}[T^{11}{}_{mnmn} + T^{12}{}_{mnmn}], \tag{2.10}$$

$$C_{sca} = \frac{2\pi}{k^2}\sum_{n=1}^{\infty}\sum_{k=1}^{\infty}\sum_{m=-n}^{n}\sum_{l=-k}^{k}\sum_{i=1}^{2}\sum_{j=1}^{2}[T^{ij}{}_{mnkl}]^2 . \tag{2.11}$$

The extinction and scattering efficiencies are calculated by dividing the extinction and scattering cross sections with the projected surface area of the particle.

The scattering phase matrix for a randomly oriented, rotationally symmetric particle is given by,

$$F(\Theta) = \begin{bmatrix} a_1(\Theta) & b_1(\Theta) & 0 & 0 \\ b_1(\Theta) & a_2(\Theta) & 0 & 0 \\ 0 & 0 & a_3(\Theta) & b_2(\Theta) \\ 0 & 0 & -b_2(\Theta) & a_4(\Theta) \end{bmatrix}, \tag{2.12}$$

where Θ is the scattering angle (the angle between the incident and scattered waves). The phase matrix has eight nonzero elements, of which six are independent. The scattering phase matrix transforms the incident Stokes parameters into scattered parameters. Each element is calculated using the expansion coefficients and generalized spherical functions.

To ascertain the difference of the optical properties between hexagonal and circular cylindrical ice crystals, the extinction efficiency, single-scattering albedo, phase

function, and asymmetry factor calculated by *Yang et al*. [2001] are taken as the reference dataset. In that study the FDTD method is applied to small hexagonal ice crystals with maximum dimensions smaller than 40 μm. For the computation of the asymmetry factor, *Yang et al*. [2001] used a combination of the FDTD method and an improved geometric optics method (for particle sizes larger than 40 μm) to compute the phase function. In the computation of extinction and absorption efficiencies, the stretched scattering potential method (SSPM) is applied to ice crystals with maximum dimensions larger than 40 μm. The SSPM method was used in *Yang and Liou* [2001] to avoid the tunneling effect which may produce significant errors in conventional light scattering computation methods. The SSPM results are refined by the weighted summation of the SSPM, the Lorenz-Mie solution for equivalent spheres, and the geometric optics solution in a manner similar to the composite approach developed by *Fu et al*. [1998]. By combining the FDTD and the refined SSPM solutions, the results computed by *Yang et al*. [2001] encompass ice crystal sizes specified in terms of their maximum dimensions from 1 μm to 10000 μm.

The FDTD method starts with specifying a computational domain to discretize the finite space enclosing the particle, followed by the development of the finite difference equations for time-dependent Maxwell's curl equations given by

$$\nabla \times \mathbf{H}(\mathbf{r},t) = \frac{\varepsilon(\mathbf{r})}{c}\frac{\partial \mathbf{E}(\mathbf{r},t)}{\partial t}, \tag{2.13}$$

$$\nabla \times \mathbf{E}(\mathbf{r},t) = -\frac{1}{c}\frac{\partial \mathbf{H}(\mathbf{r},t)}{\partial t}, \tag{2.14}$$

where $\mathbf{E}(\mathbf{r},t)$ is the electric field, $\mathbf{H}(\mathbf{r},t)$ is the magnetic field, $\varepsilon(\mathbf{r})$ is the permittivity of the dielectric medium, c is the speed of light, and $\mathbf{r}$ is the position vector [*Yee*, 1966; *Taflove*, 1995]. For a 3-dimensional particle, the finite space containing the scatterer is discretized by cubic cells. In the FDTD implementation, the magnetic field components are defined at the center of the cubic cells, and the electric field components are defined at the edges of the cubic cells to calculate the curl equations. In a Cartesian coordinate system, the components of the electric and magnetic fields are given by

$$
\begin{aligned}
&E_x^{n+1}(I,J+\frac{1}{2},K+\frac{1}{2}) \\
&= \exp[-kc\bar{\varepsilon}_i(I,J+\frac{1}{2},K+\frac{1}{2})\Delta t/\bar{\varepsilon}_r(I,J+\frac{1}{2},K+\frac{1}{2})]E_x^n(I,J+\frac{1}{2},K+\frac{1}{2}) \\
&+\{1-\exp[-kc\bar{\varepsilon}_i(I,J+\frac{1}{2},K+\frac{1}{2})\Delta t/\bar{\varepsilon}_r(I,J+\frac{1}{2},K+\frac{1}{2})]\}/[kc\bar{\varepsilon}_i(I,J+\frac{1}{2},K+\frac{1}{2})\Delta t] \\
&\times\{\frac{c\Delta t}{\Delta y}[H_z^{n+\frac{1}{2}}(I,J+1,K+\frac{1}{2})-H_z^{n+\frac{1}{2}}(I,J,K+\frac{1}{2})] \\
&+\frac{c\Delta t}{\Delta z}[H_z^{n+\frac{1}{2}}(I,J+\frac{1}{2},K)-H_z^{n+\frac{1}{2}}(I,J+\frac{1}{2},K+1)]\}
\end{aligned}
$$

$$
\begin{aligned}
&E_y^{n+1}(I+\frac{1}{2},J,K+\frac{1}{2}) \\
&= \exp[-kc\bar{\varepsilon}_i(I+\frac{1}{2},J,K+\frac{1}{2})\Delta t/\bar{\varepsilon}_r(I+\frac{1}{2},J,K+\frac{1}{2})]E_x^n(I+\frac{1}{2},J,K+\frac{1}{2}) \\
&+\{1-\exp[-kc\bar{\varepsilon}_i(I+\frac{1}{2},J,K+\frac{1}{2})\Delta t/\bar{\varepsilon}_r(I+\frac{1}{2},J,K+\frac{1}{2})]\}/[kc\bar{\varepsilon}_i(I+\frac{1}{2},J,K+\frac{1}{2})\Delta t] \\
&\times\{\frac{c\Delta t}{\Delta x}[H_z^{n+\frac{1}{2}}(I,J,K+\frac{1}{2})-H_z^{n+\frac{1}{2}}(I+1,J,K+\frac{1}{2})] \\
&+\frac{c\Delta t}{\Delta z}[H_x^{n+\frac{1}{2}}(I+\frac{1}{2},J,K+1)-H_x^{n+\frac{1}{2}}(I+\frac{1}{2},J,K)]\}
\end{aligned}
$$

$$
\begin{aligned}
&E_z^{n+1}(I+\frac{1}{2},J+\frac{1}{2},K)\\
&=\exp[-kc\bar{\varepsilon}_i(I+\frac{1}{2},J+\frac{1}{2},K)\Delta t/\bar{\varepsilon}_r(I+\frac{1}{2},J+\frac{1}{2},K)]E_x^n(I+\frac{1}{2},J+\frac{1}{2},K)\\
&+\{1-\exp[-kc\bar{\varepsilon}_i(I+\frac{1}{2},J+\frac{1}{2},K)\Delta t/\bar{\varepsilon}_r(I+\frac{1}{2},J+\frac{1}{2},K)]\}/[kc\bar{\varepsilon}_i(I+\frac{1}{2},J+\frac{1}{2},K)\Delta t]\\
&\times\{\frac{c\Delta t}{\Delta y}[H_x^{n+\frac{1}{2}}(I+\frac{1}{2},J,K)-H_x^{n+\frac{1}{2}}(I+\frac{1}{2},J+1,K)]\\
&+\frac{c\Delta t}{\Delta x}[H_y^{n+\frac{1}{2}}(I+1,J+\frac{1}{2},K)-H_y^{n+\frac{1}{2}}(I,J+\frac{1}{2},K)]\}
\end{aligned}
$$

$$
\begin{aligned}
&H_x^{n+\frac{1}{2}}(I+\frac{1}{2},J,K)\\
&=H_x^{n-\frac{1}{2}}(I+\frac{1}{2},J,K)\\
&+\{\frac{c\Delta t}{\Delta y}[E_z^n(I+\frac{1}{2},J-\frac{1}{2},K)-E_z^n(I+\frac{1}{2},J+\frac{1}{2},K)]\\
&+\frac{c\Delta t}{\Delta z}[E_y^n(I+\frac{1}{2},J,K+\frac{1}{2})-E_y^n(I+\frac{1}{2},J,K-\frac{1}{2})]\}
\end{aligned}
$$

$$
\begin{aligned}
&H_y^{n+\frac{1}{2}}(I,J+\frac{1}{2},K)\\
&=H_y^{n-\frac{1}{2}}(I,J+\frac{1}{2},K)\\
&+\{\frac{c\Delta t}{\Delta z}[E_x^n(I,J+\frac{1}{2},K-\frac{1}{2})-E_x^n(I,J+\frac{1}{2},K+\frac{1}{2})]\\
&+\frac{c\Delta t}{\Delta x}[E_z^n(I+\frac{1}{2},J+\frac{1}{2},K)-E_z^n(I-\frac{1}{2},J+\frac{1}{2},K)]\}
\end{aligned}
$$

$$
\begin{aligned}
&H_z^{n+\frac{1}{2}}(I,J,K+\frac{1}{2}) \\
&= H_z^{n-\frac{1}{2}}(I,J,K+\frac{1}{2}) \\
&+ \{\frac{c\Delta t}{\Delta x}[E_y^n(I-\frac{1}{2},J,K+\frac{1}{2}) - E_y^n(I+\frac{1}{2},J,K+\frac{1}{2})] \\
&+ \frac{c\Delta t}{\Delta y}[E_x^n(I,J+\frac{1}{2},K+\frac{1}{2}) - E_x^n(I,J-\frac{1}{2},K+\frac{1}{2})]\}
\end{aligned}
$$

where the electric and magnetic fields are calculated in the time domain, and Δx, Δy, Δz, and Δt satisfy the Courant-Friedrichs-Levy (CFL) condition [*Taflove*, 1995] in the form of

$$
c\Delta t \le \frac{1}{\sqrt{1/\Delta x^2 + 1/\Delta y^2 + 1/\Delta z^2}}
$$

to suppress the numerical instability.

In the present study, we consider particle sizes ranging from 1 μm to 180 μm. Over this size range, the T-matrix method gives convergent solutions in the 8-12 μm spectral region. For a given maximum dimension, the aspect ratio given by *Yang et al.* [2001] follows

$$
2a/L = \begin{cases} 1 \quad \text{for } L \le 40\ \mu m \\ \exp[-0.017835(L-40)] \quad \text{for } 40\ \mu m < L \le 50\ \mu m \\ 5.916/L^{1/2} \quad \text{for } L > 50\ \mu m\ , \end{cases} \tag{2.15}
$$

where a is the semi-width of the cross section, and L is the length of a hexagonal column. Ice crystals defined by Eq. (2.15) are compact hexagons with an aspect ratio of unity if their maximum dimensions are smaller than 40 μm, whereas crystals larger than 40 μm are essentially hexagonal columns.

The radius of the cross section and the length of a circular cylinder are indicated by R and H, respectively. To define an equivalent circular cylinder for a hexagonal particle, one can assume that the two particles have the same projected area, volume, or the ratio of volume to projected area under the condition that the two particles have the same length or aspect ratio. If circular and hexagonal cylinders have the same length (i.e., $H = L$), the radius of the circular cylinder with the same volume is given by

$$R_v = \sqrt{\frac{3\sqrt{3}}{2\pi}} a, \tag{2.16}$$

where the subscript v indicates that the circular cylinder has the same volume as the hexagon. The cross-section radius of a circular cylinder with the same projected area as the hexagon is given by

$$R_a = \frac{\sqrt{L^2 + (6\sqrt{3}a^2 + 12aL)/\pi} - L}{2}. \tag{2.17}$$

Similarly, the cross-section radius of the circular cylinder that has the same ratio of volume to projected area of a hexagon is given by

$$R_{v/a} = \frac{\sqrt{3}}{2} a. \tag{2.18}$$

To define the equivalence of a circular cylinder and a hexagonal column in scattering calculations, one can also let the two particles have the same aspect ratio, that is $a / L = R / H$. For this condition, the cross-section radius of circular cylinder with equivalent volume, equivalent projected area, or equivalent ratio of volume to projected area is given by

$$R_v^* = \left(\frac{3\sqrt{3}}{2\pi}\right)^{\frac{1}{3}} a, \tag{2.19}$$

$$R_a^* = \left(\frac{3\sqrt{3}a + 6L}{2\pi(a+L)}\right)^{\frac{1}{2}} a, \tag{2.20}$$

$$R_{v/a}^* = \frac{\sqrt{3}(a+L)}{\sqrt{3}a + 2L} a. \tag{2.21}$$

The lengths associated with the radii in Eqs.(2.19)-(2.21) are given by

$$H_v^* = \left(\frac{3\sqrt{3}}{2\pi}\right)^{\frac{1}{3}} L, \tag{2.22}$$

$$H_a^* = \left(\frac{3\sqrt{3}a + 6L}{2\pi(a+L)}\right)^{\frac{1}{2}} L, \tag{2.23}$$

$$H_{v/a}^* = \frac{\sqrt{3}(a+L)}{\sqrt{3}a + 2L} L. \tag{2.24}$$

Figure 2.1 shows the radii and lengths defined in Eqs. (2.16)-(2.21) versus the semi-width (a) and the length (L) of a hexagonal column. The aspect ratio defined in Eq. (2.15) is used for defining the semi-width of the cross-section of the hexagonal column with a given length. The left panel of Fig. 2.1 shows the radii of circular cylinders with the same surface area (A), volume (V), or the ratio of volume to surface area (V/A) as hexagonal columns, when the length of the two geometries are the same. Evidently, the circular cylinder specified on the basis of surface-area equivalence is largest, whereas the one based on V/A equivalence is smallest in terms of the radius of the cross section. The middle and right panels in Fig.2.1 are the radii and lengths of

cylinders having aspect ratios that are the same as for the hexagonal crystals. The same feature is noted.

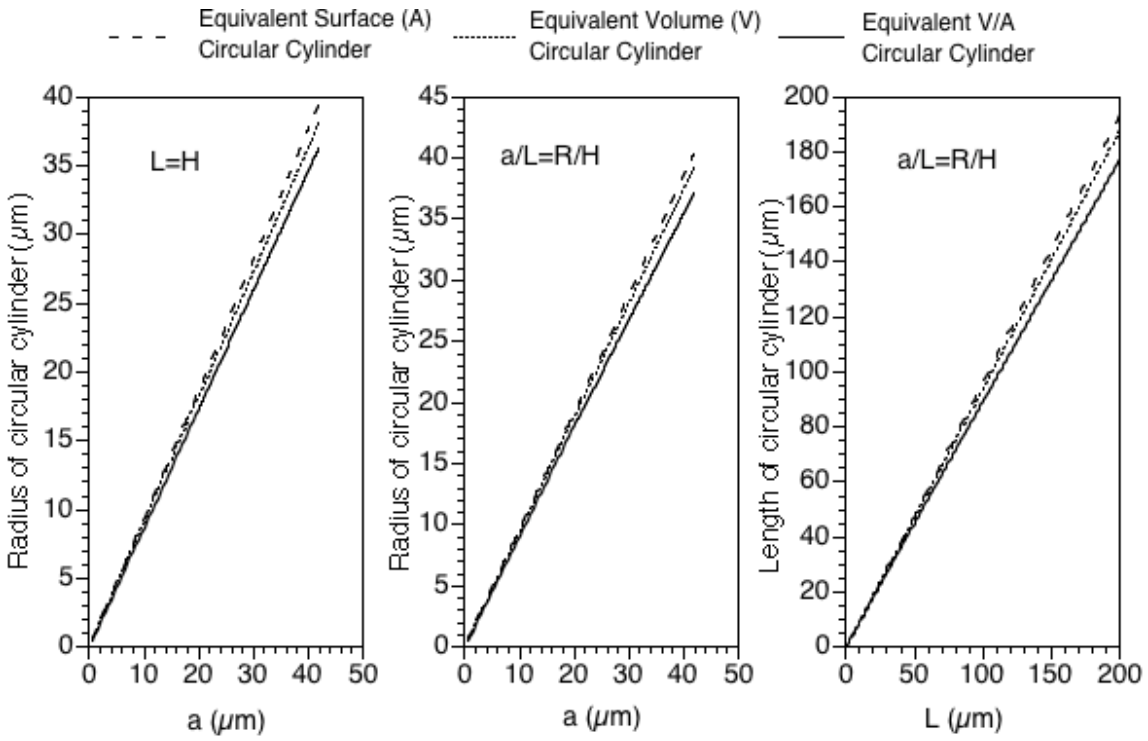

Figure 2.1 The radii and lengths of circular cylinders defined as having the same volume, surface area, or the ratio of volume to surface area as hexagonal columns, when the same length or aspect ratio is applied to the two geometries. The left panel is for the case when the lengths of circular cylinders and hexagonal columns are the same. The middle and right panels are for the case when the aspect ratio is kept constant in defining the equivalence.

2.3 Numerical results and discussions

The present results focus on the scalar optical properties including extinction efficiency, absorption efficiency, phase function, and asymmetry factor. Similarly to *Yang et al.*, [2001] we use the refractive index compiled by *Warren* [1984] in the numerical computations. The T-matrix computational code is implemented with the extended double precision algorithm [*Mishchenko and Travis*, 1994].

Figure 2.2 shows the comparison of phase functions between hexagonal ice columns and circular ice cylinders. The circular cylinders are defined to have the same length and volume as hexagonal columns. For sizes, $L = 10$ μm, 20 μm, and 40 μm, the phase functions of hexagonal columns are computed using the FDTD method whereas the results for $L =$ 140 μm are computed using an improved geometric optics method. For small sizes, the phase functions of circular cylinders are essentially the same as those of hexagonal columns. The slight differences between the two results near backscattering angles in the case of $L = 40$ μm might be caused by the inaccuracy of the FDTD method due to insufficient resolution of the grid mesh. The performance of the FDTD method for hexagonal ice crystals has been recently assessed by *Baran et al.* [2001] in comparison with the implementation of the T-matrix method to a hexagonal geometry. From Fig. 2.2, excellent agreement between the results for $L = 140$ μm is also noted. Evidently, the sharp edges of the side faces of hexagonal geometry are not important in specifying the optical properties of the particles. Instead, the overall

morphology of the particle as a cylinder or column is the major factor affecting the particle optical properties.

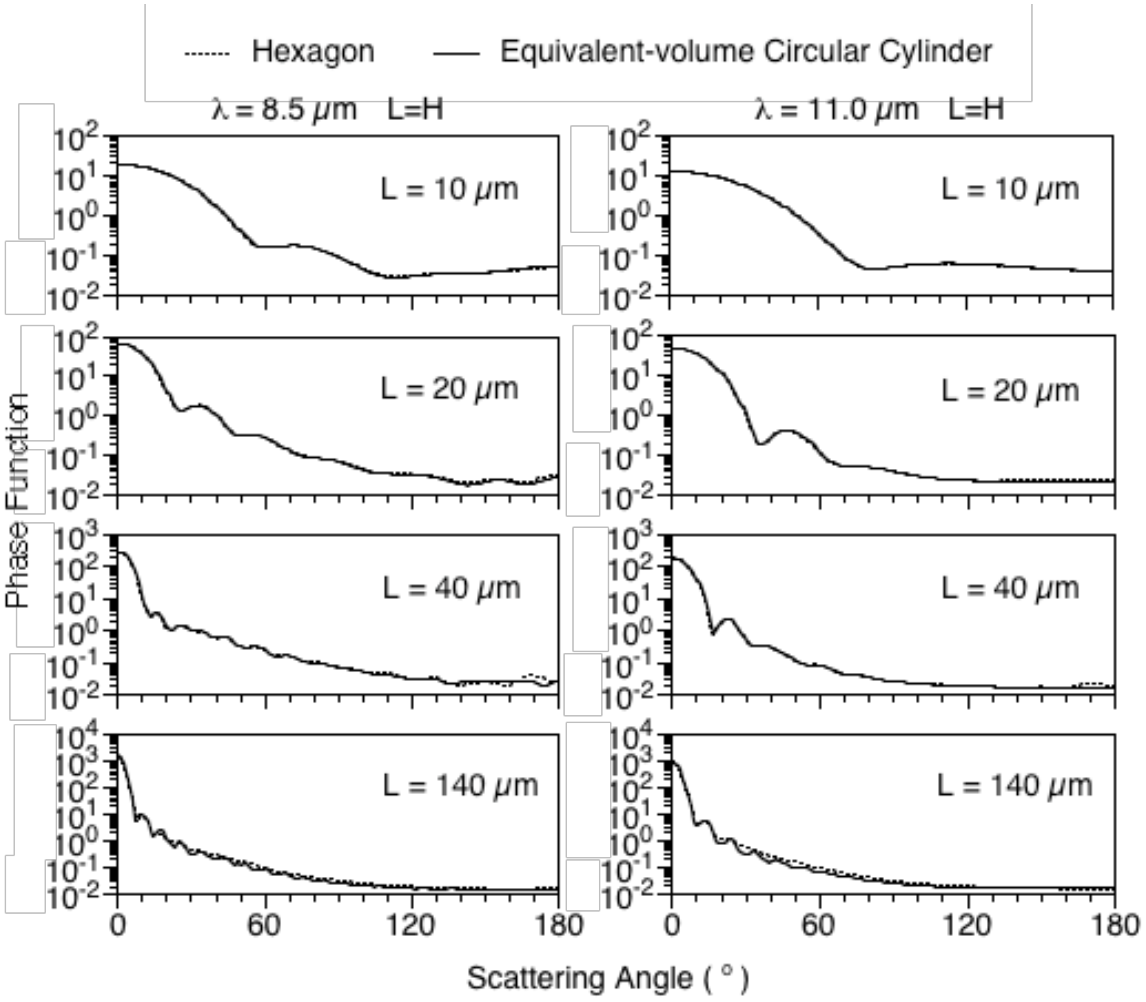

Figure 2.2 The comparison of phase functions of circular cylinders and hexagonal columns. The circular cylinders are defined as having the same volume and length as hexagonal columns. The results for circular cylinders are computed by using Mishchenko's T-matrix code [1991]. For hexagonal columns, the finite-difference time domain method is used for small particles (L=10, 20 and 40 μm), whereas an improved geometric optics method is used for L=140 μm.

For infrared radiative transfer simulations, the phase function of cirrus particles can be approximated by the Henyey-Greenstein (H-G) function given by

$$P_{HG}(\theta) = \frac{1-g^2}{(1+g^2+2g\cos\theta)^{3/2}}$$

$$= \sum_{l=0}^{N}(2l+1)g^l P_l(\cos\theta)\,, \tag{2.25}$$

where θ is the scattering angle, and g is the asymmetry factor of an ice crystal, which is defined as follows:

$$g = \frac{1}{2}\int_0^{\pi} P(\theta)\cos(\theta)\sin(\theta)d\theta\,, \tag{2.26}$$

where $P(\theta)$ is the phase function of nonspherical ice crystals. $P_l(\cos\theta)$ in Eq. (2.25) is the l-th Legendre polynomial. The H-G phase function is used frequently for its simplification and efficiency in numerical computations. In the following discussion, emphasis will be on the asymmetry factor of the phase function, instead of the detailed angular variation of the computed scattering phase function. Note that the present computations are limited to scalar optical properties. The computation of the full phase matrix elements of the circular ice cylinders at a number of infrared wavelengths have been recently reported by *Xu et al.* [2002] who used Mishchenko's T-matrix code for their numerical computation.

The present computations cover the terrestrial infrared window (8–12 μm) region, but in this paper, the discussion is limited to numerical results at 8.5- and 11-μm wavelengths. The radiometric measurements at the spectral bands centered at these two wavelengths are often used to retrieve cloud properties [*Baum et al.*, 2000]. For

investigations involving ice particles, the 11 μm wavelength is unique because it is within the Christiansen band [*Arnott et al.*, 1995; *Yang et al.*, 1997]. To ascertain the differences between the optical properties of circular ice cylinders and hexagonal ice columns, we define the relative difference ε as follows:

$$\varepsilon = \frac{\text{Result}_{\text{circular cylinder}} - \text{Result}_{\text{hexagonal column}}}{\text{Result}_{\text{hexagonal column}}} \times 100\%. \tag{2.27}$$

Figure 2.3 shows the extinction efficiencies of hexagonal ice columns and various equivalent circular ice cylinders at λ = 8.5 μm. Also shown are the relative differences between the results for the hexagonal and circular cylinder geometries. The left two panels are for the case when hexagons and circular cylinders have the same length, whereas the right panels are for the case when the two geometries have the same aspect ratio. Evidently, for large particles (>120 μm), the differences between various equivalent definitions are reduced in magnitude, particularly in the case where the aspect ratio is kept constant for the two geometries. The extinction efficiency of the equivalent-volume circular cylinder (L=H) is closer to that of hexagonal column than the other equivalence definitions. The maximum difference is less than 10%, except in the case where the two geometries have the same length and radius. For large sizes (>100 μm), the maximum difference is reduced to approximately 3%. A previous study by *Baran and Havemann* [2000] also noticed that for large size parameters the single-scattering properties asymptote to their limiting values and as such become independent of crystal shape at IR wavelengths.

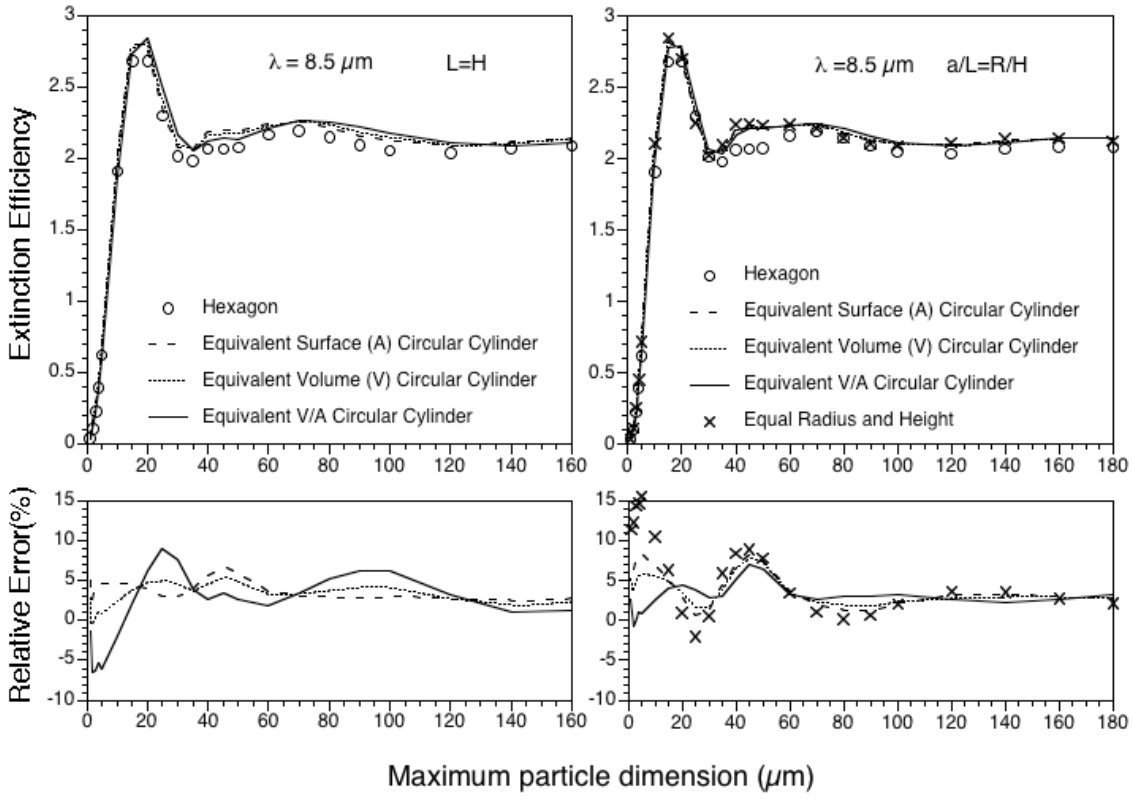

Figure 2.3 The comparison of the extinction efficiencies at a wavelength of 8.5 μm for hexagonal columns and various equivalent circular cylinders. The results for hexagonal particles are taken from *Yang et al.* [2001].

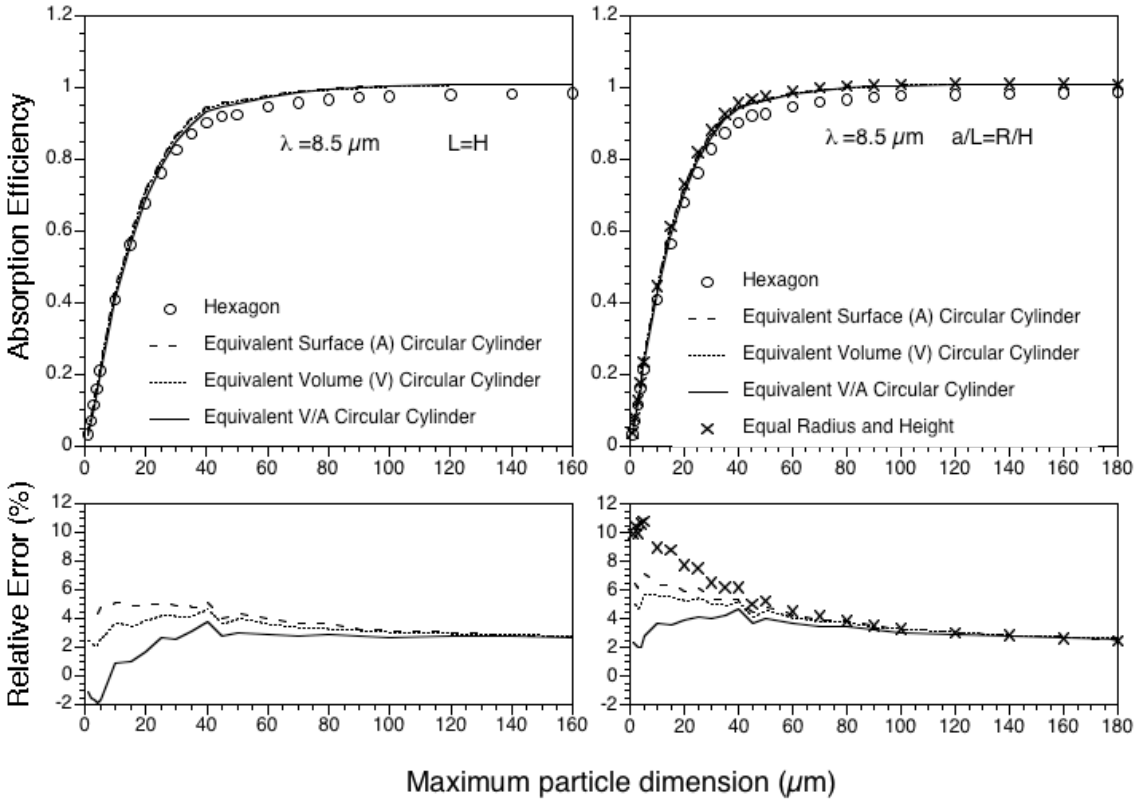

Figure 2.4 The absorption efficiencies corresponding to the extinction efficiencies shown in Fig. 2.3.

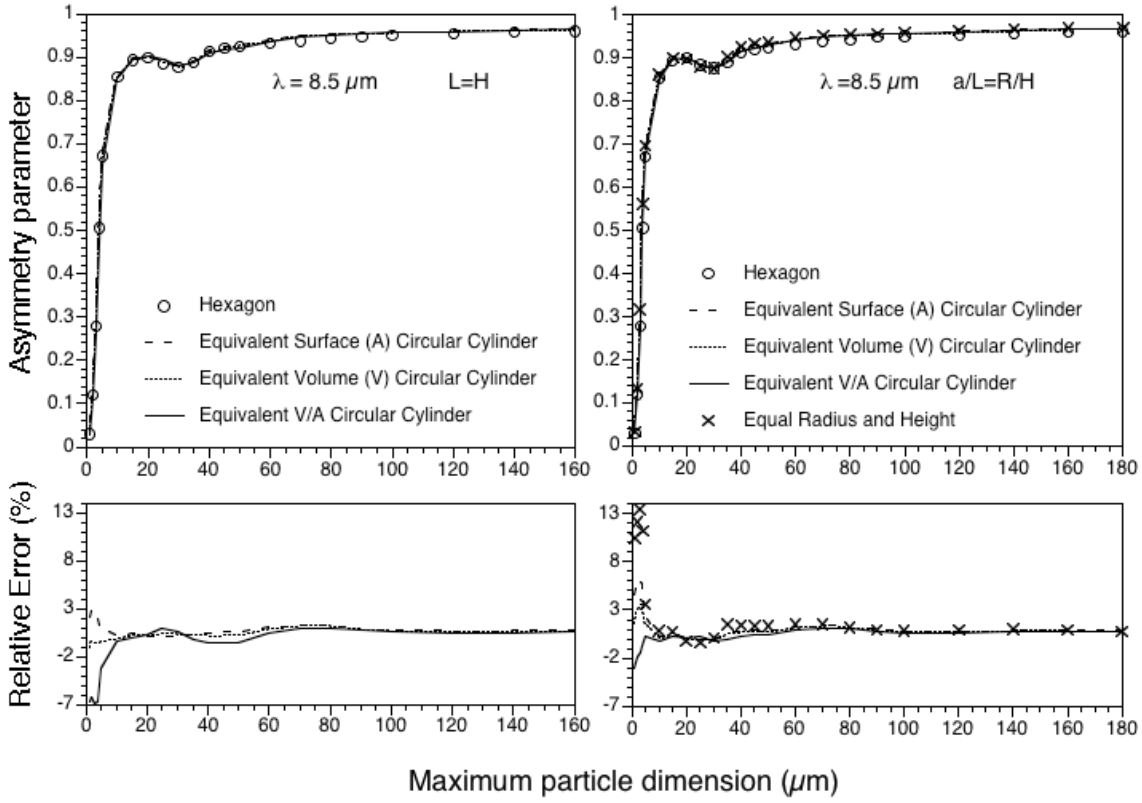

Figure 2.5 The asymmetry factors corresponding to the efficiencies shown in Figs. 2.3 and 2.4.

Figure 2.4 shows the absorption efficiencies and relative differences that correspond to the results shown in Fig. 2.3. Evidently, for large particle sizes (> 100 μm), the results for various definitions of equivalent circular cylinders converge, and the relative differences converge to approximately 2%. The differences between the absorption efficiency of hexagonal columns and the circular cylinders with the same ratio of volume to projected area are smaller in comparison to the results for other equivalence definitions. *Fu et al.* [1998] ascertained the errors of approximating hexagonal columns by spheres with various equivalent definitions in the computation of absorption efficiency. They also noticed that the equivalent sphere based on the same ratio of volume to projected-area leads to the smallest errors. Our conclusion is consistent with the previous study. For practical applications concerning IR radiative transfer, the most important process is absorption. From this perspective, hexagonal ice columns may be approximateed by circular cylinders with the same ratio of volume to projected area. In fact, the ratio of particle volume to particle projected area is proportional to the mean path-length of the rays inside the particle in the framework of anomalous diffraction theory (ADT).

Figure 2.5 shows the asymmetry factor values that correspond to the extinction and absorption efficiencies shown in Figs. 2.3 and 2.4. The definition of the equivalent circular cylinder for a hexagonal column seems to have a negligible effect on the value of the asymmetry factor when the particle size is larger than approximately 80 μm. In this case, the differences of the asymmetry factors between the hexagonal and circular cylinder geometries are less than 2%. For particle sizes smaller than 20 μm, it is

important how the equivalent circular cylinder is defined. When L=H, the asymmetry factor for the equivalent-volume circular cylinders is closer to that of hexagonal columns, in comparison with the other equivalent circular cylinder definitions. Another feature shown in Fig. 2.5 is that the asymmetry factor is small for small particles (less than 15 μm), whereas the asymmetry factor reaches its asymptotic value for large particle sizes. For small particles, the scattering pattern is close to that of Rayleigh scattering and the phase function is not strongly asymmetric with respect to scattering angle, leading to a small asymmetry factor. When the particle size is large, any rays refracted into the particles are essentially absorbed because of the strong absorption of ice at infrared wavelengths. The scattered energy is derived primarily from the diffracted energy that is concentrated in the forward direction.

Figures 2.6, 2.7, and 2.8 show the extinction efficiency, absorption efficiency, and asymmetry factor, respectively, but at λ = 11 μm. The Christiansen band lies near 11 μm [*Arnott et al.*, 1995; *Yang et al.*, 1997]. In this region, the extinction reaches its minimum and the absorption within the ice crystal is substantial. Unlike the case at λ = 8.5 μm, the extinction efficiency at λ = 11 μm converges for various definitions of equivalent circular cylinders for particle sizes larger than 60 μm. The asymptotic value for the differences between the extinction efficiencies of the hexagonal column and the circular cylinder is approximately 4%.

For the absorption efficiency shown in Fig. 2.7, the results for the equivalent-volume, equivalent-surface area, and the equivalent ratio of volume to surface area yield similar differences. All of the three definitions yield a maximum of the relative

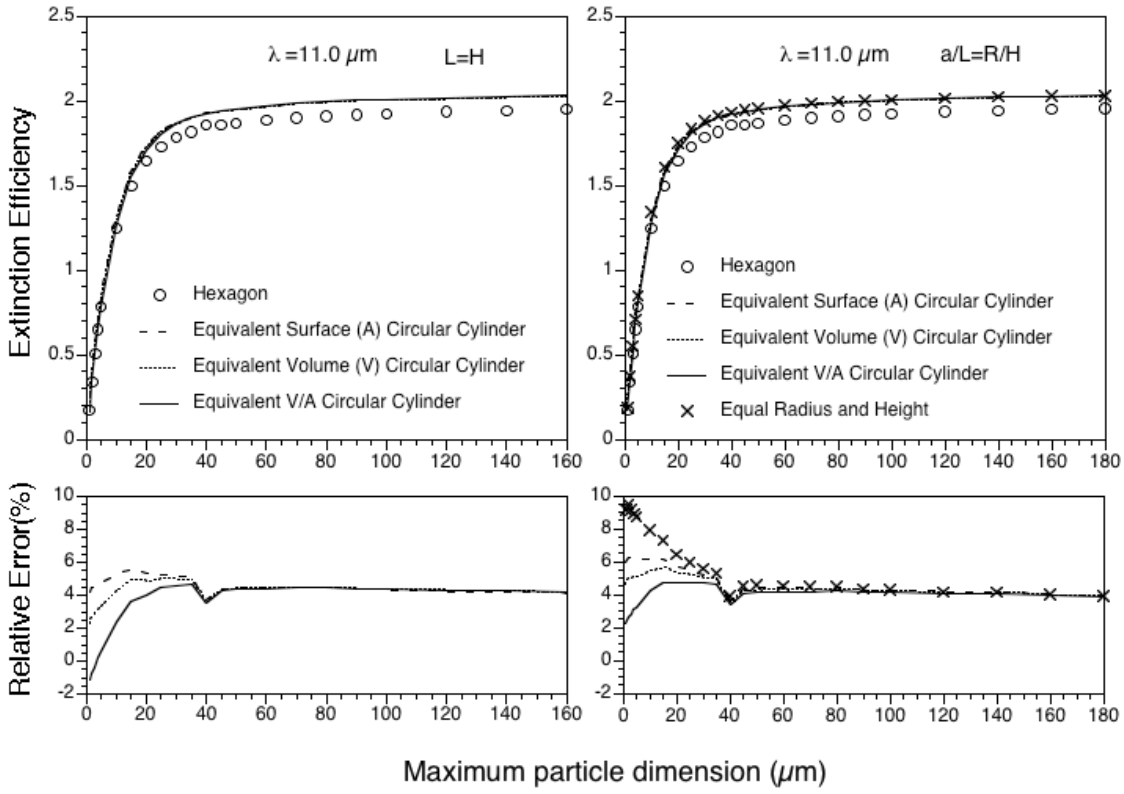

Figure 2.6 Same as Fig. 2.3, except the calculations are performed at a wavelength of 11 μm.

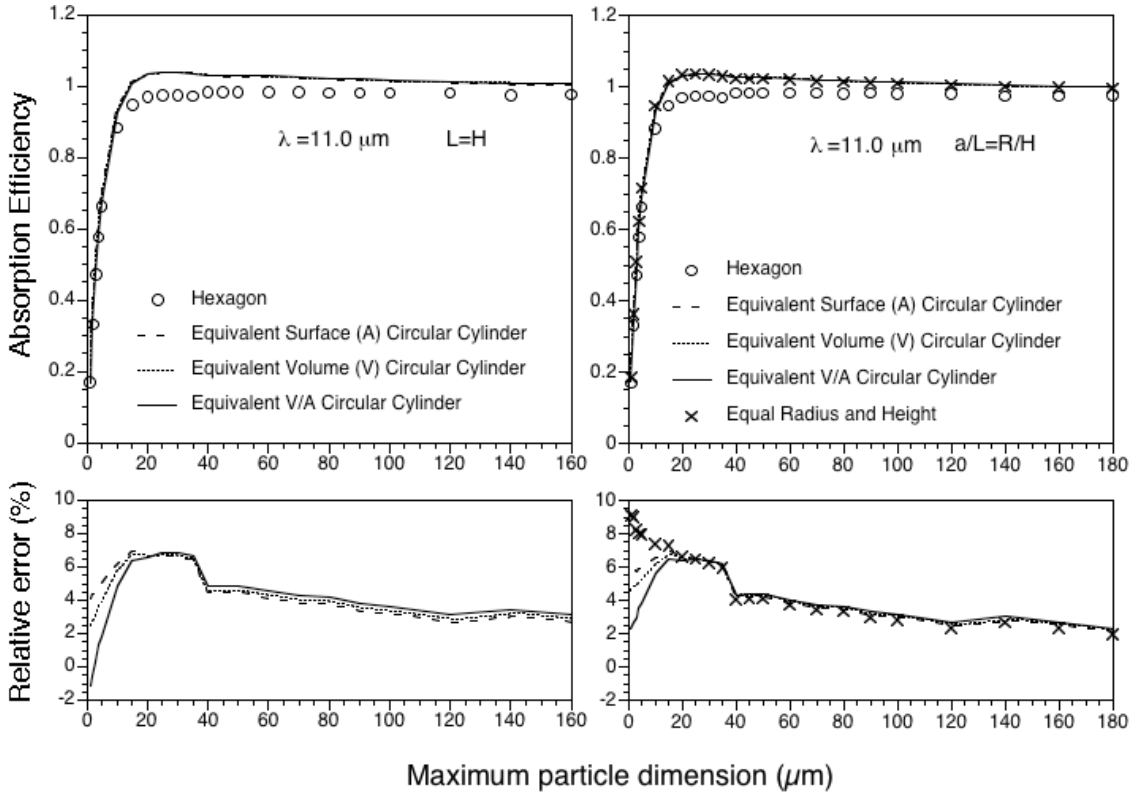

Figure 2.7 Same as Fig. 2.4, except the calculations are performed at a wavelength of 11 μm.

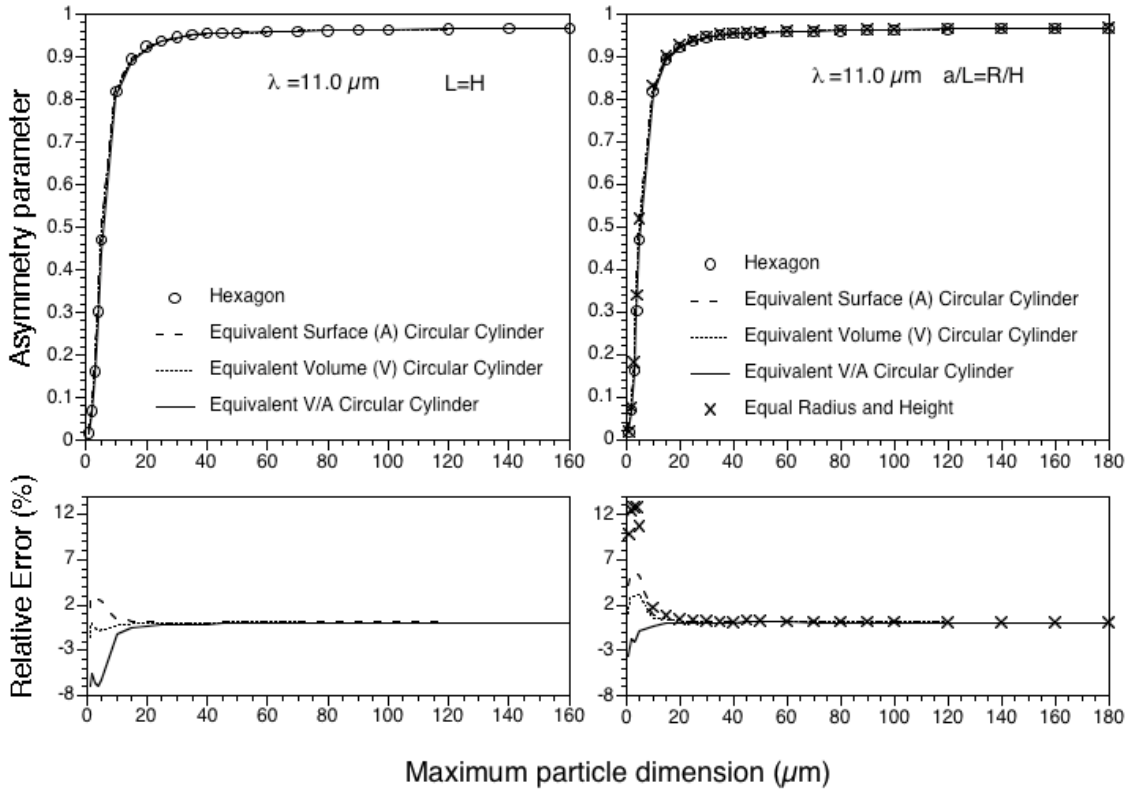

Figure 2.8 Same as Fig. 2.5, except the calculations are performed at a wavelength of 11 μm.

Table 2.1 Minimum and maximum relative errors of the approximation of hexagonal column by circular cylinders using the T-matrix compared to *Yang et al*. [2001]. The upper panel is for calculations performed at a wavelength of 8.5 μm and the lower panel is for calculations performed at 11.0 μm.

	λ=8.5 μm						
	H=L			a/L=R/H			
	Equivalent Surface Area (A)	Equivalent Volume (V)	Equivalent Ratio of V to A	Equivalent Surface Area (A)	Equivalent Volume (V)	Equivalent Ratio of V to A	a=R and H=L
Extinction Efficiency	(2.4, 6.6)	(-0.6, 5.5)	(-6.5, 8.9)	(0.7, 8.4)	(1.7, 7.8)	(-0.7, 7.0)	(-2.0, 15.5)
Absorption Efficiency	(2.7, 5.2)	(2.1, 4.7)	(-1.9, 3.8)	(2.5, 7.1)	(2.5, 5.7)	(2.0, 4.6)	(2.5, 10.8)
Asymmetry Factor	(0.1, 2.9)	(-0.1, 1.2)	(-6.9, 1.0)	(-0.1, 6.2)	(-0.2, 3.6)	(-3.0, 1.2)	(-0.4, 13.4)

	λ=11 μm						
	H=L			a/L=R/H			
	Equivalent Surface Area (A)	Equivalent Volume (V)	Equivalent Ratio of V to A	Equivalent Surface Area (A)	Equivalent Volume (V)	Equivalent Ratio of V to A	a=R and H=L
Extinction Efficiency	(3.8, 5.6)	(2.3, 5.0)	(-1.2, 4.7)	(3.9, 6.2)	(3.9, 5.7)	(2.2, 4.8)	(3.9, 9.5)
Absorption Efficiency	(2.7, 6.9)	(2.3, 6.8)	(-1.1, 6.9)	(2.1, 7.0)	(2.2, 6.8)	(2.3, 6.5)	(2.0, 9.1)
Asymmetry Factor	(0.0, 3.1)	(-1.8, 0.2)	(-6.9, 0.1)	(-0.1, 5.7)	(0.1, 3.2)	(-3.6, 0.2)	(0.1, 12.8)

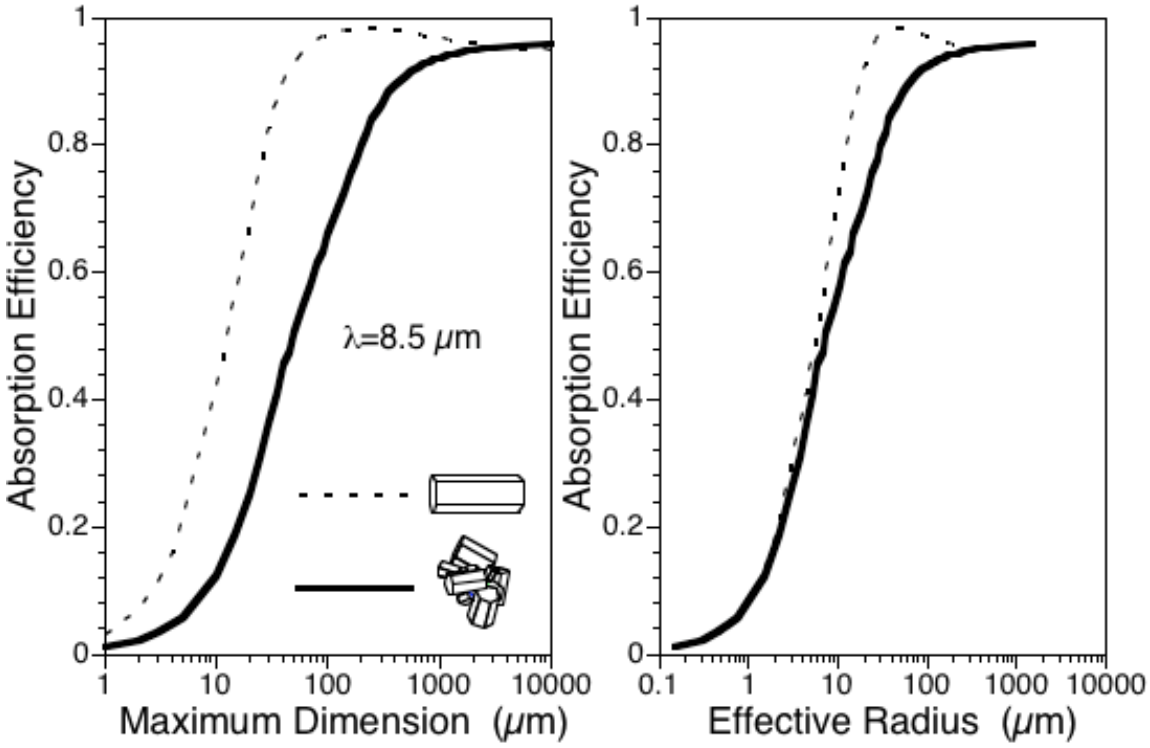

Figure 2.9 Comparison of absorption efficiencies of pristine hexagonal ice columns and aggregate ice crystals. The procedure of computing the optical properties of aggregates is explained in *Yang et al*. [2002].

difference in the size range of 15 μm to 40 μm. However, the magnitude of the differences is less than 7%. For very small ice crystals with sizes from 1 μm to 10 μm, the equivalence based on equal radius and height can lead to differences much larger than differences for other definitions. For the asymmetry factor shown in Fig. 2.8, convergence of the results for various equivalence definitions is obtained for particle sizes larger than 20 μm. For small sizes (<20 μm), the equivalent-volume circular cylinder yields the minimum difference when the two geometries have the same length (i.e., L=H).

Table 2.1 lists the errors obtained from approximating hexagonal columns by circular cylinders based upon the calculation of the various optical properties shown in Figs. 2.3-2.8. Based upon these error values, the equivalence based on the ratio of V/A performs the best for calculation of the absorption efficiency. For the asymmetry factor, the volume equivalence definition yields minimum errors. For the extinction efficiency, various equivalence definitions have a similar error range, except in the case where the equivalence is based on a=R and H=L.

In reality, pristine ice crystals are not common in cirrus clouds. For ice crystals with complex geometries, their optical properties cannot be well approximated by those of a simple morphological structure. To illustrate this, Fig. 2.9 shows the absorption efficiencies of pristine hexagonal columns and aggregates. The definition of the aggregate geometry is explained by *Yang and Liou* [1998]. The numerical computation of the optical properties of aggregates in Fig. 2.9 is explained by *Yang et al.* [2002]

Following *Foot* [1988], *Francis et al.* [1994], *Mitchell et al.* [1994], *Fu et al.* [1998], the effective radius is defined as

$$R_e = \frac{3}{4}\frac{V}{A}, \tag{2.28}$$

where V and A are the volume and projected area of the nonspherical particles, respectively. From Fig. 2.9, it is evident that the absorption efficiencies of the two geometries are quite different regardless of whether the sizes of the particles are defined in terms of maximum dimension or effective size. Note that *Baran et al.* [2003] attribute the differences of the absorption efficiencies of aggregates and columns to a tunneling effect.

CHAPTER III

POTENTIAL NIGHTTIME CONTAMINATION OF CERES CLEAR-SKY FIELDS OF VIEW BY OPTICALLY THIN CIRRUS DURING THE CRYSTAL-FACE CAMPAIGN[*]

3.1 Background

Thin cirrus clouds are widespread and radiatively important [e.g., *Chepfer et al*., 1998, 2001; *Gao et al*., 2002; *Mather et al*., 1998; *McFarquhar et al*., 2000; *Prabhakara et al*., 1993; *Rossow and Schiffer*, 1991; *Wang et al*., 1994, 1996; *Winker and Trepte*, 1998]. Several studies [*Dessler and Yang*, 2003; *Meyer et al*., 2004; *Roskovensky and Liou*, 2003; *Kahn et al*., 2005] show that optically thin cirrus properties can be inferred on the basis of satellite observations (e. g., the radiometric measurements acquired by MODIS or AIRS). In particular, *Dessler and Yang* [2003] further analyzed MODIS cloud-cleared data [*Ackerman et al*. 1998] over the oceans between 30°S and 30°N using the 1.375 μm channel. While the cirrus clouds were too tenuous for the data to be flagged as being cloudy using the operational cloud clearing procedure, the Tropical Western Pacific (TWP) region was shown to be an area where cirrus occurred with a high frequency, with optical thicknesses generally between 0.1 and 0.15. A substantial portion of the MODIS clear-sky pixels near Hawaii were contaminated by subvisual

[*] Lee, Y.-K., P, Yang, Y. Hu, B. A. Baum, N. G. Loeb, and B.-C. Gao, Potential nighttime contamination of CERES clear-sky fields of view by optically thin cirrus during CRYSTAL-FACE campaign, Journal of Geophysical Research, 111, D09203, doi: 10.1029/2005JD006372. Reproduced by permission of American Geophysical Union.

cirrus clouds. Note that subvisual cirrus clouds are defined by *Sassen et al.* [1989] to have optical thickness less than 0.03. In terms of optical thickness, the operational lower threshold for cirrus detection based on the MODIS multispectral data is approximately 0.2-0.3 [*Dessler and Yang*, 2003]. The inability to adequately detect and analyze these thin cirrus clouds may lead to biases in the simulated longwave and window radiances in comparison with measurements.

Motivated by the fact that the inability to adequately detect and analyze these thin cirrus clouds may lead to biases in the simulated LW and WIN radiances, this study investigates the potential contamination of CERES clear-sky FOVs by optically thin cirrus clouds. Additionally, the anisotropy factors associated with the CERES LW and WIN channel radiation fields are also investigated. The data involved in the present study were acquired during the Cirrus Regional Study of Tropical Anvils and Cirrus Layers-Florida Area Cirrus Experiment (CRYSTAL-FACE) campaign [*Jensen et al.*, 2004] in July 2002. Rawinsonde data obtained during the CRYSTAL-FACE campaign provide the atmospheric profiles of temperature and humidity which are necessary for the radiative transfer simulations for a direct comparison with the corresponding CERES data.

3.2 Data and methodology

The Clouds and the Earth's Radiant Energy System (CERES) [*Wielicki et al.*, 1996] is one of the state-of-the-art scientific satellite instruments developed for NASA's Earth Observing System (EOS). Included in the CERES Single Scanner Footprint (SSF)

products [*Geier et al.*, 2003] are various parameters including the broadband radiances and the fluxes at the top-of-atmosphere (TOA) and the surface. Each CERES field of view (FOV) in the SSF product contains imager-based information on clear-sky conditions and/or cloud properties for up to two cloud layers, including cloud top height, cloud thermodynamic phase, cloud effective particle size, and cloud optical thickness.

The CERES instrument measures broadband filtered radiances in three channels: a total channel (0.3-200 μm), a shortwave channel (0.3-5 μm), and a window channel (WIN, 8-12 μm) [*Lee et al.*, 1996]. The daytime longwave (LW, 5~200 μm) radiance is determined from the total, window, and shortwave channel measurements, whereas the nighttime LW radiance is derived from the total and the window channel measurements [*Loeb et al.*, 2001]. The measured filtered radiances are converted to the corresponding unfiltered radiances before subsequent conversion to fluxes. The development of the CERES operational products also involves the Moderate Resolution Imaging Spectroradiometer (MODIS) cloud data for determining cloud properties within each CERES FOV [*Minnis et al.*, 1997; *Smith et al.*, 2004]. With the scene identification (including the surface features) provided in the CERES FOV, broadband radiances are converted to fluxes by using a set of angular distribution models (ADMs) [*Loeb et al.*, 2003b; *Loeb et al.*, 2005]. The LW broadband radiance decreases as viewing zenith angle increases. This feature is called the limb-darkening effect [*Loeb et al.*, 2003b; Smith et al., 1994]. The conversion of unfiltered radiance to flux is based on an ADM that takes the limb darkening effect into account. For the CERES Terra SSF Edition-1A data, the ADMs developed for TRMM have been used [*Loeb et al.*, 2003b].

The advantage of the CERES SSF product is that it provides quantitative cloud information (e.g., the optical thickness). Given a vertical atmospheric profile that includes the vertical distributions of the atmospheric temperature and water vapor through the rawinsonde measurements, the CERES SSF product in conjunction with a rigorous radiative transfer model can be used for computing the column radiance and flux.

With the scene identification information, including the surface emissivity [*Wilber et al.*, 1999] and surface skin temperature (SSF-59) for a CERES FOV, and the corresponding rawinsonde observation, the vertical structure of the absorption due to various radiatively important gases can be computed with the use of the HITRAN-2000 database [*Rothman et al.*, 1998]. Furthermore, with the gaseous absorption optical thickness, the discrete ordinate radiative transfer (DISORT) model [*Stamnes et al.*, 1988] can be used to compute the LW and WIN channel broadband radiances. The surface skin temperature is defined as MOA (Meteorological, Ozone, and Aerosols) surface temperature at a level of 2 cm below the surface over land, and the surface skin temperature corresponds to the Reynold's Sea Surface Temperature (SST) [*Geier et al.*, 2003] over the ocean.

The rawinsonde data used in this study were acquired during the CRYSTAL-FACE campaign in July 2002 at four locations: Key West (24.5 N, 81.8 W), Miami (25.8 N, 80.4 W), Tampa (27.7 N, 82.4 W) (NWS stations) and Everglades City (25.844 N, 81.386 W) (Pacific Northwest Laboratory PARSL facility). For the radiative transfer simulations, the atmosphere sampled by each rawinsonde is divided into 100 layers.

When the cloud fraction for a CERES FOV is less than 0.1%, the FOV is regarded as clear [*Loeb et al.*, 2003b]. CERES products provide clear percent coverage that indicates the coverage of clear condition within a FOV. In this study we consider only FOVs with a clear-sky coverage of at least 99.9%. In total, 76 FOVs are selected from different days in July 2002 for a detailed study within an area of 0.25° x 0.25° in terms of the latitudes and longitudes around the four locations where the rawinsonde data were taken. The surface type is ocean for 33 FOVs and land for the other 43 FOVs. Of these, 74 FOVs are observed at night and 2 FOVs in the daytime over the ocean. The average height of the tropopause is 15.6 km and the mean temperature 199.2 K. The CERES SSF data (e.g., radiance, flux, emissivity, surface skin temperature) from the EOS Terra platform were used in this study.

The CERES cloud mask classification technique employs threshold tests that involve the radiances acquired at 0.64, 1.6, 3.7, 11, and 12 μm MODIS imager channels [*Minnis et al.*, 2003; *Trepte et al.*, 1999]. A MODIS pixel is declared as cloudy when at least one of these five channel radiances is significantly different from the corresponding expected clear sky radiance. MODIS pixels deemed as clear are categorized as weak and strong, or they can be classified as being filled with fire, smoke, or aerosol, or being affected by sunglint, or covered with snow. While all five channels can be used during the daytime, only three infrared channels, 3.7, 11, and 12 μm, are used at nighttime. The MODIS imager pixel results are convolved into each CERES FOV and subsequently are used to provide the cloud fraction within the CERES FOV.

In the present forward radiative transfer simulations, an optically thin cirrus layer is placed below the tropopause for a given clear-sky CERES FOV. The average geometrical cloud thickness is 0.5 km. An optically thin cirrus cloud located near the tropopause at extremely cold temperatures is assumed to consist solely of droxtals [*Yang et al*., 2003a; *Zhang et al*., 2004] for the theoretical light scattering and radiative transfer computations. *Baum et al*. [2005a] discuss the use of *in situ* cirrus microphysical data from midlatitude synoptic cirrus and tropical anvil cirrus to develop bulk ice cloud scattering models. However, for ice clouds of extremely low optical thickness that are located just below the tropopause, the assumption is made that the particle size distributions are extremely narrow and centered at very small particle sizes. The single-scattering properties of droxtals are provided at 39 wavenumbers selected within a spectral region spanning from 50 to 2000 cm^{-1}, which are further interpolated for a high spectral resolution on the basis of a spline-interpolation technique. The extinction efficiency, absorption efficiency, and asymmetry factor are computed from the composite method developed by *Fu et al*. [1999]. The technical details for the present light scattering computation are not described here, as they are similar to those reported by *Yang et al*. [2005].

To consider the effect of size distribution, we use the gamma distribution [*Hansen and Travis*, 1974], given as follows:

$$n(r) = \frac{N_0 (r_{eff} V_{eff})^{(V_{eff}-1)/V_{eff}}}{\Gamma[(1-2V_{eff})/V_{eff}]} r^{(1-3V_{eff})/V_{eff}} \times \exp(-r/r_{eff}V_{eff}), \qquad (3.1)$$

where N_0 is the total number of the particles in unit volume. In Eq. (3.1), r_{eff} and V_{eff} are effective radius and variance (or dispersion), respectively, which are given by

$$r_{eff} = \frac{\int_{r_1}^{r_2} r^3 n(r)\,dr}{\int_{r_1}^{r_2} r^2 n(r)\,dr}, \tag{3.2}$$

$$V_{eff} = \frac{\int_{r_1}^{r_2} (r - r_{eff})^2 r^2 n(r)\,dr}{r_{eff}^{\,2} \int_{r_1}^{r_2} r^2 n(r) dr}. \tag{3.3}$$

The effective variance (V_{eff}) for various water clouds lies between 0.111 and 0.193 [*Hansen*, 1971]. In this study, a variance value of $V_{eff} = 0.2$ is used for cirrus. It is reasonable to choose an effective variance larger for an ice cloud than for a water cloud, as ice crystals in cirrus clouds tend to have broader size distributions than the distributions of water droplets in water clouds [*Mitchell*, 2002]. For a given size distribution, the mean values of the extinction efficiency, absorption efficiency, asymmetry factor, and effective diameter (D_e) are defined as follows:

$$< Q_e > = \frac{\int_{L_{\min}}^{L_{\max}} Q_e(L) A(L) n(L) dL}{\int_{L_{\min}}^{L_{\max}} A(L) n(L) dL}, \tag{3.4}$$

$$< Q_a >= \frac{\int_{L_{\min}}^{L_{\max}} Q_a(L) A(L) n(L) dL}{\int_{L_{\min}}^{L_{\max}} A(L) n(L) dL}, \tag{3.5}$$

$$< g >= \frac{\int_{L_{\min}}^{L_{\max}} g(L) Q_s(L) A(L) n(L) dL}{\int_{L_{\min}}^{L_{\max}} Q_s(L) A(L) n(L) dL}, \tag{3.6}$$

$$D_e = \frac{3}{2} \frac{\int_{L_{\min}}^{L_{\max}} V(L) n(L) dL}{\int_{L_{\min}}^{L_{\max}} A(L) n(L) dL}, \tag{3.7}$$

where *V(L)* is the volume, and *A(L)* is the projected area of the particle with size of *L* (μm). Note that the definition of the effective particle size in Eq. (3.7) follows the work of *Foot* [1988], *Francis et al.* [1994], and *Fu* [1996], and is a generalization of the definition of the effective radius introduced by *Hansen and Travis* [1974] for water droplets. Furthermore, the definition of the effective particle size adopted in this study is consistent with that used in the operational MODIS cloud retrieval [*King et al.*, 2003; *Platnick et al.*, 2003].

Figure 3.1 shows the variation of the mean single-scattering properties for four particle sizes (D_e = 10, 20, 40 and 60 μm) as functions of the wavenumber of the incident radiation. Generally, the scattering properties of small particles are different from those of large particles because the scattering of radiation by small particles is closer to those for the regime of Rayleigh scattering [*Yang et al.*, 2003b]. Additionally, the variation of the averaged absorption efficiency for smaller particle sizes is similar to that of the imaginary part of ice refractive index [see *Warren*, 1984].

A line-by-line (LBL) radiative transfer model developed by *Heidinger* [1998] is used for calculating the background optical depths of clear-sky atmospheric layers due to the absorption by various radiatively important gases (e.g. H_2O, CO_2, O_3, N_2O, CO, CH_4,

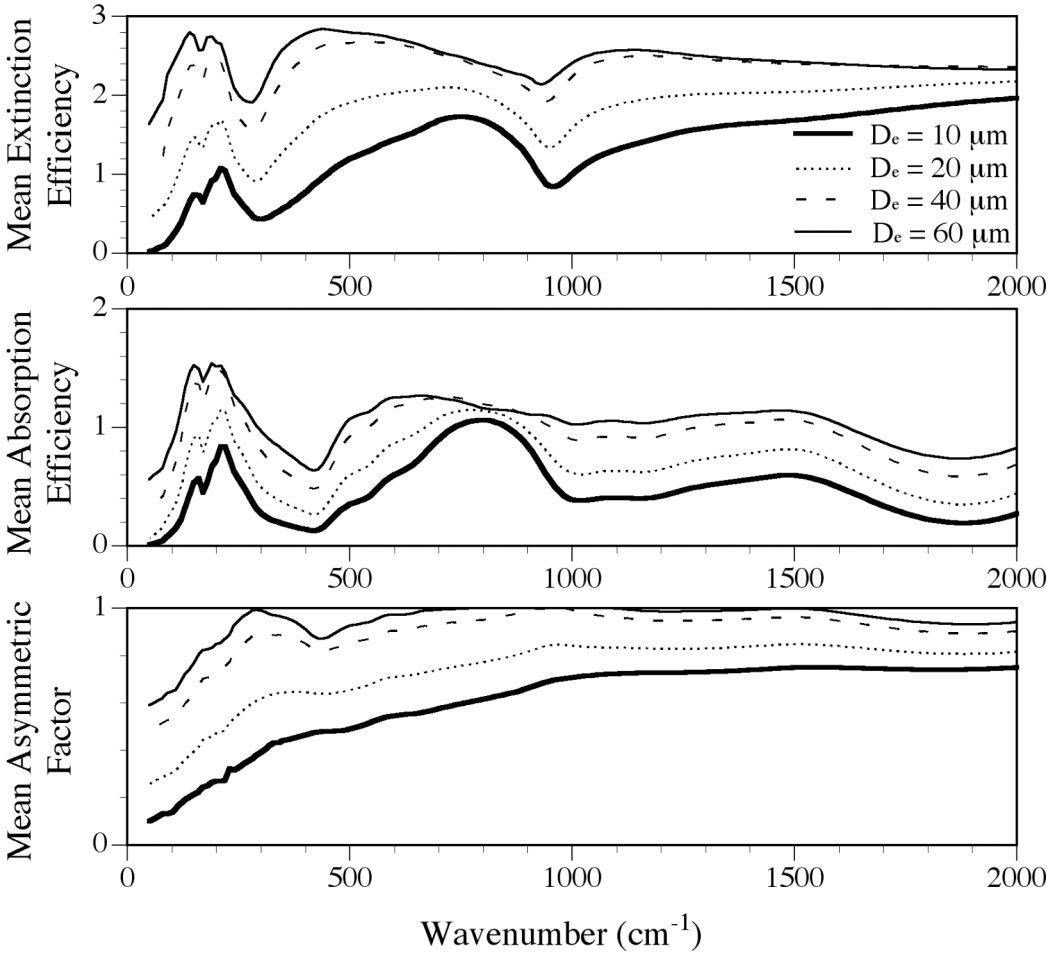

Figure 3.1 Averaged extinction efficiency, absorption efficiency and asymmetry factor for droxtal ice crystals with sizes of 10, 20, 40, and 60 μm in the spectral region from 50 to 2000 cm^{-1}.

etc.) with the line parameters from HITRAN-2000 [*Rothman et al.*, 1998]. The continuum absorption of water vapor and other gases are considered on the basis of the approach developed by *Tobin et al.* [1999]. The broadband outgoing TOA LW and WIN band radiances are calculated for each FOV using the DISORT [*Stamnes et al.*, 1988] implemented with 32 streams.

Following tradition in the literature, we specify the optical thickness of a cirrus cloud in reference to its value at a visible wavelength, that is, the cirrus optical thickness in the LW spectrum can be specified as follows:

$$\tau \approx \frac{< Q_e >}{2} \tau_{vis}, \tag{3.8}$$

where τ_{vis} is the visible optical depth, and we assume that the mean extinction efficiency of ice particles at a visible wavelength is 2. In Eq. (3.8), $< Q_e >$ is the mean extinction efficiency defined by Eq. (3.4) for a given infrared wavelength. As the TOA outgoing radiance depends on the cloud effective particle size, four effective diameters (D_e = 10, 20, 40 and 60 μm) are specified for the radiative transfer computations. Additionally, five values of the visible optical depth (τ_{vis} = 0.03, 0.1, 0.15, 0.2, and 0.3) are specified for each particle size. A library is developed for the outgoing radiances associated with the values of the visible optical depth τ_{vis} ranging from 0.03 to 0.3 and each effective particle size.

3.3 Results

Figure 3.2 shows the observed and calculated LW and WIN band radiances and also the corresponding relative differences for each FOV. Both the observed and calculated radiances are for clear-sky conditions, and their relative differences (ε) are defined as follows:

$$\varepsilon = \frac{(r_{obs} - r_{cal})}{r_{cal}} \times 100(\%), \tag{3.9}$$

where r is the outgoing either LW or WIN-channel radiance. The subscripts *obs* and *cal* indicate the observed and calculated quantities, respectively. The radiances computed for cloud-free FOVs are larger than their observed counterparts for both the CERES LW and WIN channels. We suggest that these differences can be explained in large part by the presence of thin cirrus. An important point to note is that the cloud mask is flagged as cloudy when the assumed optical thickness of the cloud is larger than approximately 0.2 ~ 0.3, and we use only CERES FOVs declared as cloud free in the SSF product; that is, thin cirrus clouds with optical thickness less than 0.3 might be missed in the cloud detection.

The relative differences defined in Eq. (3.9) in the case for the LW radiance are between -2.1% and -8.3% with a mean value of -4.2%. The CERES FOVs are separated by scene type into two categories: over ocean and over land [*Loeb et al.*, 2003b]. Large

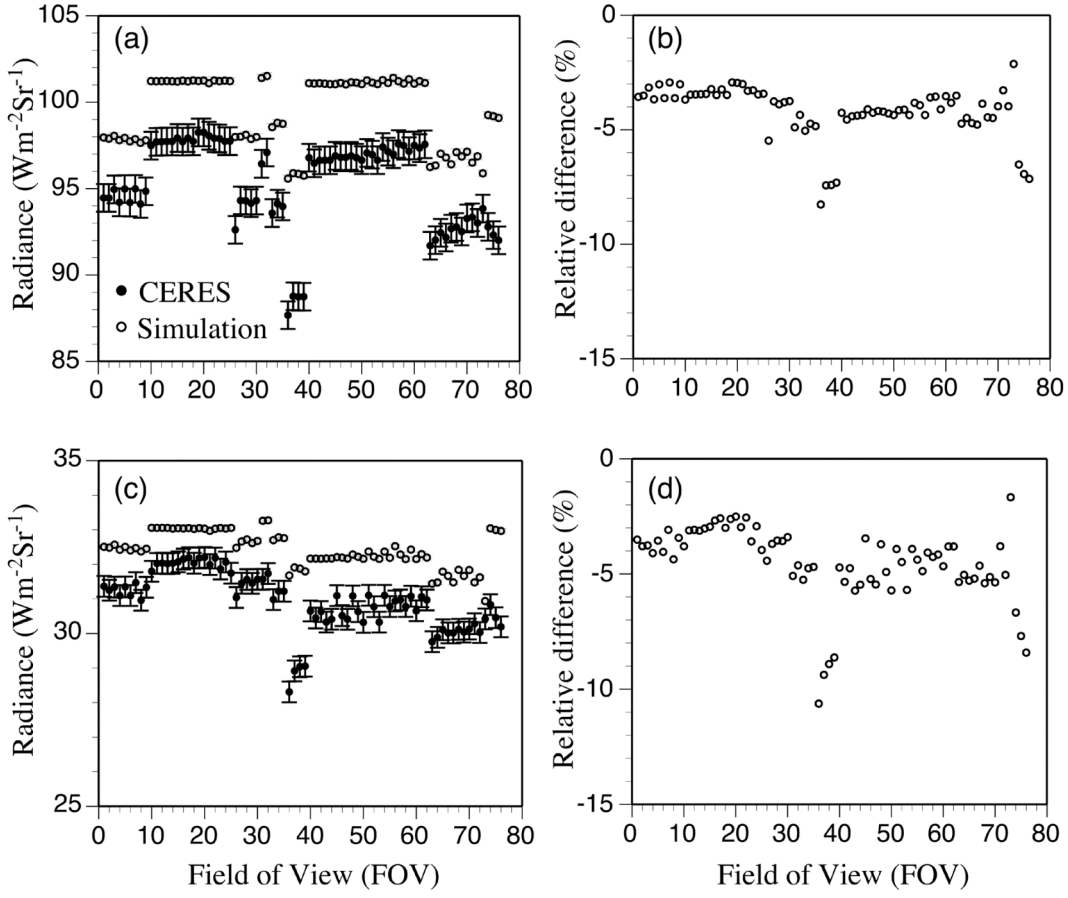

Figure 3.2 (a) The observed and calculated TOA outgoing longwave band radiances, (b) the relative differences for the computed and observed outgoing longwave band radiances, (c) the window band radiance, (d) relative differences for the computed and observed outgoing window band radiances. CERES FOVs flagged as cloud free have been chosen, which are located within 0.25 degree in both latitude and longitude over 4 atmospheric sounding locations during CRYSTAL-FACE period (July 2002). The error bars are 0.6 $Wm^{-2}Sr^{-1}$ for the LW band CERES measurement and 0.3 $Wm^{-2}Sr^{-1}$ for the WIN band, and the error bars are ±0.2% for the LW band and WIN band simulation.

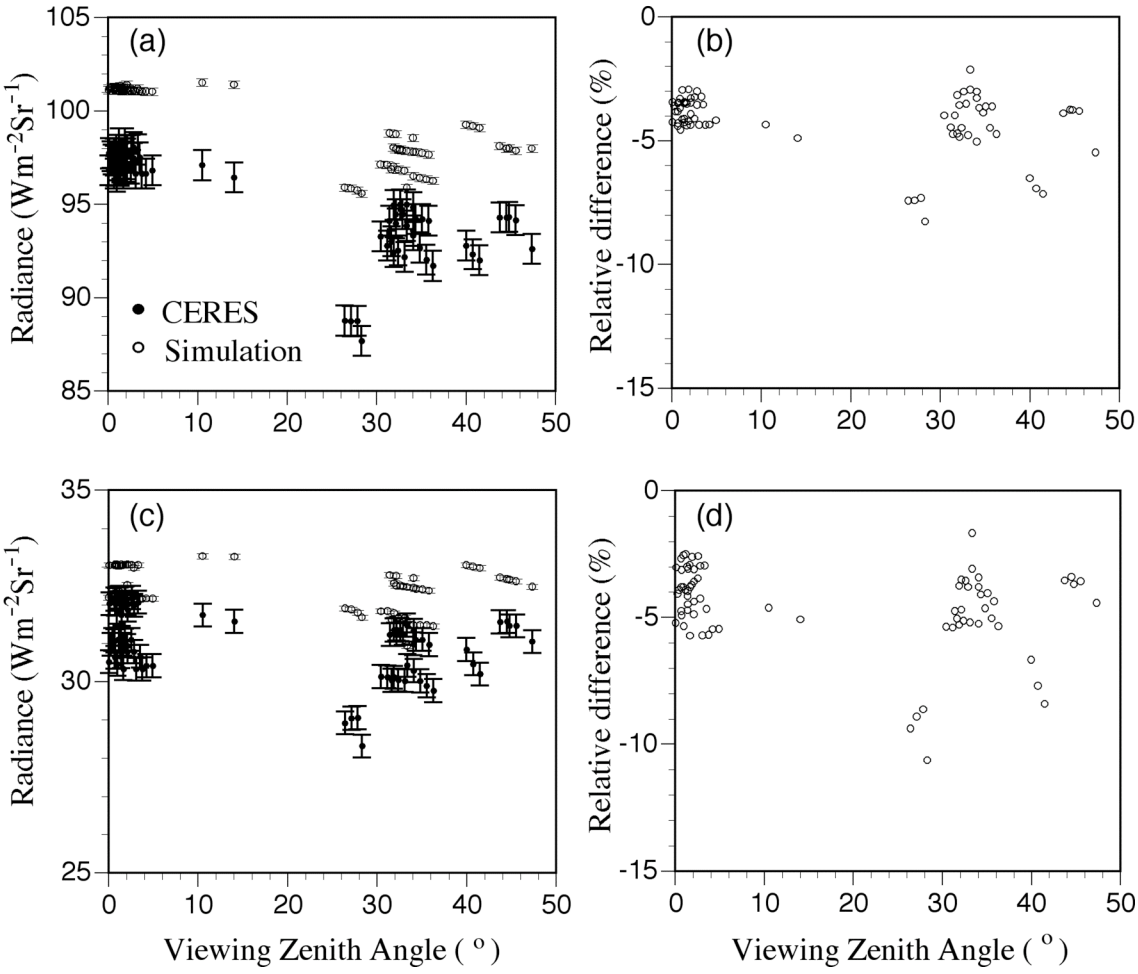

Figure 3.3 Similar to Fig. 3.2, except that the x-axis is for the viewing zenith angle in Fig. 3.3.

differences between the measurements and simulations occur for 7 nighttime FOVs whose scene types are over land. The relative differences are approximately -8.0% for 4 FOVs (2004070603 UTC, 36~39th FOV), and -7.0% for the other 3 FOVs (2004072903 UTC, 74~76th FOV). The relative differences in WIN channel radiances are between -1.7 and -10.6% with a mean value of -4.5%. The WIN channel radiances are calculated in the spectral range between 8.1 and 11.8 μm [*Loeb et al*., 2003b]. The CERES instrument accuracy requirements are 0.6 $Wm^{-2}Sr^{-1}$ for the LW band and 0.3 $Wm^{-2}Sr^{-1}$ for the WIN band [*Lee et al*., 1997], which are indicated as the error bars through Figs. 3.2-3.3 and also the error bars are indicated as ±0.2% for the longwave and window band simulation [*Loeb et al*., 2001].

Figure 3.3 shows both the observed and calculated LW and WIN channel radiances and their relative differences as functions of the viewing zenith angle. Both the measured and calculated radiances show the expected limb-darkening features. The angular distributions of the relative differences are similar for the LW and WIN channels. The maxima of the relative differences between the theoretical simulations and the corresponding CERES measurements seem to occur at the viewing zenith angles ranging from 25° to 30°. Evidently, the observed radiances for the pixels flagged as cloud free are smaller than the simulated data, and the relative differences can be as large as -8.3% and -10.6% for the LW and WIN band radiances, respectively, at a viewing zenith angle of ~28°. The outliers in the range between 25° and 30° may not imply something systematic but need to be further investigated with a larger set of data. These pixels are all over land. *Wilber et al.* [1999] adopted scene types from the

International Geosphere Biosphere Programme (IGBP) and developed surface emissivity maps to account for the scene dependence. Surface condition parameters in the CERES SSF products are obtained from their surface maps. Since a CERES FOV has a 20km spatial resolution at nadir, the heterogeneity of the surface emissivity over a CERES FOV could cause some errors in determining the surface parameters.

Figure 3.4 shows both the observed and calculated LW and WIN channel anisotropy factors and also their relative differences as functions of the viewing zenith angle. The anisotropy factors for the LW and WIN radiation are calculated from the following:

$$A(\theta) = \frac{\pi I(\theta)}{F}, \tag{3.10}$$

where θ is the viewing zenith angle, $I(\theta)$ and F are radiance and the corresponding flux at a reference level, respectively. The ADMs are used to obtain the LW and WIN broadband fluxes from the observed radiances. There are 45 ADMs for clear-sky daytime and nighttime conditions over various surfaces. As shown in Fig. 3.4 (the upper left panel for the LW channel and the lower panel for the WIN channel), the anisotropic factor decreases as the viewing zenith angle increases.

For the viewing zenith angles between 0° and 50°, the values of the anisotropic factors for the observed radiances are larger than those calculated except for some pixels for the viewing zenith angles larger than 27° for the LW bands. The relative differences between the measurements and simulations become smaller for both the LW and WIN

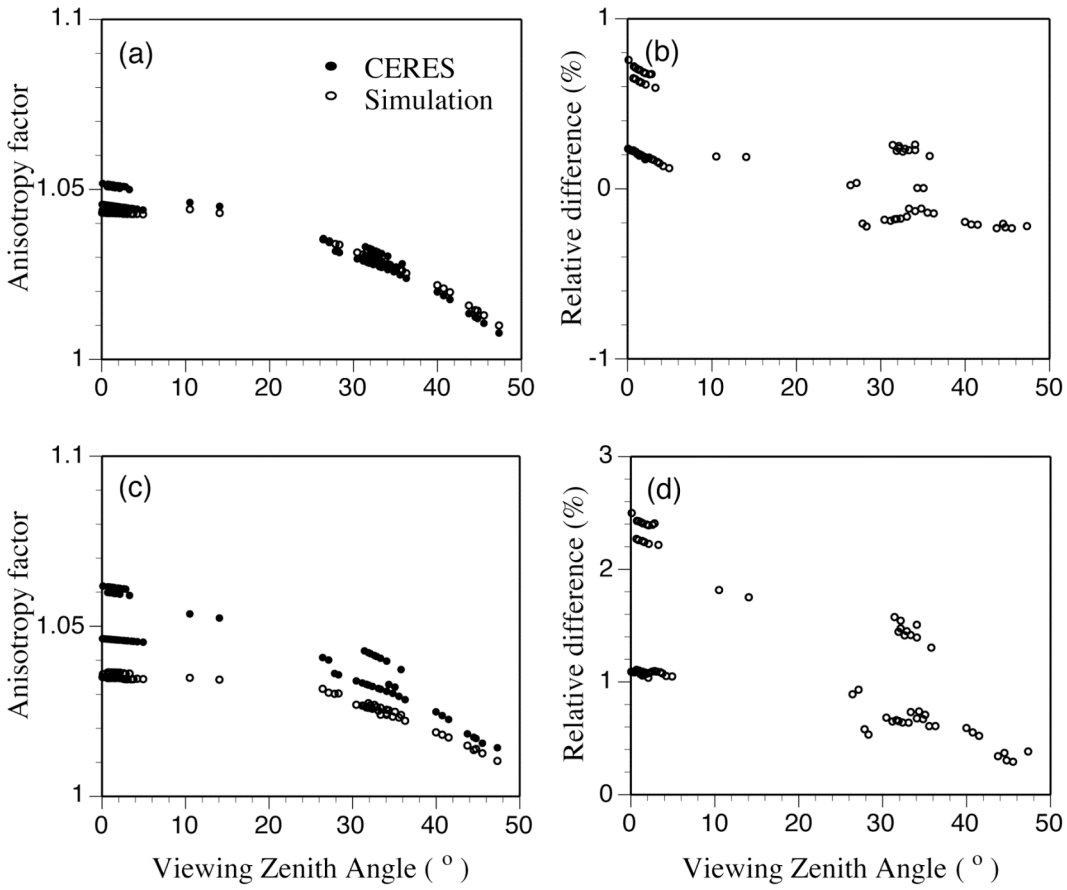

Figure 3.4 Anisotropy factors provided by the CERES SSF products in comparison with the present simulations. Panel (a) is for the longwave band, and panel (b) is for the window band.

bands as the viewing zenith angle approaches to 50°. The relative differences of the anisotropy factor for the LW band are between -0.23% (at θ = 45.5°) and 0.76% (at θ = 0.1°) with a mean value of 0.19%, and for the WIN band between 0.29% (at θ = 45.5°) and 2.5% (at θ = 0.1°) with a mean value of 1.26%. The TOA flux for a clear sky might be underestimated with a larger anisotropy factor. As an example using a typical clear-sky LW flux of 300 Wm^{-2}, if the CERES anisotropic factor is overestimated by a typical value of 0.2% because of potential cirrus contamination, the LW flux would be underestimated by approximately 0.2%, or 0.6 Wm^{-2}, in the regions where these cirrus clouds are present. *Loeb et al.* [2003a] showed that the difference between direct integration and the flux converted from the radiance using the LW ADMs is below 0.5 Wm^{-2}. The values of the LW anisotropy factor in the present study show quite small relative differences, which means that the differences of the anisotropy factor values between the CERES SSF products and the simulated could be within the uncertainty range of the ADM models.

Figure 3.5 (a) shows the inferred optical depth from minimizing the differences between the observed and calculated LW radiance as a function of the viewing zenith angle. The inferred optical thickness for each FOV is essentially below 0.3 for each D_e value. For more than 70 of the FOVs, the optical thicknesses are below 0.2, which also depend on D_e. For the viewing zenith angles between 25° and 30°, the optical thicknesses are larger than those at other angles. This is not unexpected, given the results of Fig. 3.3 (i.e. the difference between the observed and calculated radiance is large). Fig. 3.5 (b) shows the inferred cirrus optical thickness obtained by minimizing the

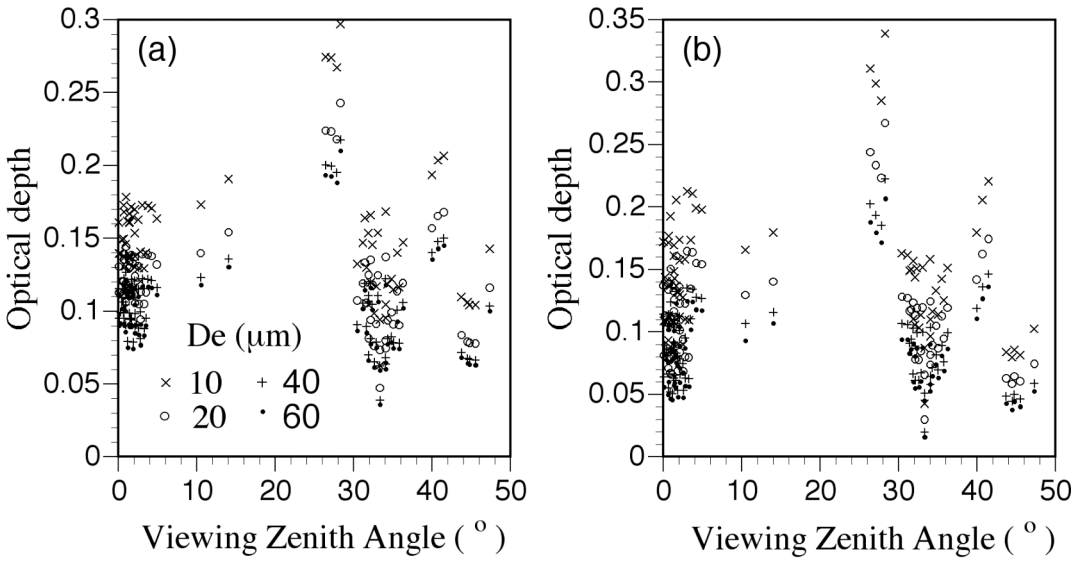

Figure 3.5 Optical depths of thin cirrus retrieved from the difference of the observed radiances and the simulated counterparts by assuming various effective particle sizes. Panel (a): retrieval from use of the longwave band data; panel (b) retrieval from use of the window band.

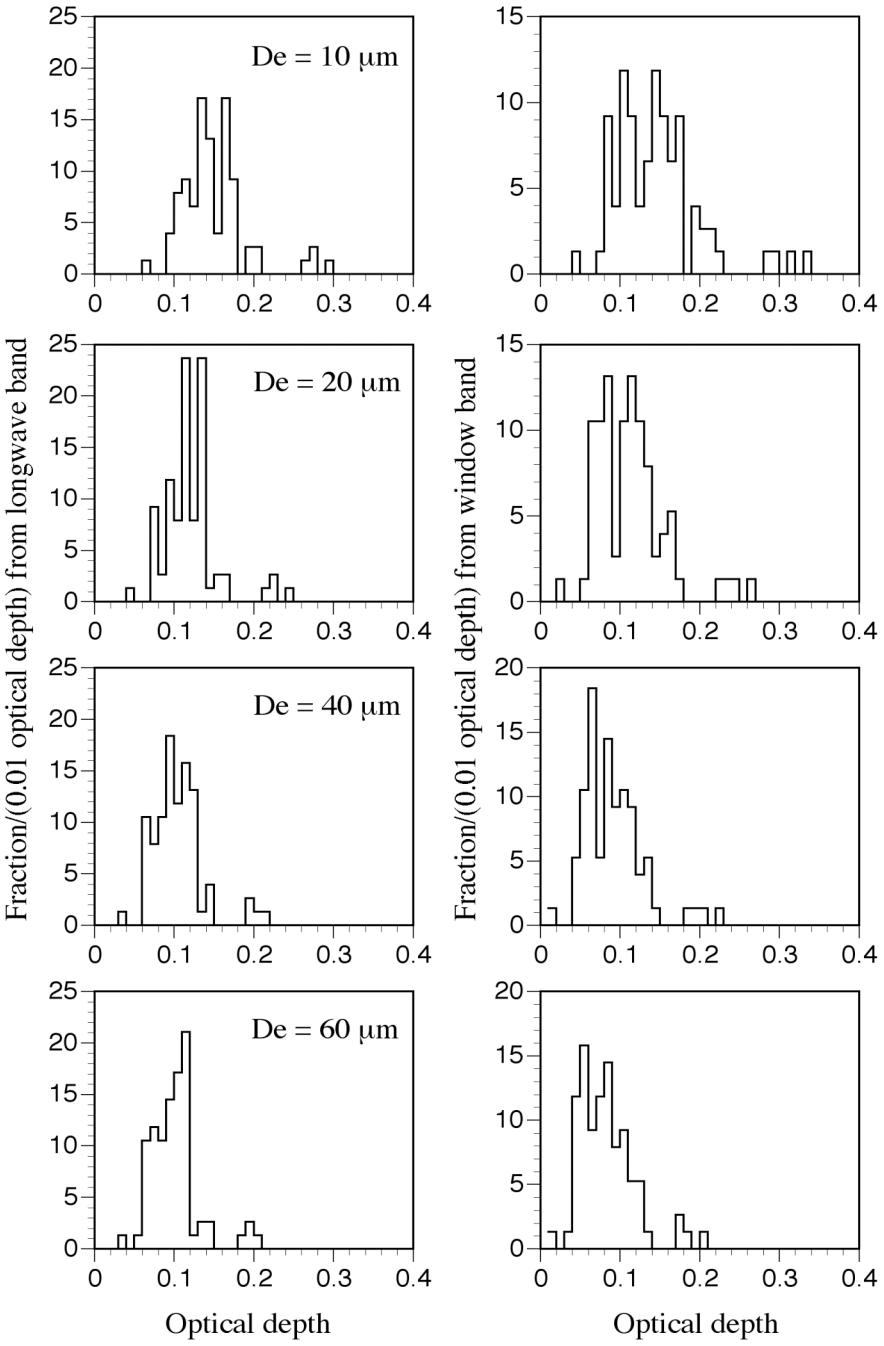

Figure 3.6 Distributions of the optical depths of thin cirrus clouds retrieved from the differences of the observed and simulated radiances by assuming various effective particle sizes. Left panels are based on the longwave band data; right panels are based on the window band data.

differences between the observed and the calculated WIN channel radiances as a function of the viewing zenith angle. The optical thickness pertaining to each FOV tends to be below 0.3 with an exception of just two FOVs (τ_{vis} = 0.31 and 0.34) when D_e = 10 μm. As the effective diameter increases, the values of the optical thickness converge for both the LW and WIN channels. This feature is associated with the variation of the averaged single-scattering properties of droxtals shown in Fig. 3.1.

In Fig. 3.6, the left panels show the histograms of cirrus optical thicknesses inferred from the differences between the observed and calculated LW radiances. As the effective diameter increases, the distribution of the optical thickness is shifted towards smaller values (see Table 3.1) and the distribution narrows. The optical thickness distribution is similar to that of *Dessler and Yang* [2003; see their Fig. 3] for the frequent occurrence of thin cirrus clouds. The right panels in Fig. 3.6 show the distributions of optical thicknesses inferred from the differences between the observed and calculated WIN channel radiances. Similar to the cases pertaining to the left panels in Fig. 3.6, the distribution of the optical thickness derived from the WIN band also shifts to smaller values with an increase of the effective diameter (see Table 3.1). The peaks of the frequency distributions of the optical thickness are shifted to slightly smaller values.

Figure 3.7 shows clear-strong and clear-weak percent coverage of each CERES FOV. In the CERES cloud mask, there are several clear subcategories such as clear-strong and clear-weak. The CERES SSF products provide cloud mask information on clear-strong (or, weak) percent coverage. Note that for the CERES data, the clear-strong (or weak) percent coverage is a weighted percentage of clear-strong (or weak) MODIS

Table 3.1 The average optical depths of thin cirrus clouds retrieved from the differences of the observed and calculated longwave and window band radiances for four effective diameters.

	$D_e = 10\,\mu m$	$D_e = 20\,\mu m$	$D_e = 40\,\mu m$	$D_e = 60\,\mu m$
Longwave	0.149	0.120	0.105	0.100
Window	0.146	0.113	0.091	0.083

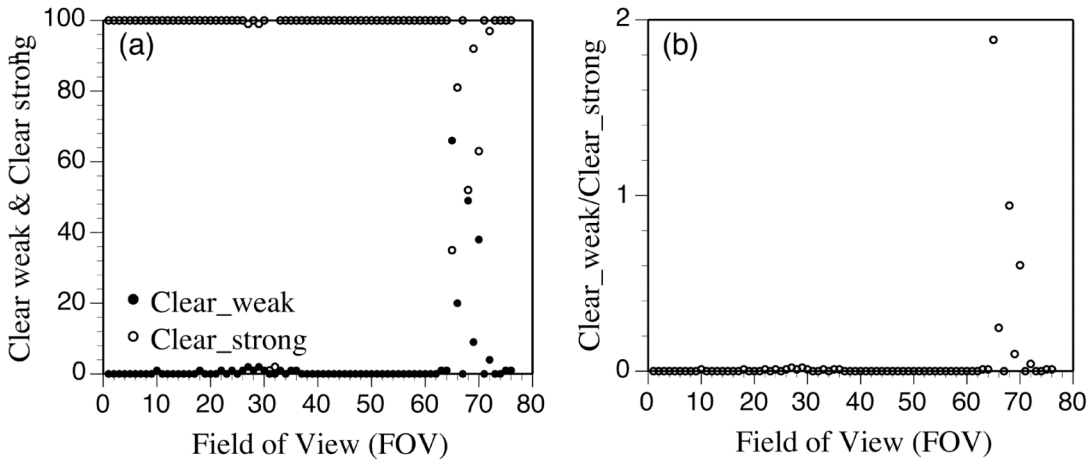

Figure 3.7 (a) Clear-strong coverage percent and clear-weak coverage percent and (b) the ratio of clear-weak coverage to clear-strong coverage.

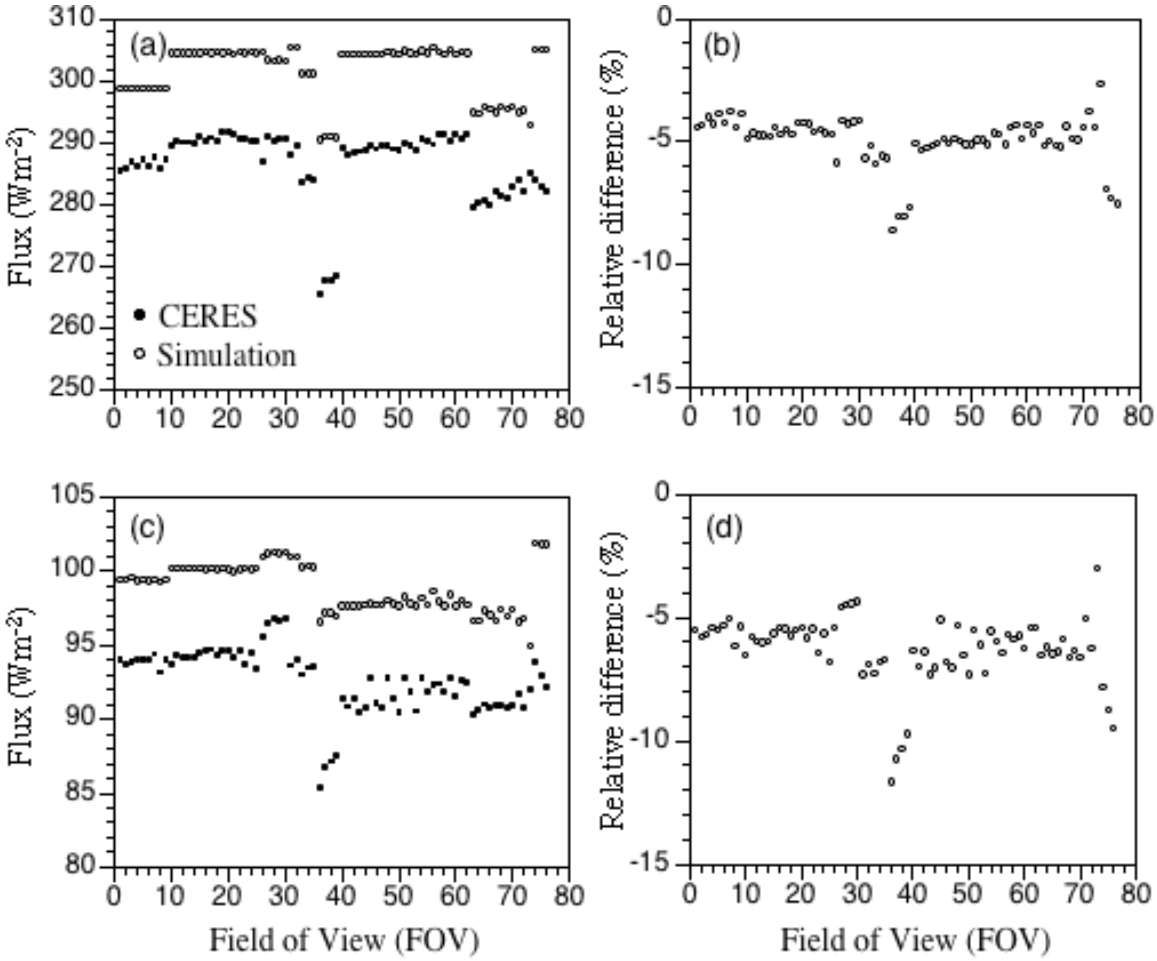

Figure 3.8 (a) The observed and calculated TOA outgoing longwave band flux, (b) the relative differences for the computed and observed outgoing longwave band flux, (c) the window band flux, (d) relative differences between the computed and observed outgoing window band flux.

pixels within the CERES FOV. For the data set used in this study, 70 FOVs out of the 76 FOVs have over 90% clear-strong coverage, and 66 FOVs have 100% clear-strong coverage. The ratio of clear-weak percent coverage to clear-strong percent coverage is almost zero except for a few FOVs.

Figure 3.8 shows the observed and calculated LW and WIN band flux (Wm^{-2}) and also the corresponding relative differences for each FOV. Both the observed and calculated flux are for clear-sky conditions which are the same as in Fig 3.2. The flux computed for cloud-free FOVs are larger than their observed counterparts for both the CERES LW and WIN channels as expected in Fig 3.2. We suggest that these differences be explained in large part by the presence of thin cirrus. At this moment, the flux difference is compared between the observed and simulated values to see how much the thin cirrus clouds affect the flux estimation. Since CERES FOVs declared as cloud free in the SSF product are used in this study, which might be missed in the cloud detetection, we assume the flux difference is from the thin cirrus clouds missed in the observation. The average value of the observed flux for total 76 pixels is 286.74 Wm^{-2}, and the simulated average value is 301.71 Wm^{-2} in LW channels which means a 14.97 Wm^{-2} deficit caused by missed thin cirrus clouds. In WIN channels, the observed average flux is 92.65 Wm^{-2}, and the simulated average value is 98.88 Wm^{-2}. Even in WIN channels the flux difference is 6.23 Wm^{-2}. The difference between the observed and simulated flux in LW and WIN channels inferred in this study is comparable to the effects when the cloud optical thickness or cloud height are increased 50% according to the CERES report (http://asd-larc.nasa.gov/ceres/broucher.html).

3.4 Sensitivity study

The radiative transfer simulations require knowledge of the surface temperature and emissivity, and the vertical atmospheric temperature and water vapor profiles. We performed various sensitivity studies for clear-sky conditions with a ±1 K bias of the surface temperature, a ±2% bias of the surface emissivity, a ±1 K bias of the vertical sounding temperature, and a ±5% bias of water vapor in the lower atmospheric layers in conjunction with a ±50% bias of water vapor in the upper atmospheric layers.

Figures 3.9-3.12 show both the observed and calculated radiances as well as their relative differences for both the LW and WIN bands. The radiances are calculated with a ±2% bias of the surface emissivity (Fig. 3.9). Although a ±2% bias of the surface emissivity is considered, the calculated LW and WIN channel radiances are larger than their observed counterparts. The average relative differences of the observed and calculated LW (WIN) channel radiance are -3.57% (-3.11%) with a -2% bias of the surface emissivity and -4.6% (-5.5%) with a +2% bias of the surface emissivity. The CERES instrument accuracy requirements are the same as those in Fig. 3.2, which are indicated as the error bars in Figs. 3.9-3.12.

In Fig. 3.10 the LW and WIN channel radiances are calculated with a ±1 K bias of the surface temperature. The average relative difference of the observed and calculated LW (WIN) channel radiances are –3.62% (-3.22%) with a –1K bias of the surface temperature and -4.74% (-5.68%) with a +1K bias of the surface temperature.

The effects of a +1 K (-1 K) bias in the surface temperature and a +2% (-2%) bias in the surface emissivity are similar for both the LW and WIN channel radiances.

The LW and WIN channel radiances are calculated assuming a ±1 K bias in a given vertical temperature profile (Fig. 3.11). The average relative difference in the LW (WIN) channel radiances between the observed and calculated values is –3.47% (-4.29%) with a –1K bias of the temperatures and –4.9% (-4.76%) with a +1 K bias of temperatures. A +1K (-1K) bias of the vertical temperature profile causes the changes in the LW channel radiances with a similar order to the case for a +2% (-2%) bias of the surface emissivity, and little influence on the WIN channel radiances.

The LW and WIN channel radiances are calculated with a ±5% bias in the water vapor amount for lower tropospheric layers in conjunction with a ±50% bias in the water vapor amount for upper tropospheric layers (Fig 3.12). An upper (lower) tropospheric layer in this study is defined as one in which the temperature is below (above) 273 K. The average relative difference of the LW (WIN) channel radiances between the observed and calculated values is –6.12% (-4.83%) with a negative bias of water vapor and –2.87% (-4.25%) with a positive bias of water vapor. Both the negative (positive) bias of water vapor and a +1K (-1K) bias in the vertical temperature profile cause some changes on the LW channel radiance but have little effects on the WIN channel radiance. Since the radiance in the window region is less sensitive to water vapor amount, the variability of the radiance in the LW channel is larger than that in the WIN channel.

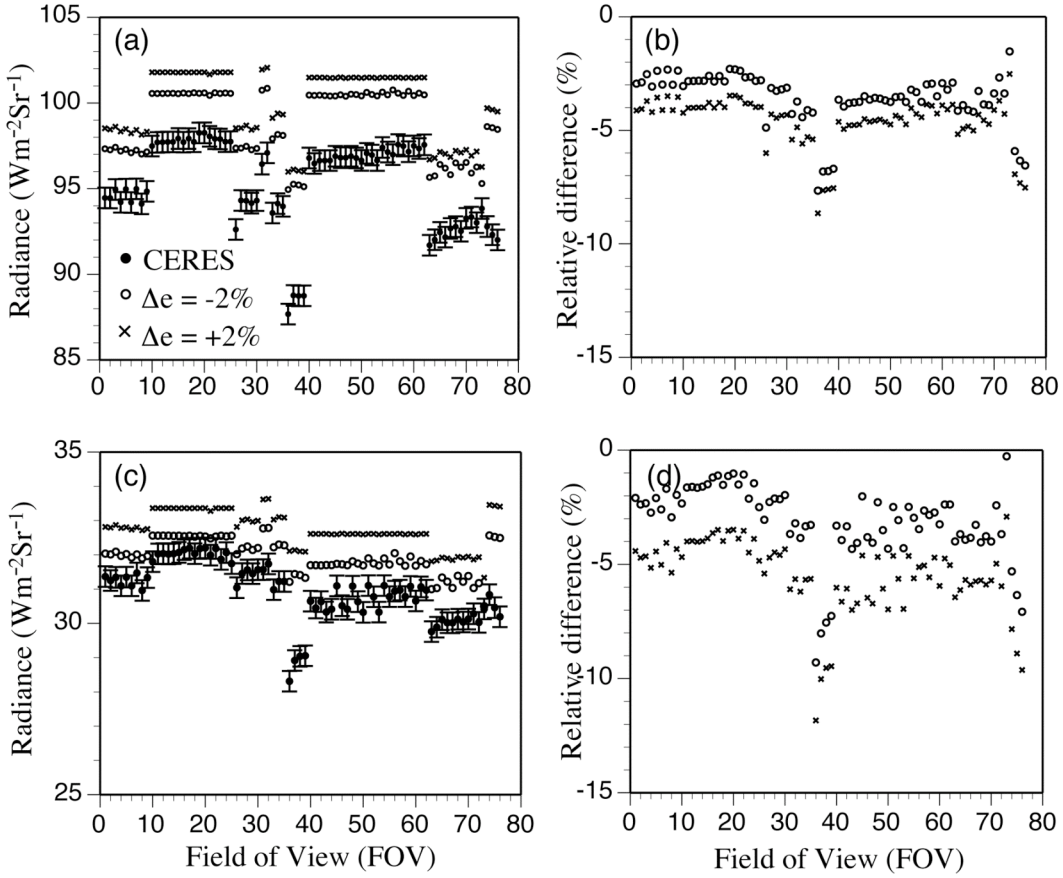

Figure 3.9 (a) The observed and calculated TOA outgoing longwave band radiances, (b) the relative differences for the computed and observed outgoing longwave band radiances, (c) the window band radiance, (d) relative differences between the computed and observed outgoing window band radiances. The radiances are calculated with a bias of ±2% in the surface emissivity. The error bars 0.6 $Wm^{-2}Sr^{-1}$ for the longwave band CERES measurement and 0.3 $Wm^{-2}Sr^{-1}$ for the window band.

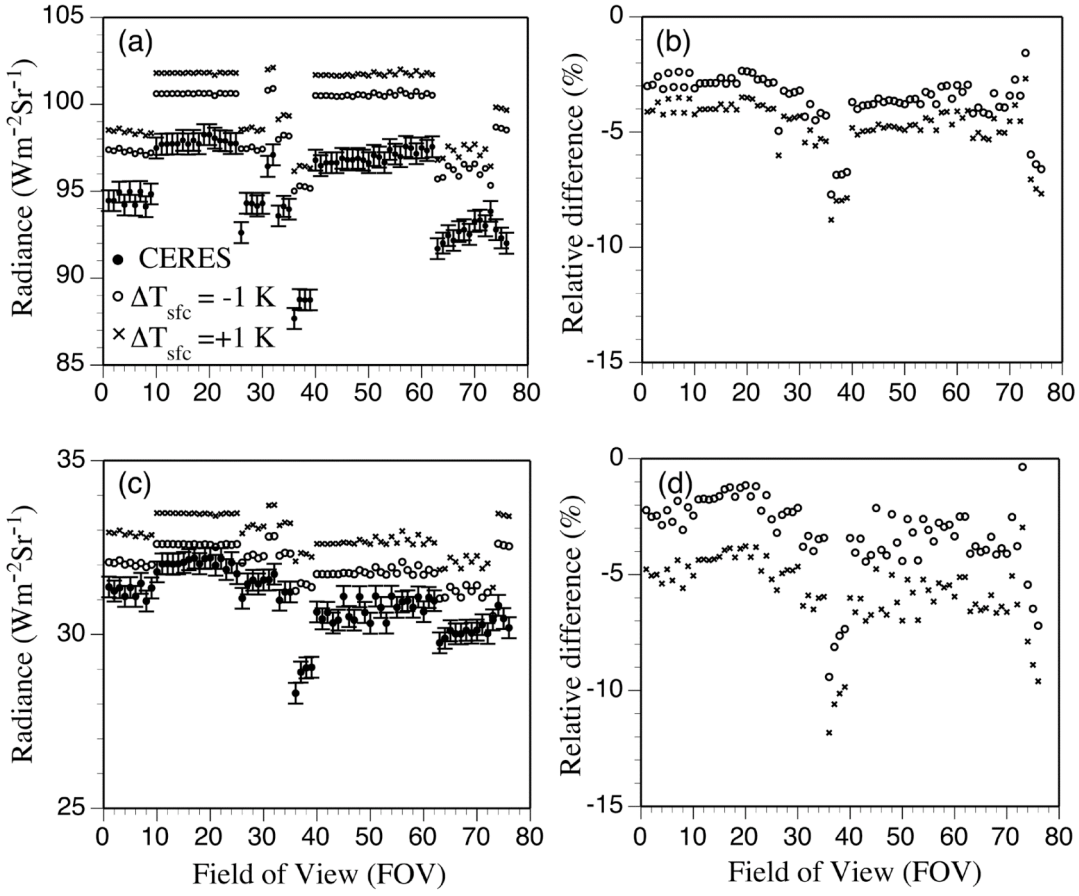

Figure 3.10 Similar to Fig. 3.9, except that the radiances are calculated with a bias of ±1 K in the surface temperature.

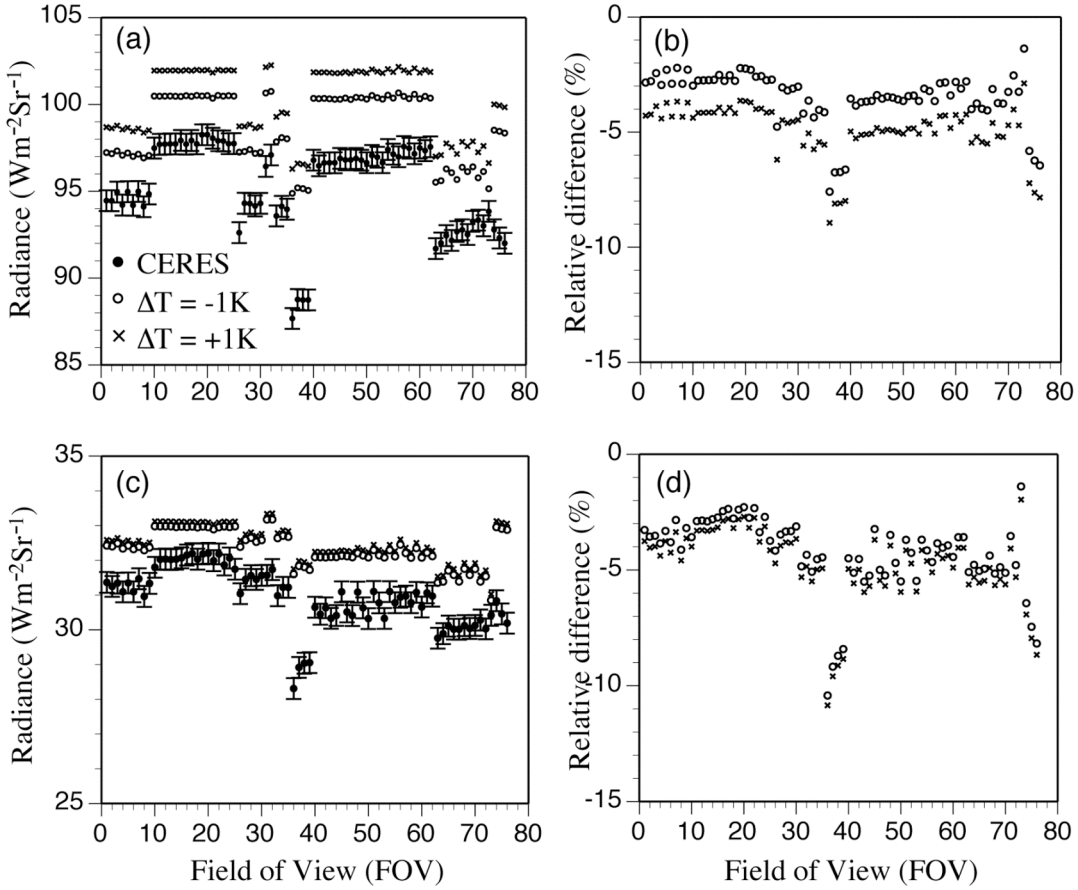

Figure 3.11 Similar to Fig. 3.9, except that the radiances are calculated with a bias of ±1 K in the vertical atmospheric temperature profile.

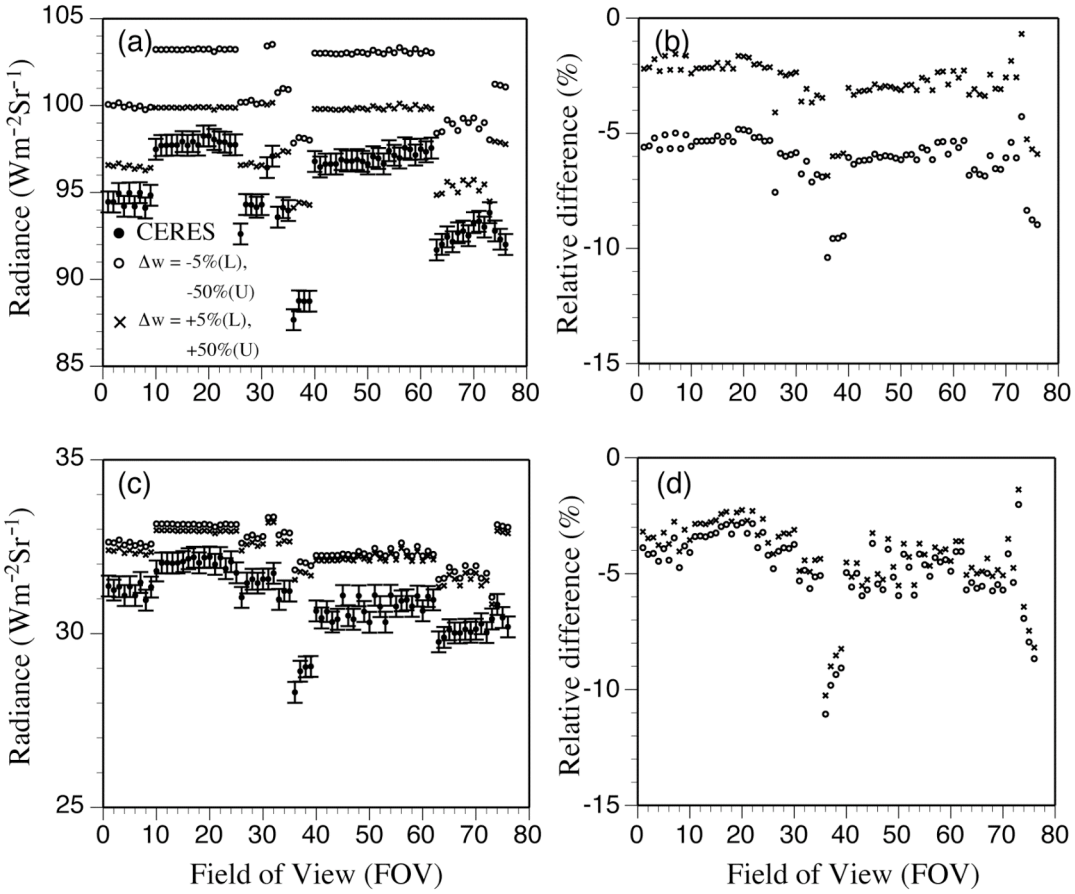

Figure 3.12 Similar to Fig. 3.9, except that the radiances are calculated with a bias of ±5% in lower atmospheric water vapor amount in conjunction with a ±50% in upper atmospheric water vapor amount. Biases of the same sign are considered together. (L) indicates the lower troposphere, and (U) indicates the upper troposphere.

CHAPTER IV

RETRIEVAL OF CLOUD PROPERTIES USING ATMOSPHERIC INFRARED SOUNDER (AIRS)

4.1 Background

The Atmospheric Infrared Sounder (AIRS) instrument is a spaceborne hyperspectral infrared radiometer aboard Aqua, one of the family members of the NASA EOS A-train constellation. The AIRS instrument is based on a heritage from the High Resolution Infrared Radiation Sounder (HIRS) that has been operational on NOAA platforms for more than 20 years. AIRS provides a substantial technological improvement in capability with its extensive calibration as compared with HIRS [*Strow et al.*, 2003b; *Gaiser et al.*, 2003; *Pagano et al.*, 2003].

The vertical profiles of temperature and water vapor amount can be obtained from the measurements acquired by the AIRS, the Advanced Microwave Sounding Unit (AMSU) and Humidity Sounder for Brazil (HSB), which constitute the operational sounding suite on Aqua [*Aumann et al.*, 2003; *Susskind et al.*, 2003]. In addition to the temperature and water vapor vertical profiles, the AIRS products also include the atmospheric profiles of minor gases, which are necessary for accurate radiative transfer simulations. Although the retrieval of cloud properties has not been a focus of the AIRS science team to date, AIRS provides an unprecedented opportunity to retrieve cloud properties for both daytime and nighttime with its high-spectral-resolution measurement capabilities.

The CO_2 slicing method originally developed by *Smith et al.* [1974] and *Chahine* [1974] can be used to derive cloud top pressure and effective cloud amount (cloud fraction multiplied by cloud emissivity). Note that this method has been successfully implemented for measurements from various satellite instruments including the Geostationary Operational Environmental Satellite (GOES) VISSR Atmospheric Sounder (VAS; VISSR is the Visible and Infrared Spin Scan Radiometer) [*Wylie and Menzel*, 1989], HIRS [*Wylie and Menzel*, 1999], and MODIS [*Platnick et al.*, 2003]. The physical basis of this method is that a set of channels in the CO_2–15 μm absorbing band can be used to sense cloud top pressure because of the different weighting functions of these channels.

Huang et al. [2004] suggested another approach referred to as the Minimum Local Emissivity Variance (MLEV) method to retrieve cloud top pressure and effective cloud amount. MLEV seeks the optimal value of effective cloud amount with varying cloud top pressure. The capabilities of the MLEV and CO_2 slicing methods have been compared and investigated recently [*Antonelli et al.* 2001]. Furthermore, the one-dimensional variational method (1-DVAR) has been suggested to calculate cloud top pressure and effective cloud amount on the basis of using an iterative method to find a solution using both MODIS and AIRS products [*Li et al.*, 2004]. Although it is effective to retrieve the cloud properties using both MODIS and AIRS products as suggested by *Li et al.* [2004], initial guess values with reasonable accuracy are needed for deriving the solution.

To infer cloud optical thickness and effective particle size, several methods have been suggested which are based on visible, near IR, and IR channels [*Heidinger* 2003; *Minnis et al*. 1993a,b; *Nakajima and King* 1990]. A method based on visible and near-infrared channels is applicable only for the daytime. To overcome this shortcoming, an alternative approach is to retrieve cloud optical and microphysical properties (i.e., cloud optical thickness and effective particle size) solely from infrared channels.

The method suggested in this dissertation for retrieving cloud optical thickness and effective particle size is based entirely on the infrared measurement, which has three distinct advantages. First, it is applicable for both daytime and nighttime. As a result, a time-series analysis of cloud properties will be possible. Second, this algorithm does not need the initial guess values with reliable quality to derive the final solution. Third, once the atmospheric environmental profiles for a pixel are set up, such as atmospheric temperature and water vapor profiles, cloud optical properties can be retrieved using only infrared channels.

4.2. Data availability and method

4.2.1. AIRS products

AIRS is a radiometric instrument on the EOS Aqua platform with 2378 channels spanning from 3.7 to 15.4 μm. The Aqua platform was launched in May 2002. AIRS level-1b radiances and level-2 standard and support products are available for public access through the NASA Distributed Active Archive Center (DAAC). One granule of AIRS level-1b infrared radiance includes 90 × 135 fields of view (FOVs) with a nadir

spatial resolution of 13.5 km. The level-2 product is based on analyses of the 3 × 3 FOVs of the level-1b infrared radiances which are degraded to a lower resolution of the microwave data. Both the level-1b and level-2 data are used in this research. Note that the level-2 products contain sufficient information (e.g., the atmospheric temperature, water vapor, and minor gas profiles) for forward radiative transfer simulations involved in retrieving cloud properties. Nine FOVs (13.5 km at nadir) in level-1b products share the same vertical profiles, since vertical profiles of temperature and water vapor are supplied on the basis of the level-2 product resolution (45 km at nadir). To compare the inferred AIRS results and the corresponding MODIS products, the collocation of the MODIS pixels and the AIRS level-1b grid is necessary.

In this dissertation, an ocean area (E145˚ - E170˚, S5˚ - N2˚) is selected because the surface parameters such as surface emissivity and temperature are substantially variable over land. Over this area, 4-6 granules are selected on the 15th of each month (except June; 16th June is selected) between October 2004 and September 2005 for a total of 52 granules. Cloud top pressure, effective cloud amount, and cloud phase are calculated for these 52 AIRS granules, and then cloud optical thickness and effective particle size are retrieved for the pixels out of 52 granules within the selected ocean area. In this study, March, April, and May are considered as spring; June, July, and August are considered as summer; September, October, and November are considered as autumn; and December, January, and February are considered as winter.

4.2.2 Single scattering properties of ice and water clouds

A radiative transfer model is required for the simulation of the effect of cloud properties on radiation field involved in implementing a retrieval algorithm. The fast infrared radiative transfer model (FIRTM) developed at Texas A&M University is employed in this study. The FIRTM is applicable to the simulation of the infrared radiance at TOA for cloudy atmospheres with one-layered clouds (either an ice cloud or a water cloud) or two-layered clouds (a water cloud topped with an ice cloud) [*Wei et al.*, 2004; *Niu et al.*, 2006]. Ice clouds are almost exclusively composed of various nonspherical ice crystals spanning from pristine hexagonal ice columns and plates to highly irregular geometric morphologies. In the current FIRTM, it is assumed that the midlatitude cirrus clouds consist of 50% bullet rosettes, 25% hollow columns, and 25% plates when the maximum dimension of an ice particle is smaller than 70 μm. For ice particles larger than 70 μm, it is assumed that bullet rosettes and aggregates dominate the particle size distribution, where the particles are composed of 30% aggregates, 30% bullet rosettes, 20% hollow columns, and 20% plates [*King et al.*, 2004].

In this study, six particle shapes are considered: droxtals, bullet rosettes, solid columns, hollow columns, plates, and aggregates. *Yang et al.* [2005] have developed a database for the scattering properties of various ice crystals for a spectral region spanning from 3 μm to 100 μm. *Baum et al.* [2005b] reported a new habit distribution acquired during several field campaigns including FIRE-I (the First ISCCP Regional Experiments; ISCCP refers to the International Satellite Cloud Climatology Project) in Madison, WI in 1986, FIRE-II in Coffeyville, KS in 1991, and ARM (Atmospheric

Radiation Measurement) in the spring of 2000 near Lamont, OK, for the midlatitude region, and CRYSTAL-FACE (the Cirrus Regional Study of Tropical Anvils and Cirrus Layers) over Florida in 2002 and TRMM (the Tropical Rainfall Measuring Mission) in Kwajalein, Marshall Islands (Kwajalein Experiment: KWAJEX) in 1999 for the tropical area. Based on the new ice crystal habit and the scattering database, an update of the look-up libraries of the cirrus reflectance and transmittance involved in the FIRTM is carried out in this research.

The habit distribution for ice particles is divided into several regions, i.e., D < 60 μm (100% droxtal), 60 < D < 1000 μm (15% bullet rosettes, 50% solid columns, 35% plates), 1000 < D < 2500 μm (45% hollow columns, 45% solid columns, 10% aggregates), and 2500 < D < 9500 μm (97% bullet rosettes, 3% aggregates). The gamma distribution [*Hansen and Travis*, 1974] is used for both ice and water clouds as the particle size distribution, which is given in Eq. (3.1). The effective radius and the effective variance (V_{eff}) in the gamma distribution are specified by Eqs. (3.2) and (3.3), respectively. The effective variance for various water clouds lies between 0.111 and 0.193 [*Hansen*, 1971]. In this study, variance values of V_{eff} = 0.2 and 0.15 are used for ice clouds and water clouds, respectively. It is reasonable to choose an effective variance larger for an ice cloud than for a water cloud, as ice crystals in ice clouds tend to have broader size distributions than the distributions of water droplets in water clouds [*Mitchell*, 2002]. For a given size distribution, the mean values of the extinction efficiency, absorption efficiency, asymmetry factor, and effective diameter (D_e) are shown in Eqs. (3.4)-(3.7).

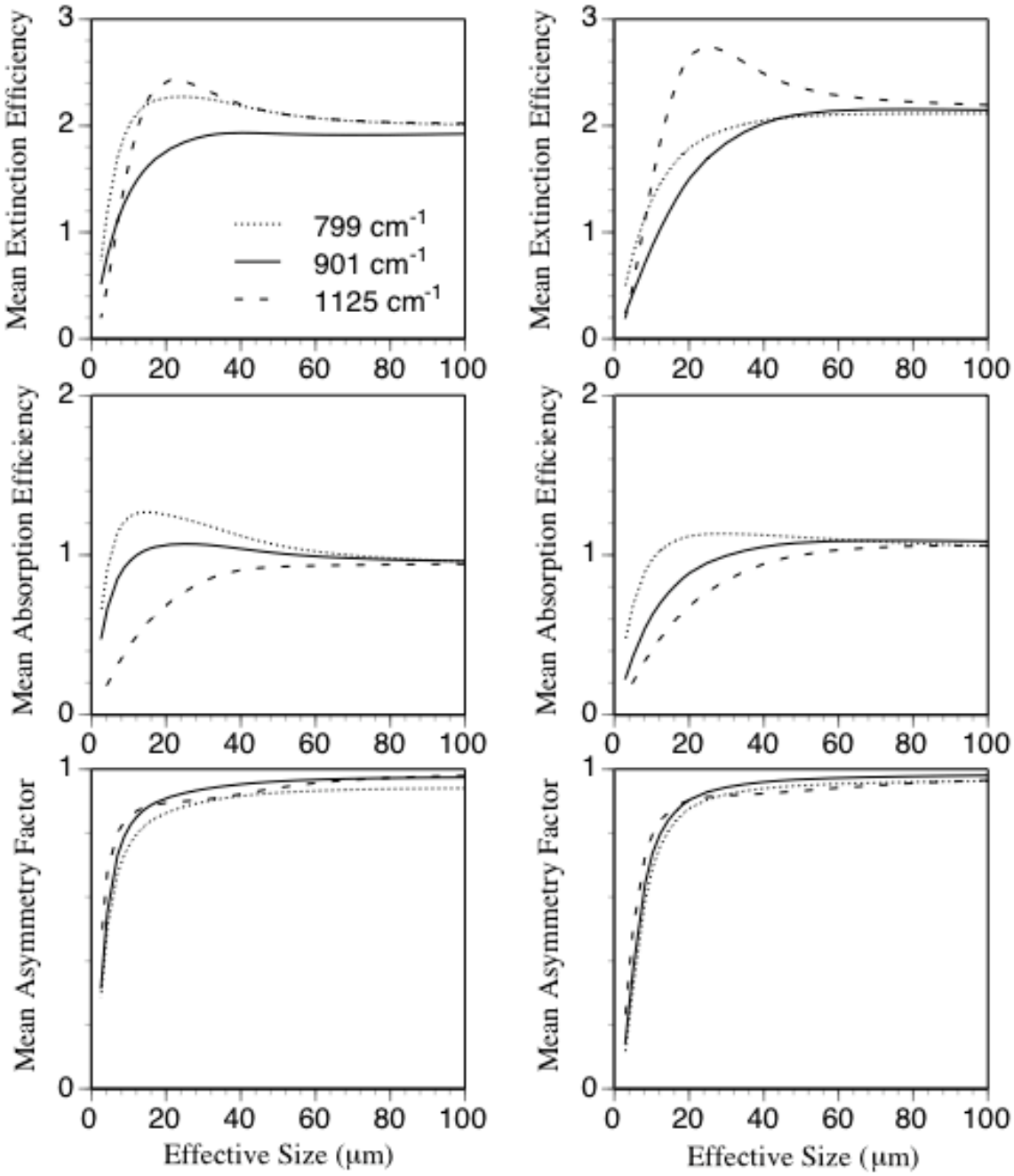

Figure 4.1 Mean single scattering properties of ice clouds (left panels) and water clouds (right panels).

Figure 4.1 shows the mean extinction efficiency, mean scattering efficiency, and mean asymmetry factor at three wavenumbers. For small effective particle sizes, all the single-scattering parameters are small, whereas the mean values of absorption efficiency and asymmetry factor converge to one, and mean extinction efficiency converges to two, as the effective particle size becomes larger.

4.2.3 Lookup libraries of transmittance and reflectance for ice and water clouds

The scattering effects are not negligible when cloud particles are involved. Thus to compute the cloud transmittance and reflectance, scattering effects must be included. The transmittance and reflectance of clouds are functions of cloud optical depth, effective particle size, wavelength (or wavenumber), and viewing zenith angle. In this study, the lookup libraries for the transmittance and reflectance of clouds are developed on the basis of the mean single scattering properties of ice and water clouds (section 4.2.2) using the Discrete Ordinate Radiative Transfer (DISORT) code (Stamnes et al. 1988). Cloud optical depth for a given infrared channel can be approximated as $\tau \approx \frac{< Q_e >}{2} \tau_{vis}$ (given in Eq. (3.8)). In this study the Henyey-Greenstein (H-G) phase function is used as an approximation of the true phase function at the AIRS infrared channels [*Turner et al.*, 2003; *Garrett et al.*, 2002; *Wei et al.*, 2004] given by,

$$P_{HG} = \frac{1-g^2}{(1+g^2+2g\cos\theta)^{\frac{3}{2}}}$$

$$= \sum_{l=0}^{N} (2l+1) g^l P_l(\cos\theta), \qquad (4.1)$$

where g is the asymmetry factor of the phase function pertaining to cloud particles. θ is scattering angle, $P_l(\cos\theta)$ is the l^{th} Legendre polynomial, N is the stream number (N=16 is used in this study), and the asymmetry factor, g, is defined as

$$g = \frac{1}{2}\int_0^{\pi} P(\theta)\cos\theta\sin\theta d\theta$$

$$= \frac{1}{2}\int_{-1}^{1} P(\mu)\mu d\mu\,, \tag{4.2}$$

where P(θ) is the phase function, and μ is equal to cosθ.

The H-G phase function can be specified by the asymmetry factors which can be extracted from the single scattering database (section 4.2.2). In this study, the mean values of extinction efficiency, absorption efficiency, and asymmetry factor are interpolated from the single scattering database, which are consequently used as the input variables in the DISORT code. Using the aforementioned input variables, the transmittance and reflectance of ice and water clouds are computed from the DISORT code. The azimuthally averaged reflected and transmitted radiances are given as follows:

$$I(0,\mu,\mu_0) = \frac{I_{inc}}{4\pi\mu} S(\tau,\mu,\mu_0)\,, \tag{4.3}$$

$$I(\tau,-\mu,\mu_0) = \frac{I_{inc}}{4\pi\mu} T(\tau,\mu,\mu_0)\,, \tag{4.4}$$

where μ_0 is the cosine of the incident angle (θ_0), μ is the cosine of the reflected or transmitted angle, τ is the optical thickness of the cloud layer, I_{inc} is the incident radiance, and $S(\tau,\mu,\mu_0)$ and $T(\tau,\mu,\mu_0)$ are the azimuthally averaged bidirectional reflection and transmission functions of the cloud layer. The reflection and transmission

functions are regarded as symmetric in μ and μ_0 as required by the Helmholtz's principle of reciprocity (Chandrasekhar, 1960).

$$S(\tau, \mu, \mu_0) = S(\tau, \mu_0, \mu), \tag{4.5}$$

$$T(\tau, \mu, \mu_0) = T(\tau, \mu_0, \mu). \tag{4.6}$$

Since isotropic incident radiation is assumed in this study, the azimuthally averaged reflected and transmitted radiances are given as [*Stamnes and Swanson*, 1981]

$$I(0, \mu) = 2\pi \int_0^1 I(0, \mu, \mu_0) d\mu_0$$

$$= \frac{I_{inc}}{2\mu} \int_0^1 S(\tau, \mu, \mu_0) d\mu_0, \tag{4.7}$$

$$I(\tau, -\mu) = 2\pi \int_0^1 I(\tau, -\mu, \mu_0) d\mu_0$$

$$= \frac{I_{inc}}{2\mu} \int_0^1 T(\tau, \mu, \mu_0) d\mu_0. \tag{4.8}$$

The albedo and the transmissivity for the cloud layer (a plane parallel medium) are given, respectively, as,

$$a(\mu) = I(0, \mu) / I_{inc}$$

$$= \frac{1}{2\mu} \int_0^1 S(\tau, \mu, \mu_0) d\mu_0, \tag{4.9}$$

$$t(\mu) = I(\tau, -\mu) / I_{inc}$$

$$= \frac{1}{2\mu} \int_0^1 T(\tau, \mu, \mu_0) d\mu_0, \tag{4.10}$$

where t(μ) is the diffuse transmissivity. If the incident radiation is 1, the total transmissivity, $t_{tot}(\mu)$, is given as the sum of two parts, the directly and diffusely transmitted radiances, as follows:

$$t_{tot}(\mu) = \exp(-\tau/\mu) + I(\tau,-\mu). \tag{4.11}$$

In the DISORT [*Stanmns et al.* 2000], I(0, μ) and I(τ,- μ) are given as

$$I(0,\mu) = \sum_{j=1}^{N} [\hat{C}_{-j1} \frac{G_{-j1}(\mu)}{1-k_{j1}} \hat{E}_{-j1}(0,\mu) + \hat{C}_{j1} \frac{G_{j1}(\mu)}{1+k_{j1}} \hat{E}_{j1}(0,\mu)], \tag{4.12}$$

$$I(\tau,-\mu) = \sum_{j=1}^{N} [\hat{C}_{-j1} \frac{G_{-j1}(-\mu)}{1+k_{j1}} \hat{E}_{-j1}(\tau,-\mu) + \hat{C}_{j1} \frac{G_{j1}(-\mu)}{1-k_{j1}} \hat{E}_{j1}(\tau,-\mu)], \tag{4.13}$$

where 2N is the number of stream, k_{j1} (or k_{-j1}) and $G_{j1}(\pm\mu)$ (or $G_{-j1}(\pm\mu)$) are the eigenvalues and eigenvectors obtained as the homogeneous solution, $\hat{C}_{j1}$ (or $\hat{C}_{-j1}$) are the coefficients which are used in the DISORT instead of constants of integration through the scaling transformation [*Stamnes and Conklin*, 1984]. $\hat{E}$'s are given as follows:

$$\hat{E}_{-j1}(0,\mu) = \exp[-k_{j1}\tau] - \exp[-\frac{\tau}{\mu}], \tag{4.14}$$

$$\hat{E}_{j1}(0,\mu) = 1 - \exp[-k_{j1}\tau - \frac{\tau}{\mu}], \tag{4.15}$$

$$\hat{E}_{-j1}(\tau,-\mu) = 1 - \exp[-k_{j1}\tau - \frac{\tau}{\mu}], \tag{4.16}$$

$$\hat{E}_{j1}(\tau,-\mu) = \exp[-k_{j1}\tau] - \exp[-\frac{\tau}{\mu}]. \tag{4.17}$$

The present lookup libraries comprise the transmittance (total: sum of direct and diffuse) and reflectance of ice and water clouds as functions of cloud visible optical thickness ranging from 0.04 to 50 and effective particle size varying between 3 and 100 μm. Since the transmittance and reflectance have viewing zenith angle dependence, nine viewing zenith angles are also considered from 0° to 80°. In this study, the transmittance and reflectance are calculated at 30 optical thicknesses, 30 effective particle sizes, 9 viewing zenith angles, and 1010 wavenumbers between 649 and 2667 cm^{-1}. Once the lookup libraries are prepared, the transmittance and reflectance of clouds can be derived for any cloud optical thickness, effective particle size, viewing zenith angle, and wavenumber which are located in the ranges available.

Figure 4.2 shows the transmittance and reflectance of ice and water clouds at three wavenumbers, 799, 901, and 1125 cm^{-1}. The transmittance converges to 0.6 as the effective size of the particle increases for both ice and water clouds. The reflectance shows some oscillations for ice cloud and becomes smaller with the increase of the effective size for water clouds. The values of the reflectance are one order smaller than the transmittance for both ice and water clouds.

4.2.4 One-layer FIRTM

In FIRTM, the gaseous absorption in the atmosphere is computed from a fast clear-sky radiance model developed by *Strow et al.* [2003a]. In this dissertation, only one-layered clouds are considered. FIRTM for this specified case is refered to as one-layer FIRTM. The effect of clouds on the IR radiative transfer is accounted for on the

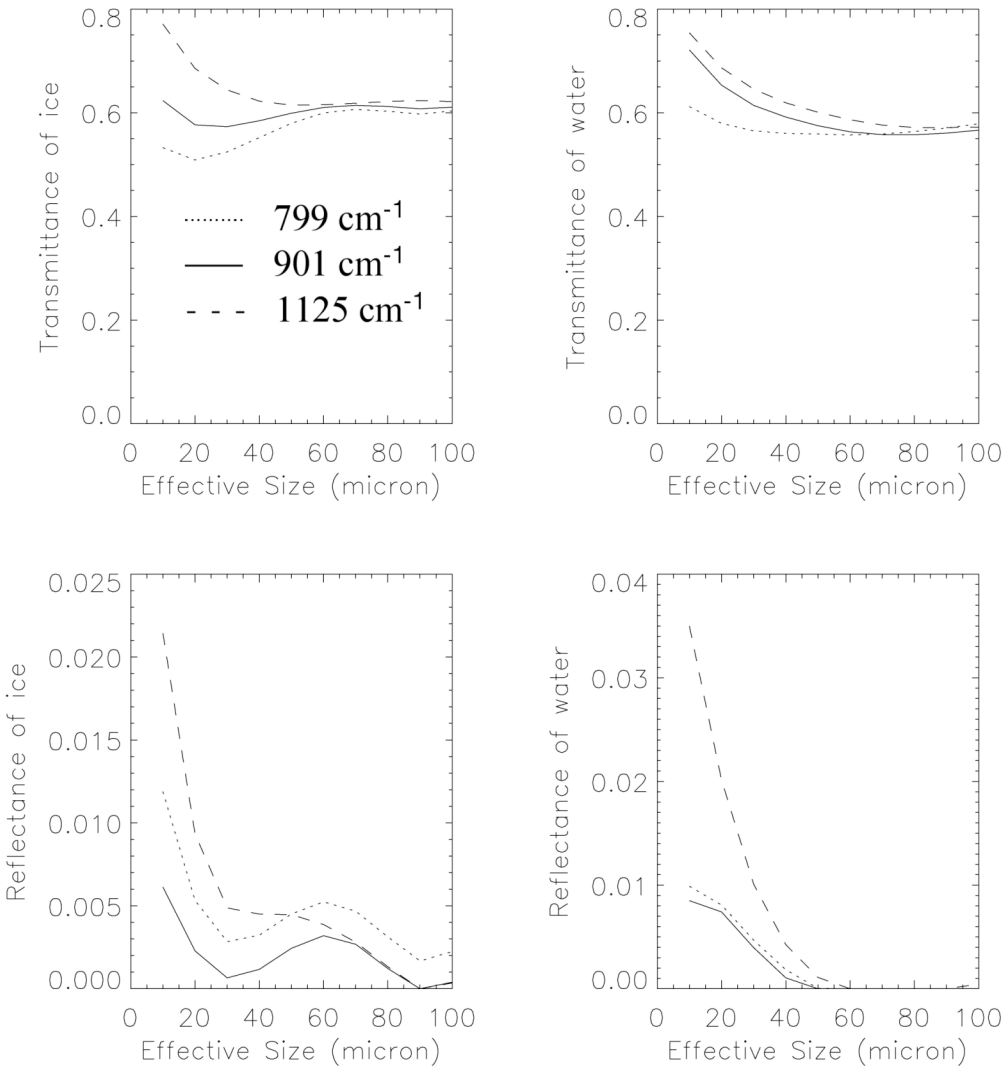

Figure 4.2 The transmittance and reflectance of ice and water clouds.

basis of pre-computed lookup libraries of cloud reflectance and transmittance, which are described in section 4.2.3.

For upward radiance the radiative transfer equation is written as follows (Liou 2002):

$$\mu \frac{dI}{d\tau} = I - B \qquad (0 < \mu <= 1), \tag{4.18}$$

where μ ($\cos\theta$) is the cosine of the viewing zenith angle, τ is the optical thickness, I is the upward radiance, and B is the source function. If we consider the transmissivity from TOA to an atmospheric layer, the transmissivity is given by the optical thickness as follows:

$$\Gamma = e^{-\frac{\tau}{\mu}}. \tag{4.19}$$

By the definition of the transmissivity in this study, the transmissivity at the top of atmosphere is 1. If Eq. (4.19) is applied to Eq. (4.18), we obtain

$$-\Gamma \frac{dI}{d\Gamma} = I - B. \tag{4.20}$$

Integration of Eq. (4.20) from Γ_0 to Γ_1 leads to the following result:

$$I(t_1) = I(t_s)\frac{\Gamma_0}{\Gamma_1} + \int_{\Gamma_0}^{\Gamma_1} \frac{B(t)}{\Gamma_1} d\Gamma, \tag{4.21}$$

where Γ_0 is the transmissivity from TOA to the surface, and Γ_1 is the transmissivity from TOA to a certain atmospheric layer. t is the temperature of an atmospheric layer, t_s is the surface temperature, and t_1 is the temperature of the atmospheric layer whose transmissivity is Γ_1.

To get the downward radiance, we need to replace μ with -μ. The basic equation is as follows:

$$-\mu \frac{dI}{d\tau} = I - B, \tag{4.22}$$

The transmissivity from an atmospheric layer to the surface is related to the optical thickness as follows:

$$\Gamma_d = \frac{\Gamma_0}{\Gamma} = e^{-\frac{\tau_0 - \tau}{\mu}}, \tag{4.23}$$

where τ_0 is the total optical thickness from the surface to TOA.

Applying Eq. (4.23) to Eq. (4.22), we obtain

$$-\Gamma_d \frac{dI}{d\Gamma_d} = I - B. \tag{4.24}$$

Integrating Eq. (4.24) from Γ_1 to Γ_0, we obtain

$$I(t_s) = I(t_1)\frac{\Gamma_0}{\Gamma_1} - \int_{\Gamma_1}^{\Gamma_0} B(t)\frac{\Gamma_0}{\Gamma^2} d\Gamma = I(t_1)\frac{\Gamma_0}{\Gamma_1} + \int_{\Gamma_1}^{\Gamma_0} B(t) d(\frac{\Gamma_0}{\Gamma}). \tag{4.25}$$

Using the basic form of the upward and downward radiances, one-layer FIRTM is essentially developed to compute the upward radiances and downward radiances. A cloud layer in one-layer FIRTM is assumed to be plane-parallel, isothermal, and homogeneous for a pixel (or FOV). The temperature of the cloud layer is assumed to be the same as that of the corresponding ambient atmospheric layer. The scattering effect of a cloud layer is included in the transmittance and reflectance derived from the lookup libraries (Section 4.2.3). Since surface emissivity is close to 1, only the first order reflection by the surface is considered in the model.

$$I_{TOA}(\mu) = I_1 + I_2 + I_3$$
$$= I_{u1} + (I_{u2}T(\mu)N + I_{u2}(1-N))\Gamma_1 + I_{d1}R(\mu)N + I_{cld}N +$$
$$(I_{d1}\Gamma_1/\Gamma_0((1-N)+T(\mu)N) + I_{d2} + I_{cld}N\Gamma_1/\Gamma_0)(1-\varepsilon)((1-N)+T(\mu)N)\Gamma_0$$

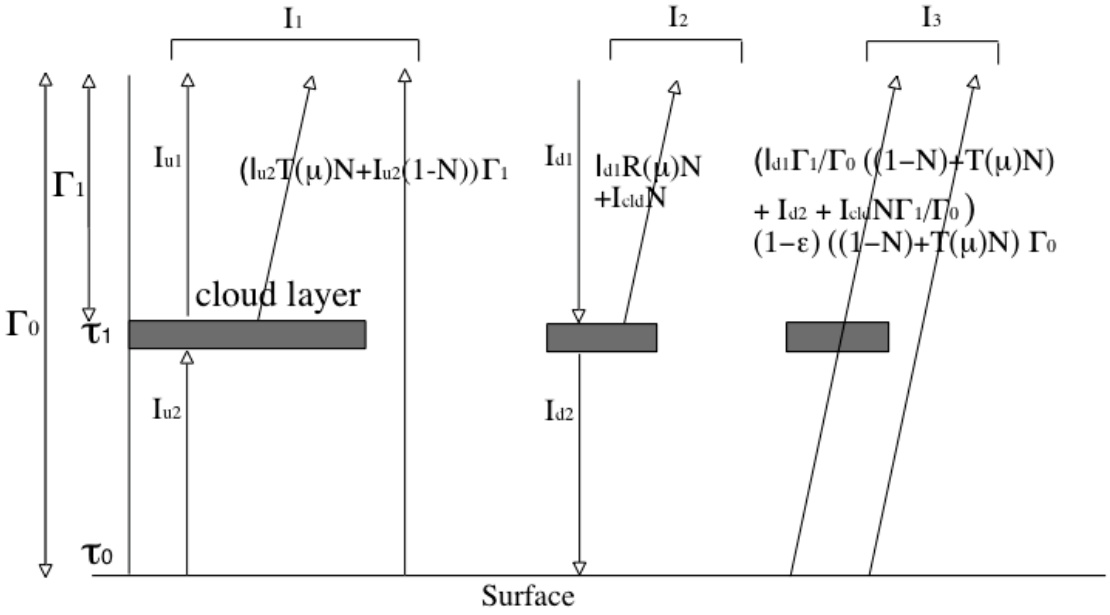

Figure 4.3 Radiative transfer in one layer FIRTM.

Figure 4.3 shows the radiance components in one-layer FIRTM. The vertical arrows show the radiances without reflection (non-scattering atmosphere) and the slanted arrows show the radiances affected by the cloud layer through reflection or transmission, depending on the viewing zenith angle. The energy conservation law is assumed, i.e., $R_\lambda + E_\lambda + T_\lambda = 1$ where R is cloud reflectivity, E is cloud emissivity, T is cloud transmissivity, and the subscript λ is wavelength.

The upward radiance observed at TOA in one-layer FIRTM is divided into three components of infrared radiances as indicated in Fig. 4.3.

1) Thermal radiance directly from the surface and atmospheric layers:

A part of the total radiance observed at TOA is the thermal radiance directly emitted from the surface and atmospheric layers, which can be divided into three terms as follows:

$$I_1 = I_{u1} + [I_{u2}\, T(\mu)\, N + I_{u2}\, (1\text{-}N)]\, \Gamma_1, \tag{4.26}$$

where N is cloud fraction, $T(\mu)$ is the transmittance of the cloud layer derived from the lookup libraries (Section 4.2.3) including direct and diffuse transmittance. Γ is the transmittance from TOA to a certain atmospheric layer and Γ_1 is the transmittance from TOA to the cloud top. I_{u1} and I_{u2} are the upwelling thermal radiances above and below the cloud layer, respectively, given by

$$I_{u1} = \int_{\Gamma_1}^{1} B(t)\, d\Gamma\,, \tag{4.27}$$

$$I_{u2} = B(t_s)\frac{\Gamma_0}{\Gamma_1} + \int_{\Gamma_0}^{\Gamma_1} \frac{B(t)}{\Gamma_1} d\Gamma , \quad (4.28)$$

where B(t) is the Planck function at temperature t, and t_s is the surface temperature. Γ_0 is the transmittance from TOA to the surface. At TOA the transmittance is 1. The term, I_{u1}, in Eq. (4.27) is the upwelling thermal radiance from the atmospheric layers above the cloud top. I_{u2} in Eq. (4.28) comprises the upwelling radiance from the surface and the atmospheric layers below the cloud layer. Since cloud fraction is considered for an FOV in one-layer FIRTM, a part of the FOV may be clear, and the rest may be cloudy. In this situation, the upwelling (or downwelling) radiance can pass through the cloud layer or pass through only the clear sky. The last two terms among three terms in the right hand side of Eq. (4.26) indicate the upwelling radiance passing through the cloud layer and the other passing through only the clear sky in an FOV. I_{u1} is the only term which is not viewing zenith angle dependent among the radiance elements considered in this model. Thermal radiance directly from the surface and atmospheric layers contributes most of the total radiance observed at TOA.

2) Reflected thermal radiance by the cloud layer and thermal emission from the cloud:

The second part of the total radiance observed at TOA is composed of the downward radiance from the atmospheric layers above the cloud top reflected by the cloud [I_{d1} R(μ) N Γ_1] and thermal emission (I_{cld} N Γ_1) from the cloud itself.

$$I_2 = [I_{d1} R(\mu) N + I_{cld} N] \Gamma_1, \quad (4.29)$$

where R(μ) is the reflectance of the cloud, and I_{cld} is the thermal radiance emitted from the cloud given by

$$I_{cld} = E(\mu)\, B(t_{cld})$$

$$= [1-R(\mu)-T(\mu)]\, B(t_{cld}), \tag{4.30}$$

where $E(\mu)$ is the emissivity of the cloud layer derived from $[1-R(\mu)-T(\mu)]$, t_{cld} is the temperature of the cloud layer, and I_{d1} is downwelling thermal radiance from the atmospheric layers above the cloud top given by

$$I_{d1} = \int_{1}^{\Gamma_1} B(t)\, d\left(\frac{\Gamma_1}{\Gamma}\right). \tag{4.31}$$

3) Thermal radiance reflected by the surface:

The third part of the total radiance observed at TOA is composed of the thermal radiance reflected by the surface, given by

$$I_3 = \{I_{d1}\, \Gamma_1/\, \Gamma_0\, [(1-N)+T(\mu)\, N] + I_{d2} + I_{cld}\, N\, \Gamma_1/\Gamma_0\}$$

$$\cdot(1-\varepsilon)\, [(1-N)+T(\mu)\, N]\, \Gamma_0, \tag{4.32}$$

where ε is surface emissivity. If the downwelling radiance is multiplied by $(1-\varepsilon)$, it represents the reflected radiance by the surface. I_{d2} is the downwelling radiance from the atmospheric layers below the cloud layer which can be as follows:

$$I_{d2} = \int_{\Gamma_1}^{\Gamma_0} B(t)\, d\left(\frac{\Gamma_0}{\Gamma}\right). \tag{4.33}$$

I_3 comprises four terms before the reflection by the surface, e.g., the downwelling thermal radiance to the surface from the atmospheric layers above the cloud layer which transmits the cloud layer, the downwelling thermal radiance to the surface from the atmospheric layers above the cloud layer, which transmits only the clear sky, the downwelling thermal radiance from the atmospheric layers below the cloud layer, and

thermal emission from the cloud layer to the surface. After the reflection by the surface, this part is divided into two terms, i.e., the radiances passing through the cloud layer and through only the clear sky in an FOV.

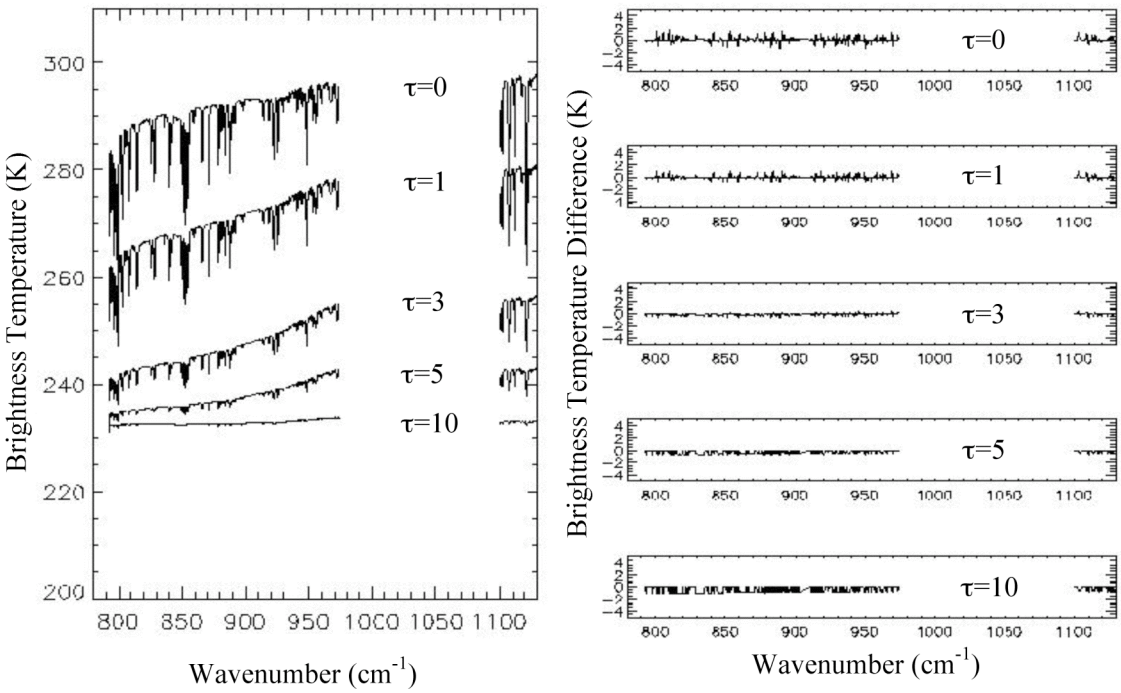

Figure 4.4 Brightness temperature from one layer FIRTM simulations for several cloud optical thicknesses; τ=0, 1, 3, 5, and 10 on the left panel. The brightness temperature difference between one layer FIRTM and the DISORT simulations for several cloud optical thickness. Vertical profiles of temperature and water vapor from an AIRS FOV are used. Cloud top temperature is assumed as 220 K, and the surface temperature is 307 K.

One-layer FIRTM must be validated for application to the retrieval of cloud properties. The results from the DISORT code are compared with the results from one-layer FIRTM using the same configuration. Figure 4.4 shows the difference between the one layer cloud model and DISORT for clear sky and cloudy cases for an AIRS pixel. The differences between one-layer FIRTM and DISORT solutions are usually smaller than 1 K in absolute value for clear sky or cloudy simulation.

4.2.5 Determination of cloud properties

To retrieve cloud properties, one needs to determine whether a pixel is cloudy or clear. The clearest window band around 960 cm^{-1} is chosen carefully, and the observed brightness temperature at this channel is compared with the calculated brightness temperature for given vertical profiles of temperature and water vapor, and some other gases. If the calculated brightness temperature is higher than the brightness temperature at the window channel, the pixel is declared as cloudy; otherwise, it is considered as a clear sky pixel.

The CO_2 slicing method is applied to each AIRS level-1b pixel within an AIRS granule to retrieve cloud top pressure and effective cloud amount. The theoretical basis of the CO_2 slicing method is in the following discussions.

The radiance from a cloudy field of view can be written as

$$R(\nu) = (1 - N)\cdot R_{clr}(\nu) + N\cdot R_{cld}(\nu)\,, \tag{4.34}$$

where the radiance from a cloudy region is given by

$$R_{cld}(\nu) = (1 - E)\cdot R_{clr}(\nu) + E\cdot R_{bcd}(\nu)\,. \tag{4.35}$$

By applying Eq. (4.35) to Eq. (4.34), another form of radiance is given as

$$R(\nu) = (1 - NE)\cdot R_{clr}(\nu) + NE\cdot R_{bcd}(\nu, P_c), \tag{4.36}$$

where $R(\nu)$ is the radiance observed from a field of view, $R_{clr}(\nu)$ is the corresponding clear sky radiance, $R_{bcd}(\nu, P_c)$ is the corresponding radiance if the field of view were completely covered with an opaque cloud at pressure level P_c and calculated from a temperature and moisture profile using the AIRS fast model, N is the cloud fraction of the field of view, and E is the cloud emissivity. $R_{bcd}(\nu, P_c)$ and $R_{clr}(\nu)$ are given by

$$R_{bcd}(\nu, P_c) = R_{clr} - \int_{P_c}^{P_s} \tau(\nu, p) \frac{dB[\nu, T(p)]}{dp} dp, \tag{4.37}$$

$$R_{clr}(\nu) = B(P_s)e^{-\tau_0} - \int_{P_c}^{P_s} \tau(\nu, p) \frac{dB[\nu, T(p)]}{dp} dp, \tag{4.38}$$

where P_s is the surface pressure, P_c is the cloud top pressure, $\tau(\nu, p)$ is the fractional transmittance of radiation at frequency ν emitted from the atmospheric pressure level (p) arriving at TOA (p=0), and $B[\nu, T(p)]$ is the Planck radiance at frequency ν for temperature T(p). The second term on the right-hand side in Eq. (4.37) represents the decrease in radiation from clear conditions introduced by the opaque cloud. The clear sky radiance is calculated using the atmospheric profiles given by AIRS products without any cloud layers. By applying Eqs. (4.37) and (4.38) to Eq. (4.36), the ratio between two channels is given as

$$\frac{R(\nu_1) - R_{clr}(\nu_1)}{R(\nu_2) - R_{clr}(\nu_2)} = \frac{NE_1 \int_{P_c}^{P_s} \tau(\nu_1, p) \frac{dB[\nu_1, T(p)]}{dp} dp}{NE_2 \int_{P_c}^{P_s} \tau(\nu_2, p) \frac{dB[\nu_2, T(p)]}{dp} dp}. \tag{4.39}$$

The optimum cloud top pressure is determined when the sum of the difference between the right- and left-hand sides for the whole channel considered in this study is its minimum. Usually, in the CO_2 slicing method, several pairs of channels near 15 μm are selected to be used in Eq. (4.39), and the number of selected channels depends on the spectral resolution around 15 μm. Twenty-one pairs of channels are used in this study. The differences for the twenty-one pairs of channels are summed up and compared for each P_c to obtain the optimum cloud top pressure. There are two basic assumptions inherent in this method, that is, the cloud has infinitesimal physical thickness, and furthermore, the cloud emittances are the same for the two spectral channels.

Once the cloud top pressure is determined using Eq. (4.39), effective cloud amount is determined as follows:

$$NE = \frac{R(w) - R_{clr}(w)}{B[w, T(P_c)] - R_{clr}(w)}, \tag{4.40}$$

where N is the fractional cloud cover within the FOV, E is the cloud emissivity, NE is the effective cloud amount, w represents the window channel frequency, and $B[w, T(P_c)]$ is the opaque cloud radiance. Effective emissivity (or effective cloud amount) cannot be calculated without an estimate of the window channel clear sky radiance. In this dissertation, 960 cm^{-1} is used as a window channel to compute effective cloud amount. For each cloudy pixel, we have effective cloud amount and corresponding emissivity for the window channel from the lookup libraries so that cloud fraction is calculated for the pixel.

For the cloud phase determination, the temperature of the cloud layer is used. The temperature of the cloud layer is assumed to be the temperature of the corresponding atmospheric layer. When the temperature of the cloud layer is below 258 K, the cloud phase is assumed to be ice [*Rogers and Yau*, 1994], and when the temperature of the cloud layer is above 273 K, it is assumed to be water. If the cloud temperature is between 258 K and 273 K, the cloud phase is assumed to be unknown, which is assumed to be water to retrieve the cloud optical thickness and effective particle size.

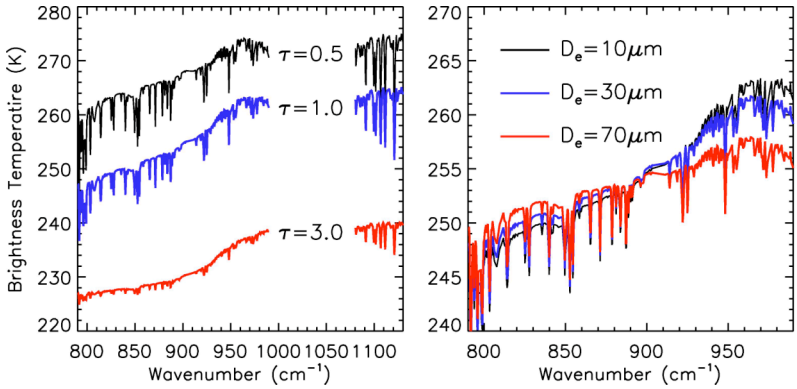

Figure 4.5 Dependence of brightness temperature on ice cloud. Optical thickness (τ) with De = 10 μm (left) and effective particle size (De) with τ=1 (right) using atmospheric environment of a pixel from AIRS granule.

Once cloud top pressure, effective cloud amount, and cloud phase are determined, cloud optical thickness and effective particle size can be retrieved. *Huang et al*. [2004] showed that for ice clouds the slope of the IR brightness temperature spectrum between 760~990 cm^{-1} is sensitive to the effective particle size, whereas a strong sensitivity of the IR brightness temperature to cloud optical thickness is noted within the 1060~1130 cm^{-1} region (Fig. 4.5). For the same region the optical thickness of water clouds has less sensitivity than that of ice clouds (not shown). Also, brightness temperatures in this spectral region are not sensitive to the particle size of water clouds.

Based on these spectral features, a technique illustrated by the flow chart in Fig. 4.6 is proposed for the simultaneous retrieval of the visible optical thickness and effective particle size from high spectral resolution infrared data for clouds. To determine τ and D_e, simulated annealing based on the simplex method [*Nelder and Mead*, 1965] is employed. The simplex method requires function evaluations and finds the minimum value through its own steps (reflection, expansion, and contraction). The simulation starts with arbitrary initial guess values of τ & D_e, and the sum of the brightness temperature difference squared, $(\Delta BT)^2$ between observation and simulation in the range of 760~990 & 1060~1130 cm^{-1} divided by the sum of squared error factors are checked. The weighted sum of brightness difference between the observation and the simulation is given as

$$\sum_{i=1}^{NCHAN} \frac{(BT_{OBS}(I) - BT_{sim}(I))^2}{NEDT(i)^2 + forward\_\mathrm{mod}el\_error(i)^2}, \qquad (4.41)$$

where NCHAN is the total number of channels available in the range considered in this study, and NEDT(i) (noise equivalent delta temperature) is the instrumental noise in the brightness temperature unit at the i^{th} channel. The forward model error includes the error of the radiative transfer calculation in the model and the RTA (Radiative Transfer Algorithm) fitting error for the fast transmittance regressions. NEDT given at 250 K is available as a text file (L2chan_prop.2003.11.19v6.8.1.txt) from the website http://daac.nasa.gsfc.gov/AIRS/documentation/v4_docs/. It is converted to NEDT at the observed brightness temperature using the following equation [*Sherlock et al.* 2003],

$$NEDT(i,T_B) = \frac{NEDT(i,250)\left.\frac{\partial B(i,T)}{\partial T}\right|_{T=250K}}{\left.\frac{\partial B(i,T)}{\partial T}\right|_{T=T_B}}, \qquad (4.42)$$

where B(i,T) is the Planck function at brightness temperature T at the i^{th} channel, and T_B is the observed brightness temperature at the i^{th} channel. The derivative, $\left.\frac{\partial B(i,T)}{\partial T}\right|_{T=T1}$ is calculated by the difference of Planck functions at brightness temperatures (T1-0.1) K and (T1+0.1) K. Figure 4.7 shows the NEDT given at 250 K for the infrared channels considered in this study. Most of NEDT at 250 K are below 0.5 K. *Strow et al.* [2003] showed the RTA fitting error is much less than 0.2 K for almost all the AIRS channels. *Li et al.* [2004] used a forward model error value of 0.5 K in their study. In this dissertation, a forward model error value of 0.5 K is also used. The iteration to find τ and D_e will be carried out until the weighted sum reaches its minimum.

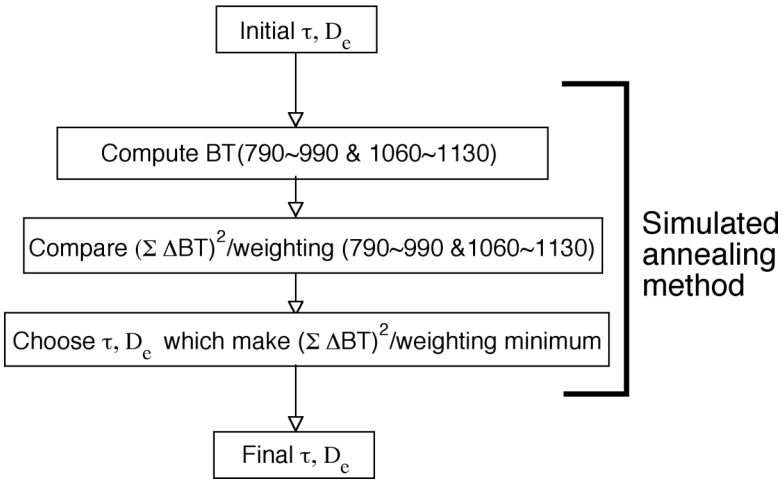

Figure 4.6 Flow chart for the retrieval of cloud optical thickness and effective particle size.

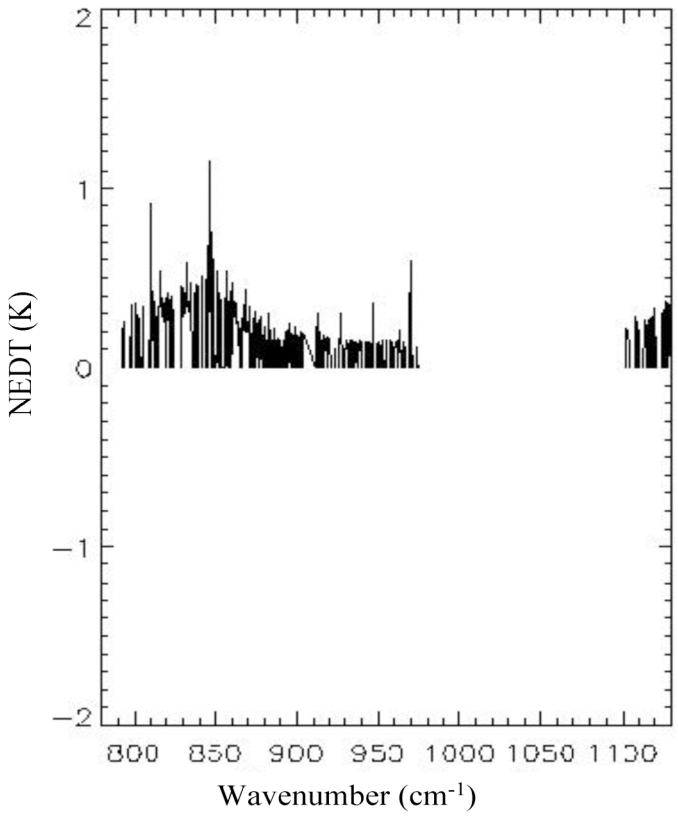

Figure 4.7 NEDT (K) at 250 K used in this study.

The AIRS L2 products provide quality control flags for retrieved geophysical quantities, and AIRS science team recommends using the retrieval results when quality control flags are equal to 0. However, all AIRS L2 products selected are used independently of quality control flags in this study. *Szczodrak et al*. [2005] reported that although the retrieval results are used independently of the quality flag values, the retrieved air temperature and humidity profiles from AIRS data showed similar quality compared to other methods, such as the European Center for Medium-Range Weather Forecasting (ECMWF) analysis and the Marine-Atmosphere Emitted Radiance Interferometer (M-AERI) retrieval.

4.2.6 The simulated annealing method

The simulated annealing process is employed to infer the appropriate values of cloud optical thickness and effective particle size, starting with the retrieved cloud top pressure, effective cloud amount, and cloud phase.

Simulated annealing includes the annealing process and the simplex method to find a function minimum in N-dimensional space. To accomplish the simulated annealing procedure, four elements are needed [*Press et al.*, 1992]. First, an objective function value for which we have to find the minimum is needed. One of the advantages of this method is that we only need to evaluate the function rather than its derivative. Second, when this procedure begins, the system status is needed, e.g., we select N+1 starting points of **X** and calculate the corresponding values of the function. Third, a control parameter is needed which is gradually reduced following an annealing schedule.

The last one is how the next points (**X+ΔX**) are selected from **X**. The simplex method is used to determine the next points with three operations, such as reflection, contraction and expansion [*Nelder and Mead*, 1965].

In this study, the simulated annealing method is applied beginning with arbitrary values of cloud optical thickness and effective particle size to make the problem less dependent on initial guess values using an iterative method. A 2-dimensional problem (N=2) is considered in which appropriate cloud optical thickness and effective particle size should be found to fit the observed brightness temperature for a cloudy AIRS pixel.

The simulated annealing method has several parameters which should be pre-determined. The fractional convergence tolerance (ftol) is one of those parameters. If the absolute difference between the local maximum and minimum function values multiplied by 2 and divided by the sum of absolute values of local maximum and minimum function value is smaller than ftol, then the subroutine returns N+1 points of X and the corresponding function values. A moderate tolerance (ftol = 10^{-4}) is used. The control parameter is set to 1000, which is reduced by 15 % when the iteration restarts.

In this dissertation, cloud optical thicknesses ranging from 0.04 to 20 and effective particle sizes ranging from 3 to 100 μm are considered. To make sure that the variables are varying within the boundaries, the following equation is considered [*Maltenfort and Hamm*, 2004]:

$$P_i = b_i + a_i \cdot [1.0 - \exp(-2.5 \cdot y_i^2)], \tag{4.43}$$

where P_i is value of the i^{th} parameter (e.g., cloud optical thickness and effective particle size), b_i is the minimum of the parameter i, and a_i is the difference between the

maximum and minimum of the parameter i. This equation converts the problem in which P_i ranges between b_i (lower boundary) and a_i+b_i (upper boundary) into an unconstrained problem in which the variable (y_i) varies from $-\infty$ to ∞.

Figure 4.8 shows the given cloud optical thickness (or effective particle size) and inferred cloud optical thickness (or effective particle size) within the relative error of 60% through the simulated annealing method using hyperspectral infrared channel information. The accuracy of the cloud optical thickness and effective particle size depends on cloud top height and viewing zenith angle. The accuracy especially of the effective particle size depends strongly on the accuracy of retrieved cloud optical thickness. To define the accuracy of the cloud optical thickness and effective particle size, the relative error is given by

$$error(\%) = \frac{A_{given} - A_{searched}}{A_{searched}} \times 100 \tag{4.44}$$

where A is the cloud parameter, such as cloud optical thickness and effective particle size. The subscript "given" refers to the assumed cloud optical thickness or effective particle size, and "searched" refers to the values of cloud optical thickness or effective particle size which are finally decided through the simulated annealing method. Within a 60 % error range, the suggested method in this study shows applicability to high clouds (located above 440 hPa). The accuracy of the inferred cloud optical properties depends on viewing zenith angle. Cloud optical thickness and effective particle size are inferred within a 60 % error range with a viewing zenith angle less than 30° and 10°, respectively. For clouds located in the lower troposphere, cloud optical thickness and

effective particle size cannot be retrieved through the method in this study using infrared channels. Henceforth, cloud optical properties, such as cloud optical thickness and effective particle size, are analyzed for high clouds (pressure below 440 hPa) with a viewing zenith angle less than 30° for cloud optical thickness (10° for effective particle size).

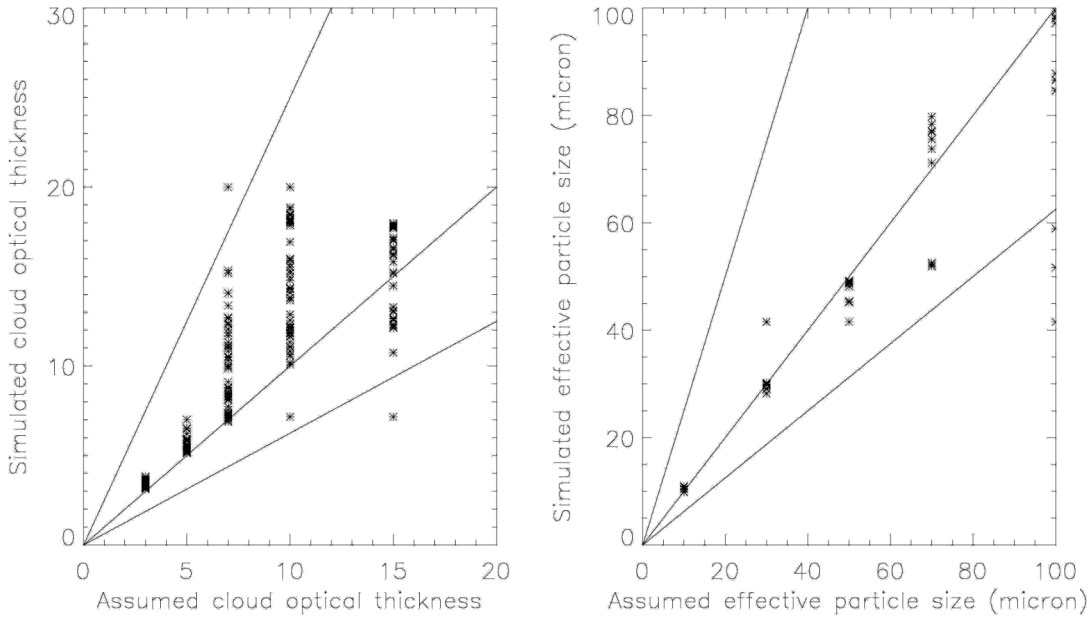

Figure 4.8 The accuracy to retrieve the cloud optical thickness (left panel) and effective particle size (right panel) for high clouds (above the 440 hPa level). Viewing zenith angle less than 30° (10°) for cloud optical thickness (effective particle size) is considered. Among the three solid lines in each panel, two solid lines on the top and bottom are 60% relative error lines, and the center line represents a line of y=x.

4.3. Results

4.3.1 Retrieval of cloud properties derived from AIRS observations and comparison with the corresponding MODIS products

The cloud properties retrieved from AIRS products are compared with the corresponding MODIS products. MODIS pixels with high spatial resolution are collocated to corresponding AIRS pixels, and consequently, cloud properties of the collocated MODIS pixels are averaged for comparison.

Figures 4.9 and 4.10 show cloud top pressure, effective cloud amount, cloud phase, cloud optical thickness, and effective particle size retrieved from AIRS and the corresponding MODIS products for the 4 AIRS granules at daytime (20041215_019, 20050315_025, 20050616_020, 20050915_017) among the 52 AIRS granules. The cloud top pressure and effective cloud amount derived from the AIRS and MODIS data agree well. The main differences between the AIRS and MODIS products come from the approach of determining an FOV as clear. In this study, an FOV is declared as clear when the observed brightness temperature at the 10.4 μm band is lower than the simulated brightness temperature. Meanwhile, visible, near infrared, and infrared channels are utilized to declare an FOV as clear or cloudy in MODIS. Thus, simply using the clearest window band radiance in AIRS causes some difference compared to MODIS data in determining the cloud status of an FOV. To determine thermodynamic cloud phase, the cloud top temperature is simply used (see section 4.2.5). If cloud top temperature is below 258 K (above 273 K), it is assumed as ice (water), whereas cloud phase is assumed as unknown if cloud layer temperature is between 258 K and 273 K.

For the retrieval of cloud optical thickness and effective particle size, the unknown cloud phase is assumed to be water. The cloud phase inferred from the cloud top temperature of AIRS is similar to MODIS cloud phase products except some edge areas between ice and water phase clouds. The retrieved cloud optical thickness of AIRS shows a pattern similar to the corresponding MODIS products. In Fig. 4.10, cloud optical thickness from AIRS is indicated if the cloud top pressure is below 440 hPa (i.e., high cloud) because of the restricted applicability of the suggested method in this study to infer cloud optical properties as shown in Fig. 4.8.

Figure 4.11 shows the correlation of cloud properties, such as cloud top pressure, effective cloud amount, cloud optical thickness, and effective particle size, retrieved from the AIRS and MODIS measurements. As evident from Fig. 4.9 cloud top pressure and effective cloud amount derived from AIRS data are well correlated to the corresponding MODIS products. Compared to MODIS products, AIRS cloud optical thickness is overestimated for small optical thickness (less than 5 in MODIS), and underestimated for large optical thickness (larger than 5 in MODIS). The accuracy of the effective particle size depends on the accuracy of the retrieval of cloud optical thickness in this method. The AIRS and MODIS retrievals do not show similar effective particle size of clouds.

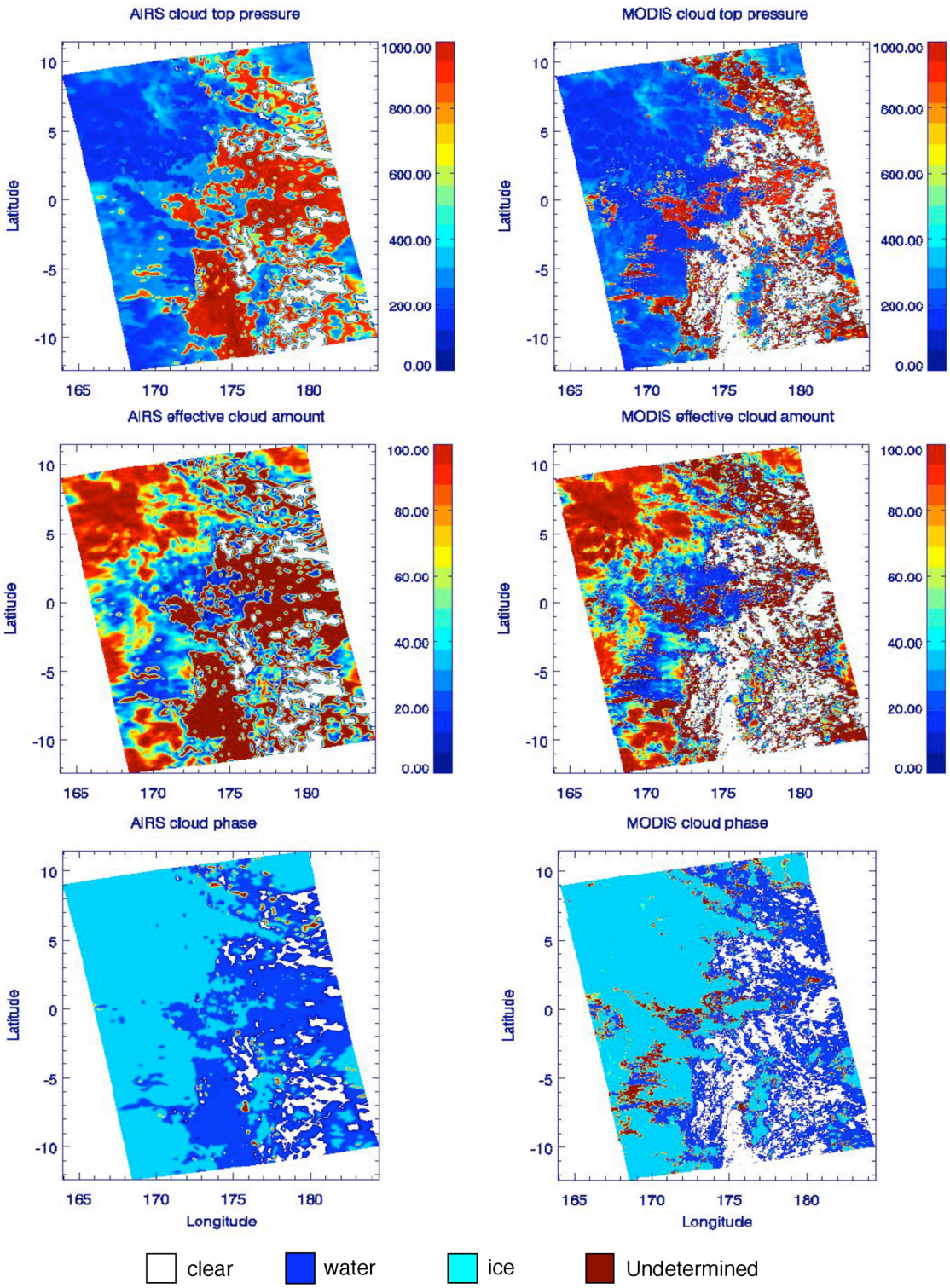

(a)

Figure 4.9 Retrieved cloud top pressure, effective cloud amount, and cloud phase from AIRS and corresponding MODIS products. (a) For a granule on 15 December 2004.

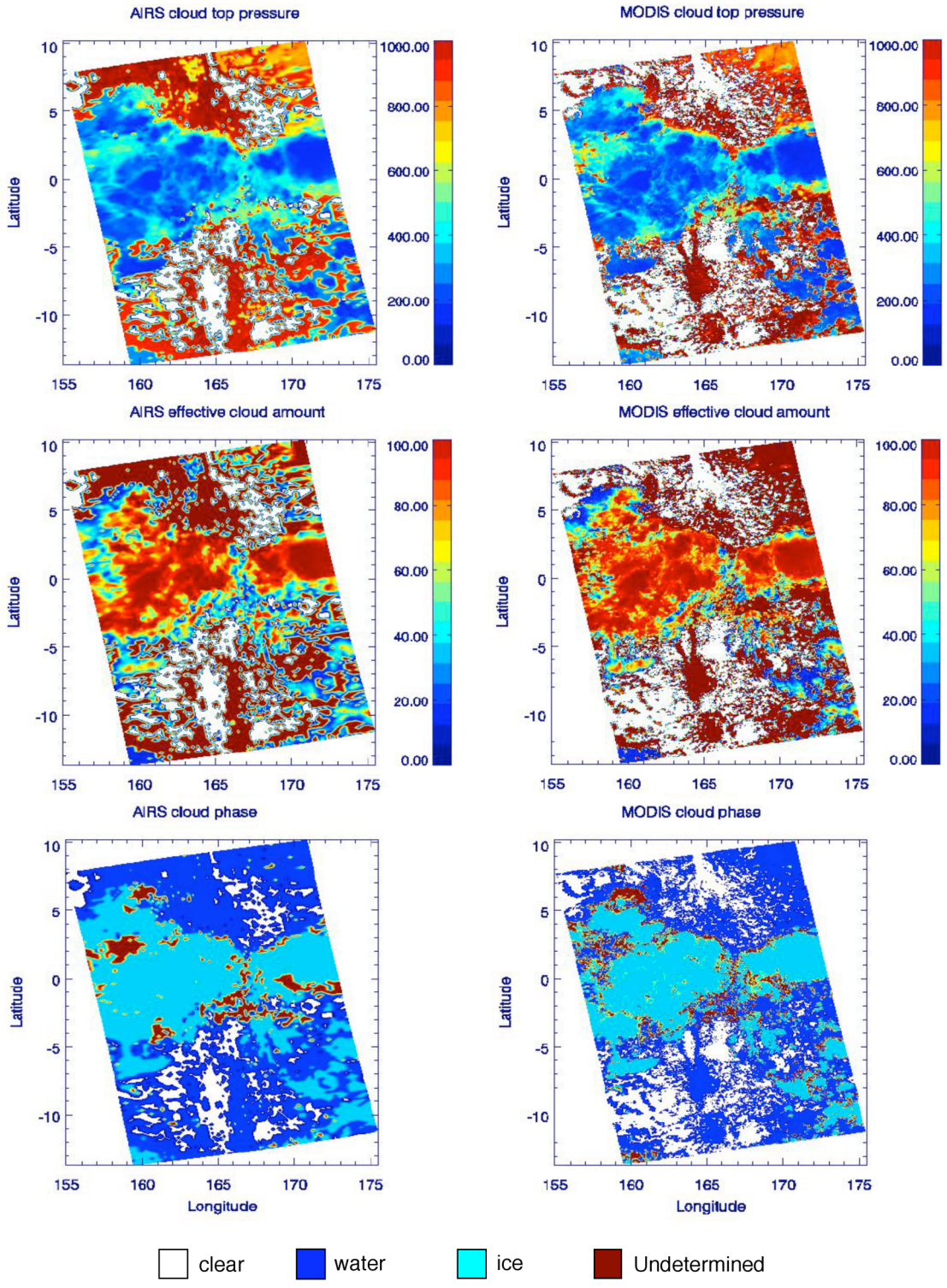

(b)
Figure 4.9 Continued. (b) For a daytime granule on 15 March 2005.

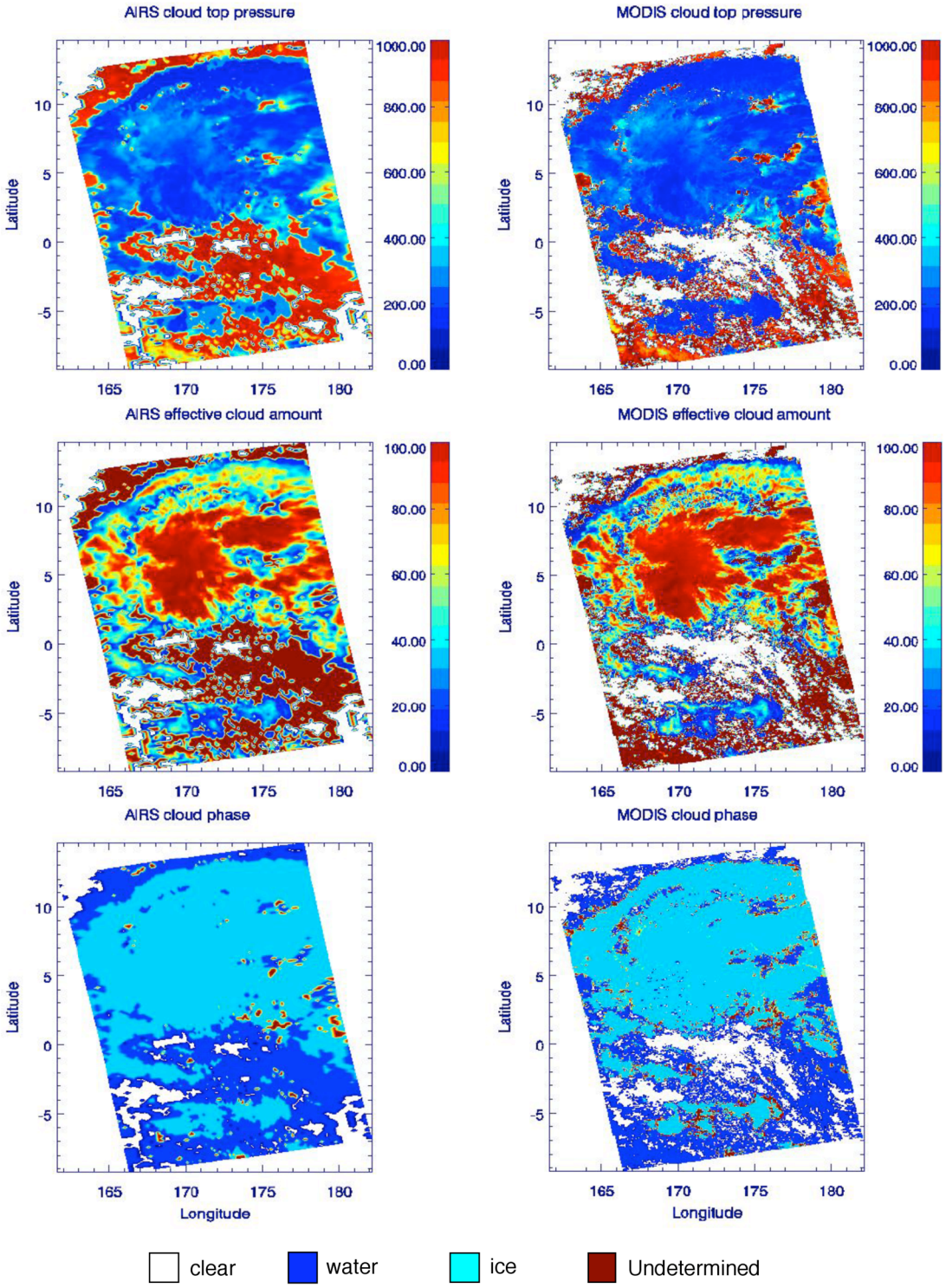

(c)

Figure 4.9 Continued. (c) For a daytime granule on 16 June 2005.

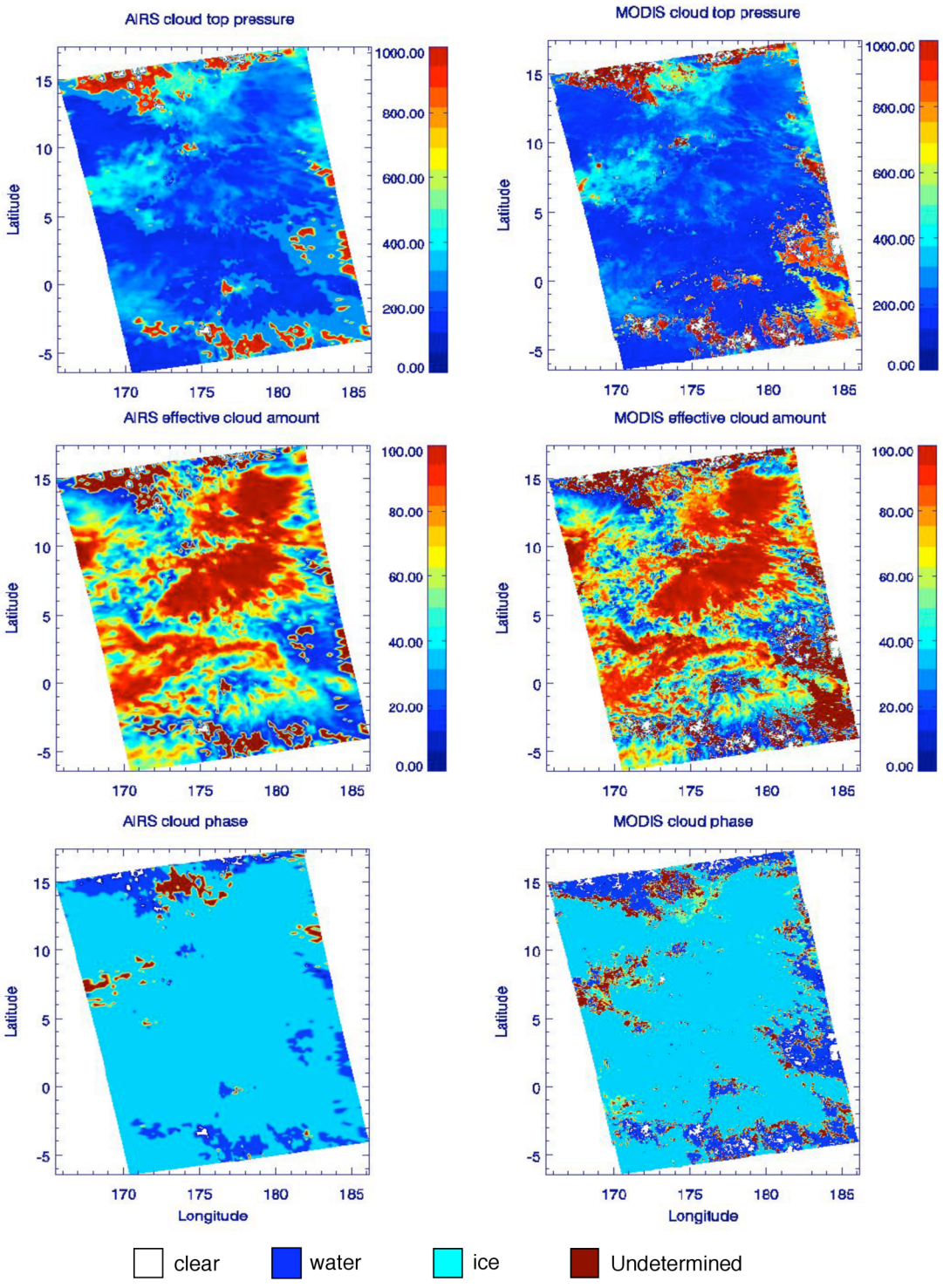

(d)

Figure 4.9 Continued. (d) For a daytime granule on 15 September 2005.

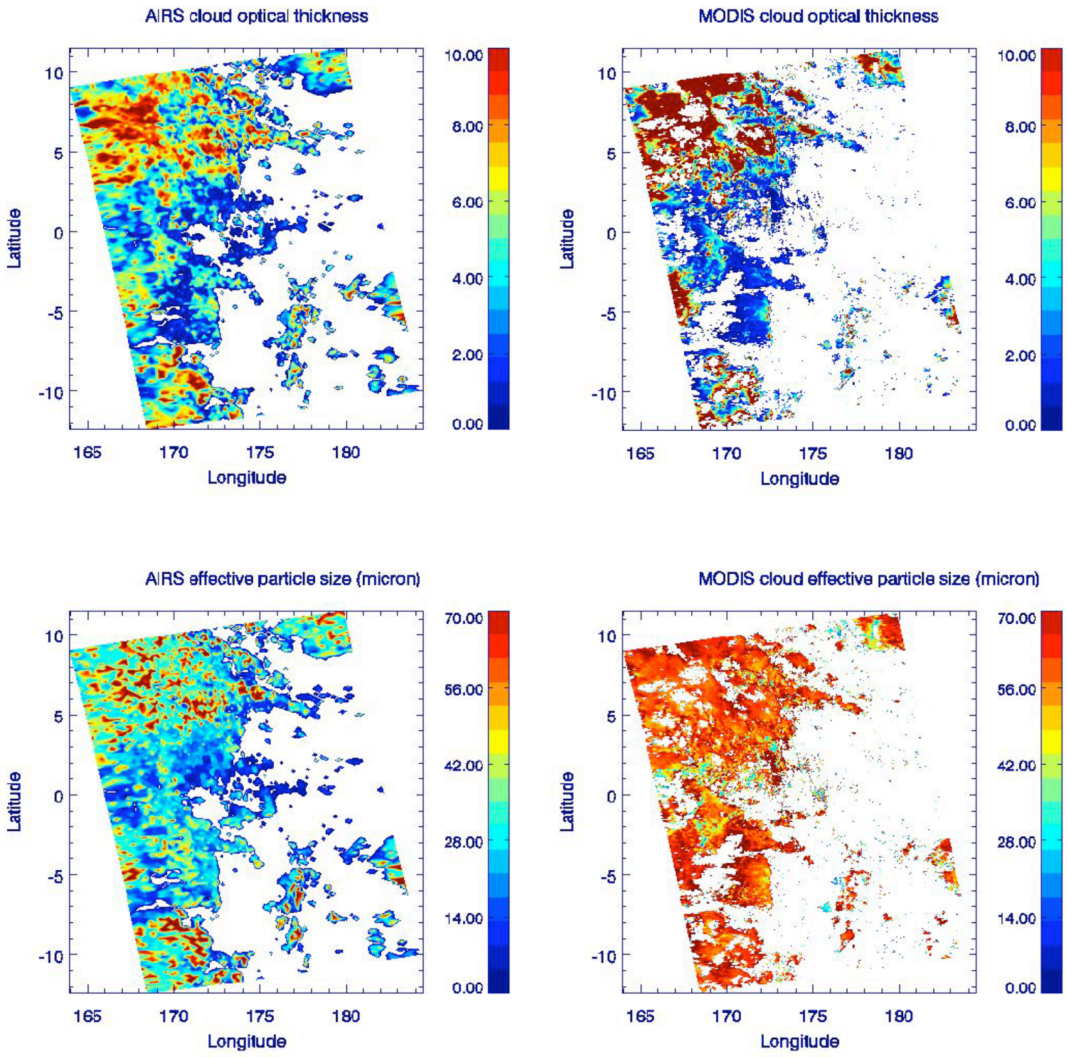

(a)

Figure 4.10 Retrieved cloud optical thickness and effective particle size from AIRS and corresponding MODIS products. (a) For a daytime granule on 15 December 2004. For AIRS cloud optical thickness and effective particle size, high cloud (above 440 hPa) is considered.

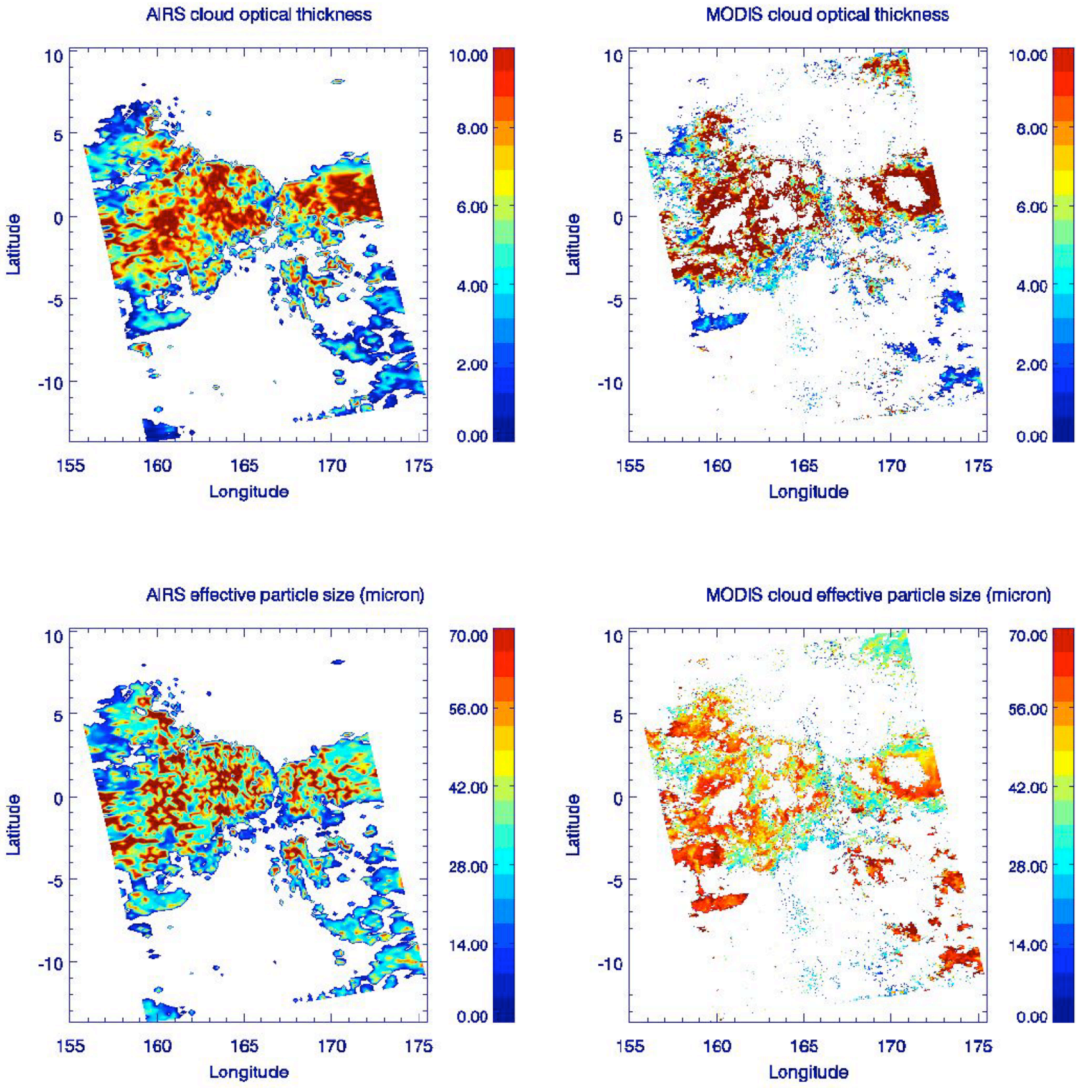

(b)

Figure 4.10 Continued. (b) For a daytime granule on 15 March 2005.

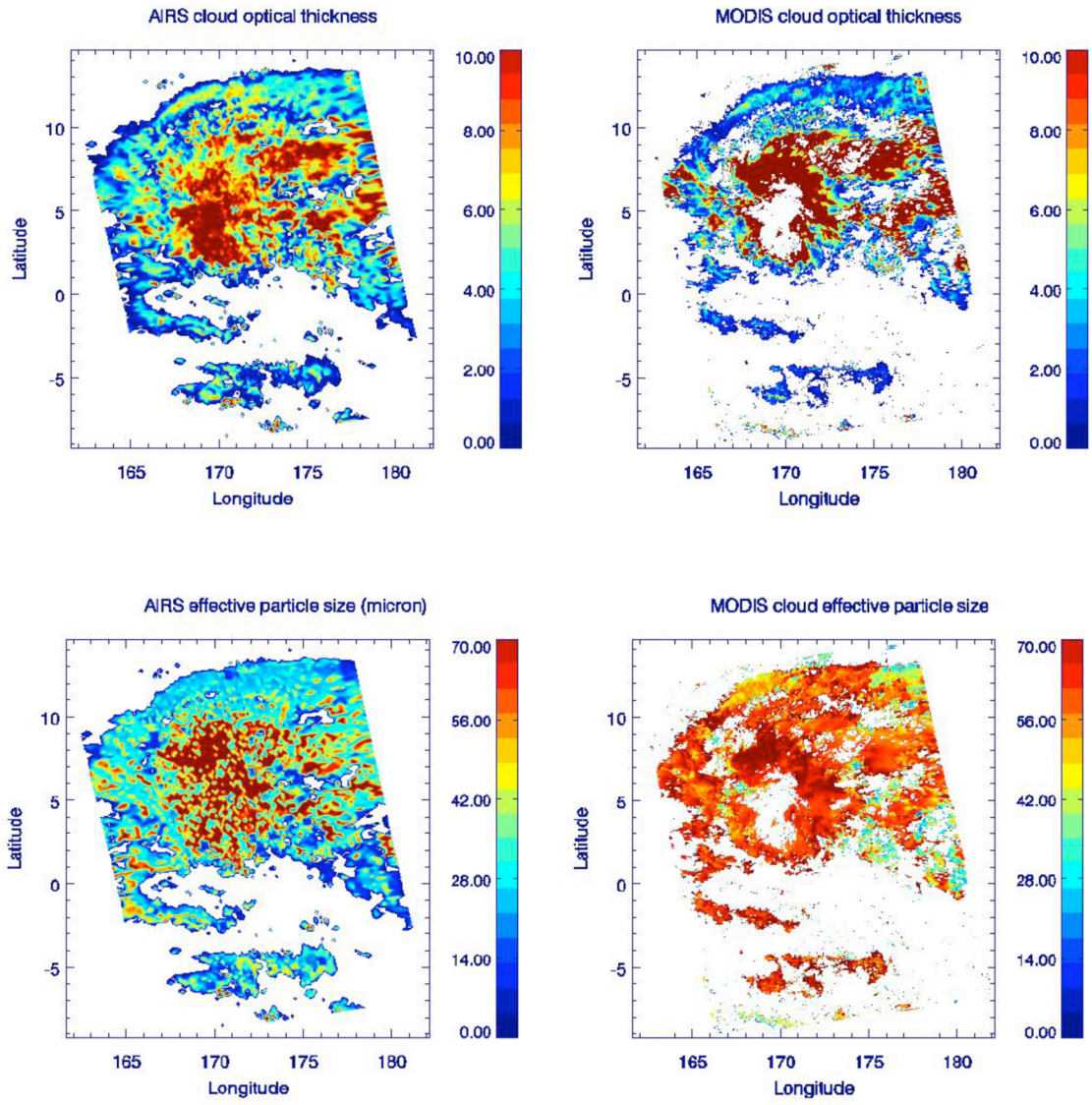

(c)

Figure 4.10 Continued. (c) For a daytime granule on 16 June 2005.

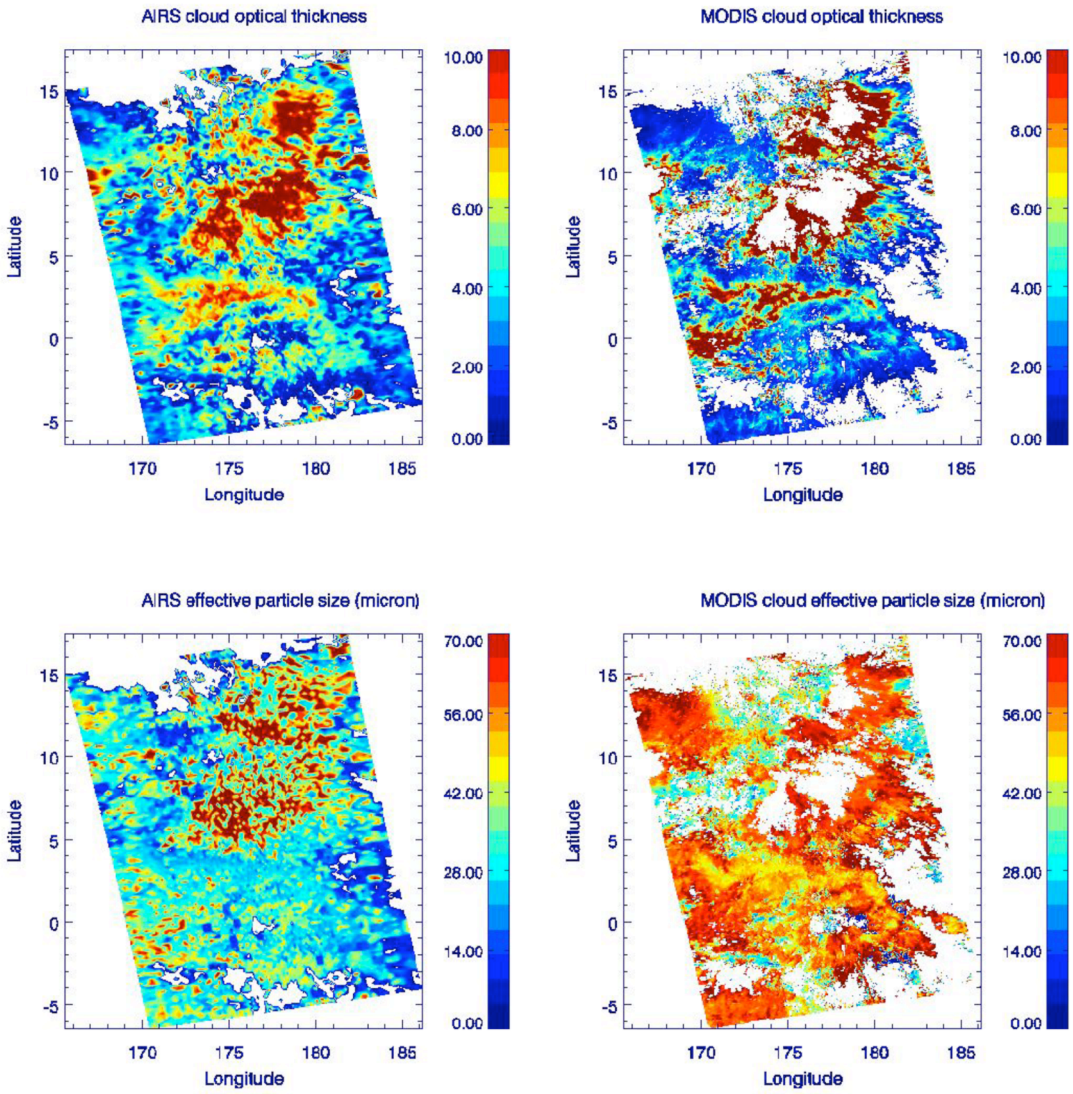

(d)

Figure 4.10 Continued. (d) For a daytime granule on 15 September 2005.

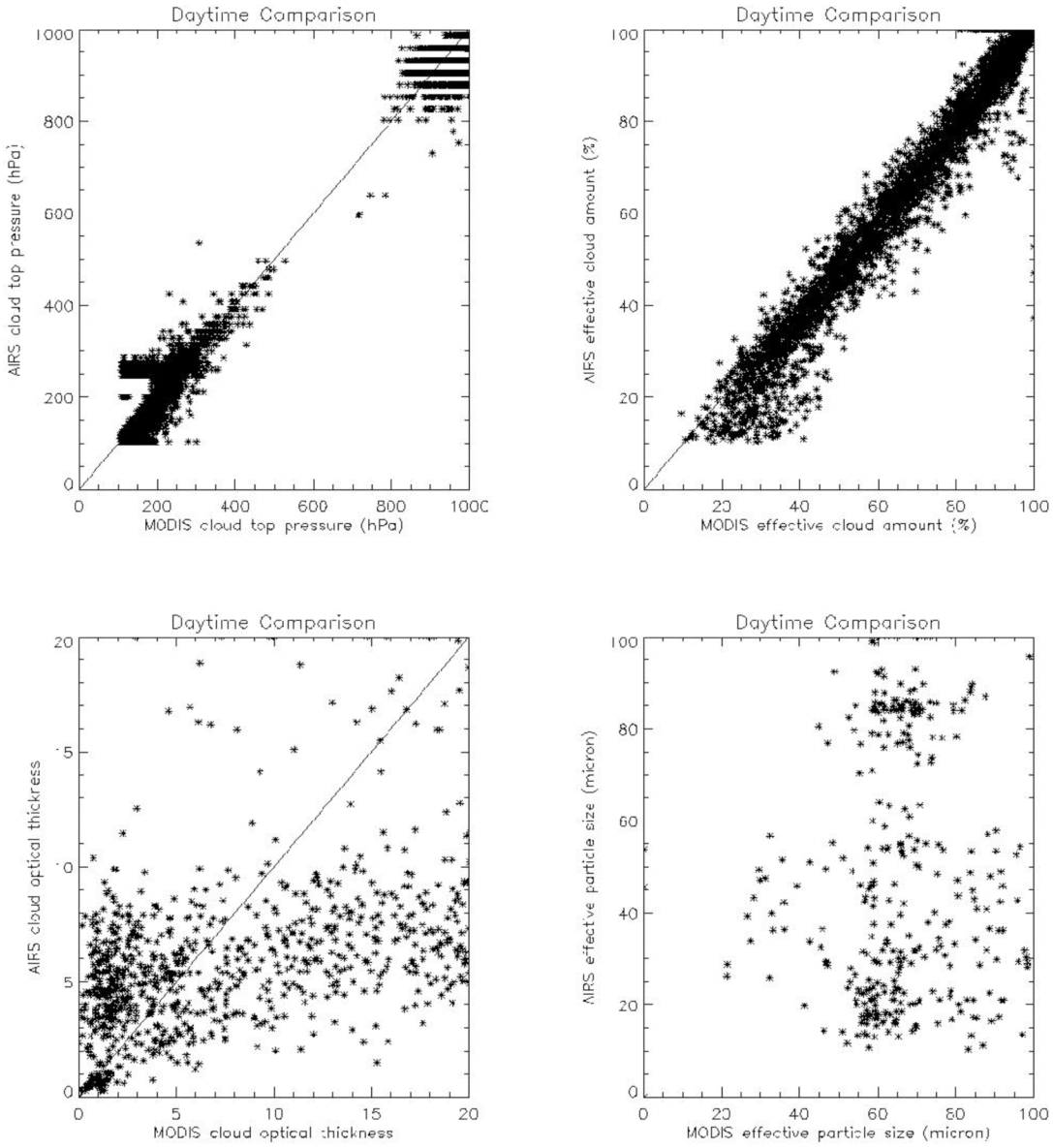

(a)

Figure 4.11 Scatter plots of cloud top pressure, effective cloud amount, cloud optical thickness and effective particle size between AIRS and MODIS. For cloud optical thickness, the viewing zenith angle below 30° is considered, and for effective particle size, the viewing zenith angle below 10° and cloud optical thickness less than 5 are considered. (a) For a daytime granule on 15 December 2004.

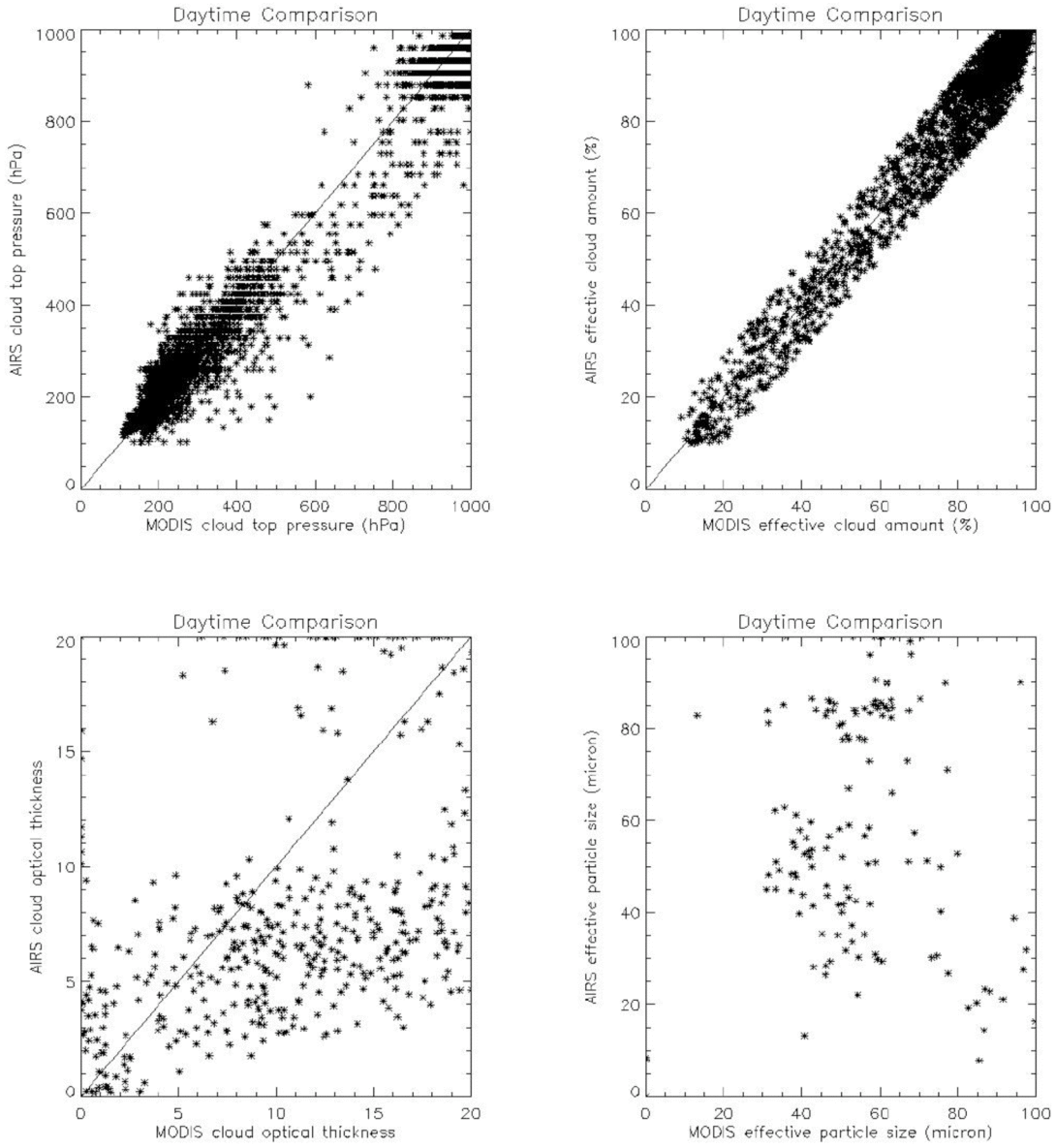

(b)

Figure 4.11 Continued. (b) For a daytime granule on 15 March 2005.

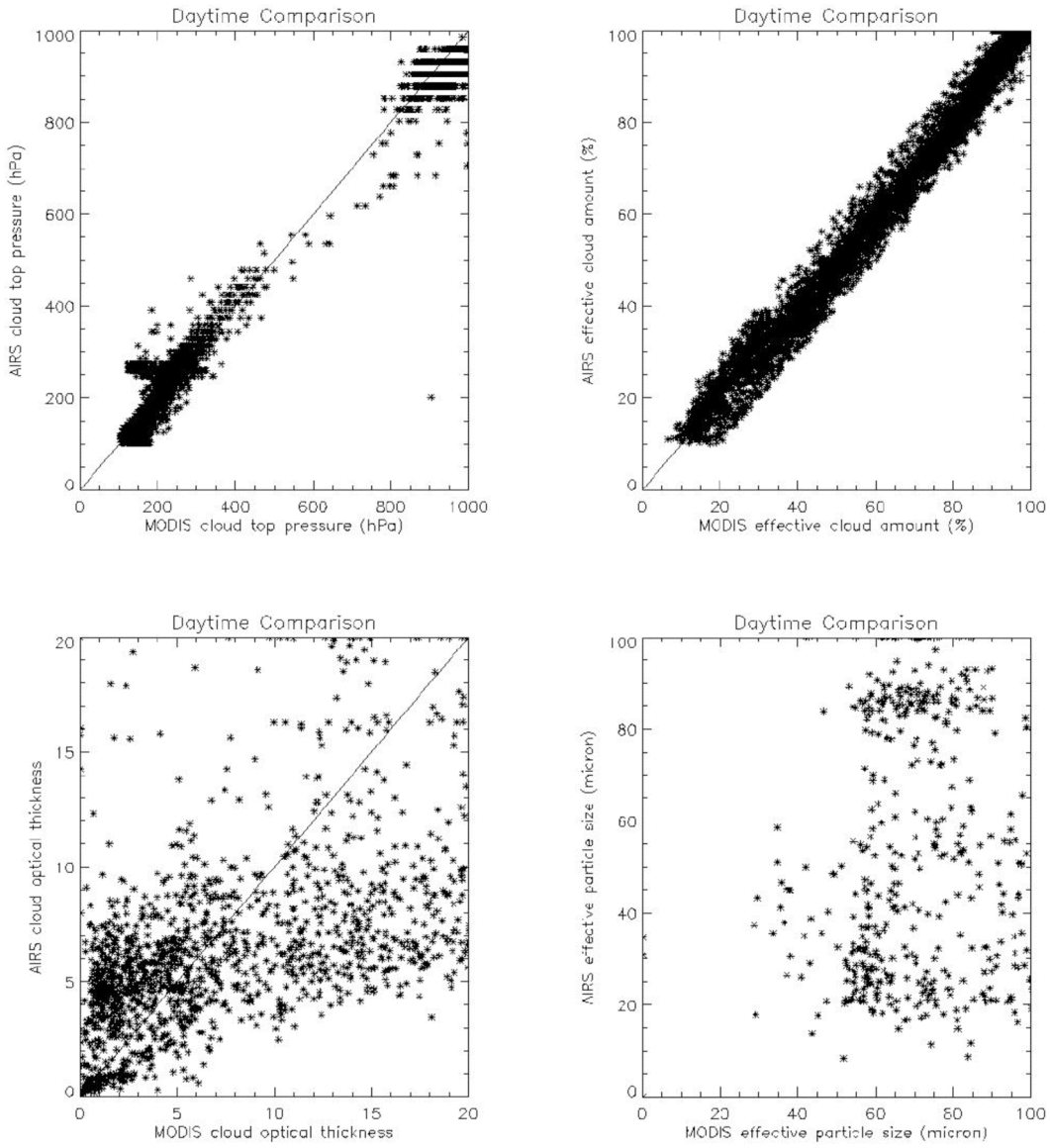

(c)

Figure 4.11 Continued. (c) For a daytime granule on 16 June 2005.

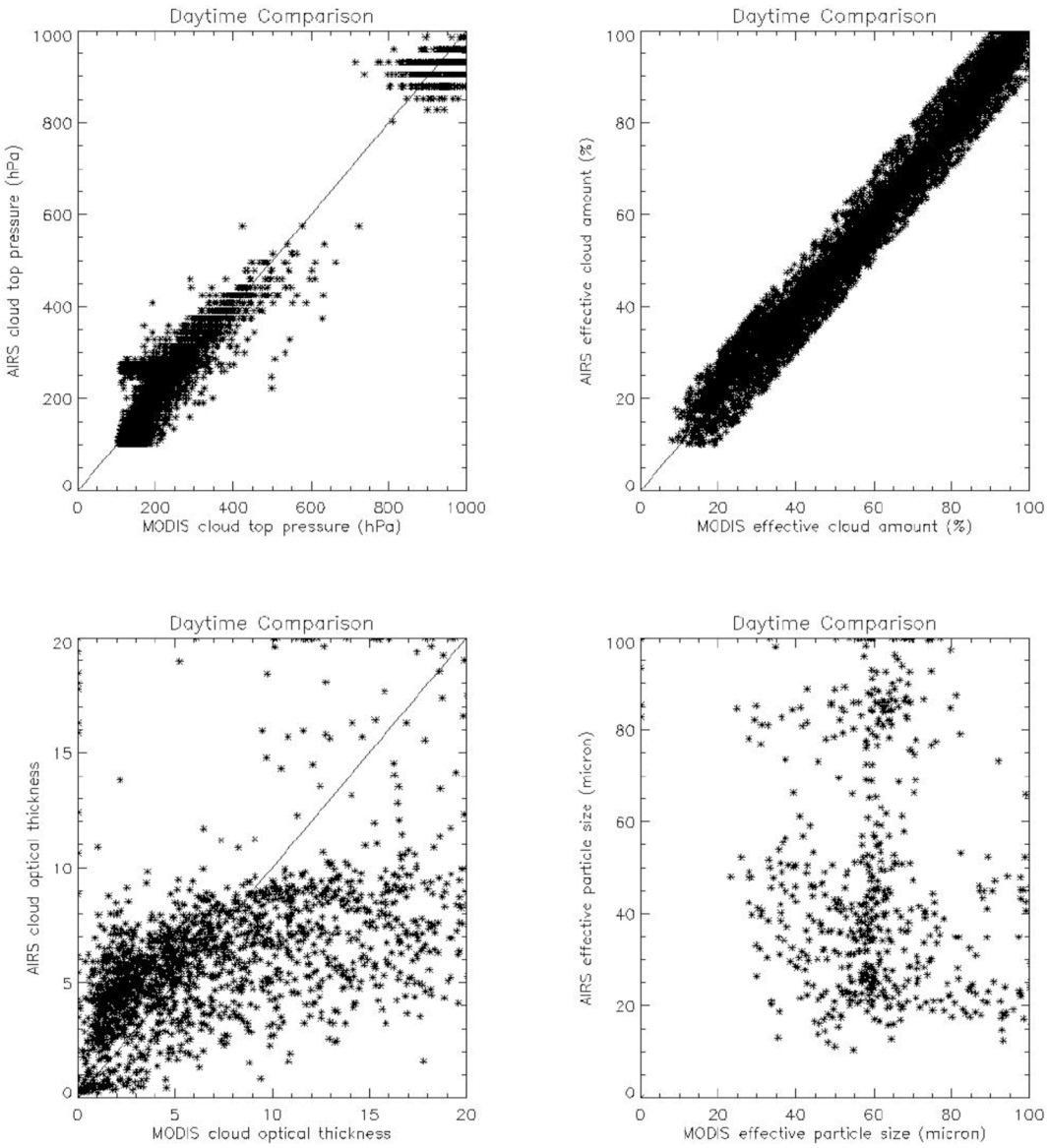

(d)

Figure 4.11 Continued. (d) For a daytime granule on 15 September 2005.

4.3.2 Diurnal and seasonal contrast of cloud properties

Cloud top pressure, effective cloud amount, thermodynamical phase, optical thickness, and effective particle size are retrieved from the AIRS data within the selected ocean area (E145° - E170°, S5° - N2°) to investigate the diurnal and seasonal contrasts of cloud properties.

Rossow and Schiffer [1999] suggested a new cloud type definition that is used in the ISCCP D-series datasets for daytime. Figure 4.12 shows the ISCCP cloud classification [same as Fig. 2 in *Rossow and Schiffer*, 1999], which uses cloud top pressure and cloud optical thickness to classify the cloud types. Since cloud optical thickness is available for nighttime in this study, their classification of clouds is applied for both daytime and nighttime. According to their classification, high clouds are defined when cloud top pressure is less than 440 hPa, middle clouds are defined when cloud top pressure is between 680 and 440 hPa, and low clouds are defined when cloud top pressure is larger than 680 hPa. According to cloud optical thickness, cloud types are further classified as cirrus, cirrostratus, and deep convection for high clouds; altocumulus, altostratus, and nimbostratus for middle clouds; and cumulus, stratocumulus, and stratus for low clouds. In this study, there is a clear distinction between thin clouds (e.g., cirrus, altocumulus, and cumulus) and thick clouds (e.g., cirrostratus, altostratus, stratocumulus, deep convection, nimbostratus, and stratus). However, deep convection, nimbostratus, and stratus are not distinguished from cirrostratus, altostratus, and stratocumulus because of the limitation of detecting the optical thickness in this study (see Fig. 4.8).

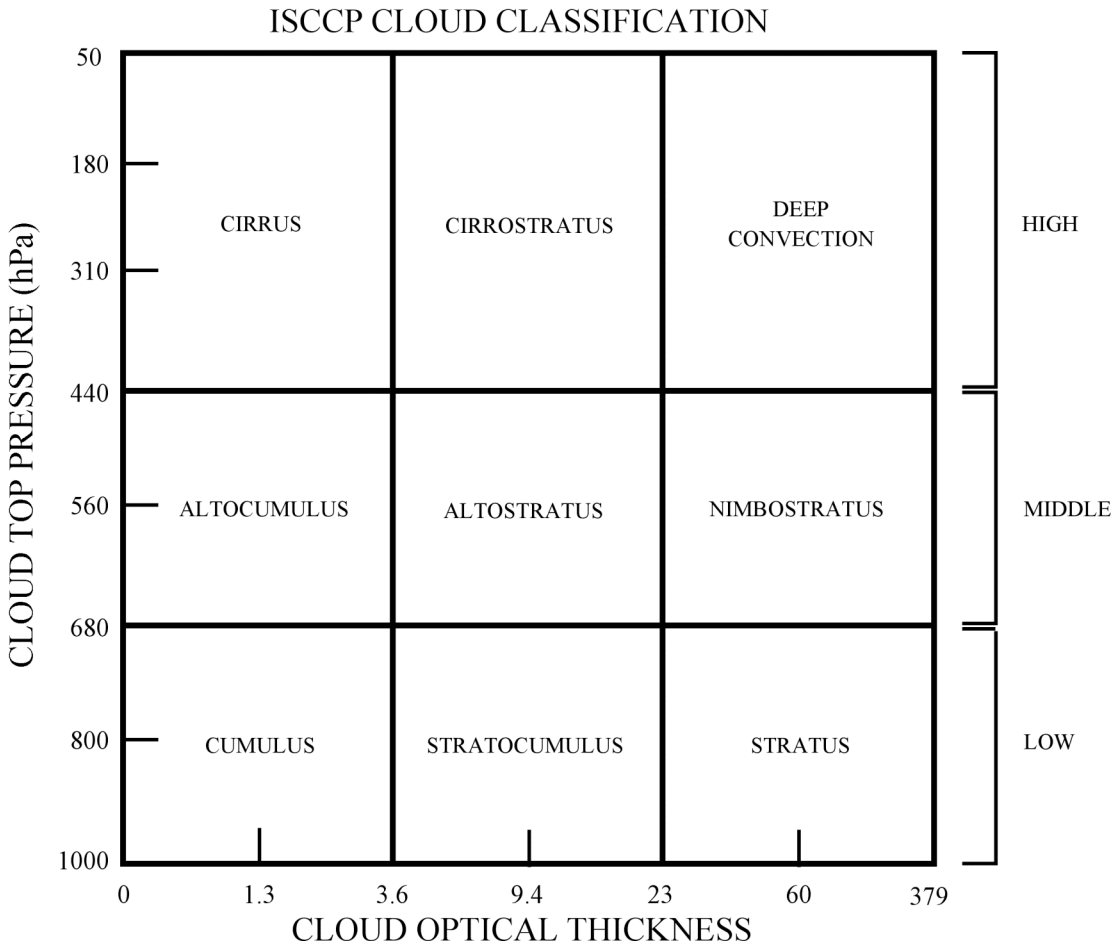

Figure 4.12 ISCCP cloud classification in *Rossow and Schiffer* [1999].

Table 4.1 shows the cloud classification for the daytime and nighttime during spring (the sum of FOVs observed on the date of 15th March, April, and May) and the corresponding MODIS products. The MODIS cloud properties are averaged for the collocated MODIS pixels within an AIRS level-1b pixel level (13.5 km at nadir). As mentioned before, high, middle, and low clouds are classified by the cloud top pressure (above 440 hPa, between 440 and 680 hPa, below 680 hPa, respectively). Following the traditional definitions in the literature [*Wylie and Menzel*, 1999; *Wylie et al.*, 1994], "thin" cloud is defined when the effective cloud amount (Nε) is smaller than 0.5, "thick" cloud is defined when Nε is between 0.5 and 0.95, and "opaque" cloud is defined when Nε is larger than 0.95. Both "thin" and "thick" clouds where Nε ≤ 0.95 are defined as transmissive clouds.

At daytime spring, AIRS shows that high clouds account for more than half of the chosen pixels within the selected oceanic area (145E-170E, 5S-2N). The number of high clouds is larger than that of the MODIS products. The number of "thick" clouds is the largest in high clouds similar to MODIS results. Middle clouds occupy the smallest portion of the chosen pixels. Most of the low clouds are comprised of "opaque" clouds, which are similar to the MODIS results. The number of AIRS pixels defined as clear is larger than that of the MODIS results.

At nighttime spring, high and middle clouds of AIRS increase while low clouds and clear pixels decrease. For high clouds, "thick" and "thin" clouds increase and "opaque" clouds decrease. For middle clouds, ""thick" and "opaque" clouds increase,

Table 4.1 Number of pixels in the daytime and nighttime for spring (sum of 15th March, April, and May) in the selected oceanic region (145-170E, 5S-2N).

Daytime Spring

	AIRS				MODIS			
	total	thin ($N\varepsilon < 0.5$)	thick ($N\varepsilon \geq 0.5$)	opaque ($N\varepsilon > 0.95$)	total	thin ($N\varepsilon < 0.5$)	thick ($N\varepsilon \geq 0.5$)	opaque ($N\varepsilon > 0.95$)
High Cloud	6291	2104	3130	1057	5576	1188	3732	656
Middle Cloud	1098	563	441	94	1242	131	1080	31
Low Cloud	2927	47	15	2865	4511	0	864	3647
Clear	1641				628			
total	11957	2714	3586	4016	11957	1319	5676	4334

Nighttime Spring

	AIRS				MODIS			
	total	thin ($N\varepsilon < 0.5$)	thick ($N\varepsilon \geq 0.5$)	opaque ($N\varepsilon > 0.95$)	total	thin ($N\varepsilon < 0.5$)	thick ($N\varepsilon \geq 0.5$)	opaque ($N\varepsilon > 0.95$)
High Cloud	6921	2452	3708	761	6499	1528	4648	323
Middle Cloud	1229	360	690	179	1449	126	1245	78
Low Cloud	2376	54	12	2310	3857	0	534	3323
Clear	1422				143			
total	11948	2866	4410	3250	11948	1654	6427	3724

Table 4.2 Number of pixels in the daytime and nighttime for summer (sum of 16th June, 15th July, and August) in the selected oceanic region (145-170E, 5S-2N).

Daytime Summer

	AIRS				MODIS			
	total	thin (Nε < 0.5)	thick (Nε ≥ 0.5)	opaque (Nε > 0.95)	total	thin (Nε < 0.5)	thick (Nε ≥ 0.5)	opaque (Nε > 0.95)
High Cloud	7732	2941	3636	1155	7077	1895	4703	479
Middle Cloud	865	469	335	61	965	73	880	12
Low Cloud	2294	61	8	2225	3329	0	834	2495
Clear	1032				552			
total	11923	3471	3979	3441	11923	1968	6417	2986

Nighttime Summer

	AIRS				MODIS			
	total	thin (Nε < 0.5)	thick (Nε ≥ 0.5)	opaque (Nε > 0.95)	total	thin (Nε < 0.5)	thick (Nε ≥ 0.5)	opaque (Nε > 0.95)
High Cloud	7918	3499	3172	1247	6992	2194	3982	816
Middle Cloud	576	313	245	18	1208	119	1075	14
Low Cloud	3002	45	3	2954	3694	0	862	2832
Clear	415				17			
total	11911	3857	3420	4219	11911	2313	5919	3662

and “thin” clouds decrease. The change of the number of cloud pixels is similar to the corresponding MODIS results.

For spring, high clouds (thick” and “thin” clouds) and middle clouds (“thick” and “opaque” clouds) increase, and low cloud and clear pixels decrease from daytime to nighttime for both AIRS and MODIS. Overall, “thin” and “thick” clouds increase, and “opaque” clouds decrease from daytime to nighttime for both AIRS and MODIS.

In Table 4.2, the cloud classification for daytime and nighttime summer is listed. For daytime summer, the number of high clouds in AIRS results is larger than that of MODIS results. While “thin” clouds account for slightly over half of the middle clouds for AIRS results, “thick” clouds are dominant in MODIS results. “Opaque” clouds are the major element in low clouds for both AIRS and MODIS. The number of clear pixels in AIRS results is larger than that in MODIS results.

At nighttime, “thin” clouds are most frequent in high and middle clouds for AIRS results. “Thick” clouds are most frequent in high and middle clouds for MODIS results, similar to the results at daytime. The number of high clouds is larger than half of the total pixel number for both AIRS and MODIS. High clouds comprise almost two thirds of the total number of pixels in the AIRS results. The number of high clouds in the AIRS results is larger than that in MODIS products.

High clouds account for a major portion of the classification at nighttime summer, similar to the daytime results. The number of “thin” and “opaque” high clouds of AIRS results is larger than that of MODIS. AIRS results have a smaller number of low and middle clouds than MODIS products. For all the atmospheric layers, “opaque”

clouds are more dominant than “thin” and “thick” clouds in AIRS results. Meanwhile, “thick” clouds are the major component in MODIS results.

The number of high clouds increases for nighttime summer; in detail, “thin” and “opaque” clouds increase, and “thick” clouds decrease for both AIRS and MODIS. Mid-level clouds decrease from daytime to nighttime in AIRS results, which is opposite in MODIS results. Low clouds increase and clear pixels decrease from daytime and nighttime for both AIRS and MODIS. Overall, “thin” and “opaque” clouds increase and “thick” clouds decrease from daytime to nighttime for both AIRS and MODIS.

Table 4.3 lists the cloud classification for daytime and nighttime autumn. At daytime autumn, high clouds are the main element (over 50%) in the classification, and “thick” clouds are the main component of the high clouds for both AIRS and MODIS. For MODIS, “thick” clouds comprise over half of the high clouds. Middle clouds are the least common element in the cloud height classification. Low clouds account for a significant portion in the classification for both AIRS and MODIS. Clear pixels constitute below 10% of all the pixels. Considering the effective cloud amount, “opaque” clouds are the main element for both AIRS and MODIS in daytime autumn.

For nighttime autumn, high clouds are the main element for both AIRS and MODIS, similar to the daytime results. While “thin” clouds account for over half of the high clouds in AIRS results, “thick” clouds are the main component in MODIS results. Middle clouds comprise the smallest portion in the classification for AIRS results, and the number of clear sky pixels is the smallest for MODIS results. Low clouds occupy the second largest portion in the classification for both AIRS and MODIS. Overall, “thin”

Table 4.3 Number of pixels in the daytime and nighttime for autumn (sum of 15th September, October, and November) in the selected oceanic region (145-170E, 5S-2N).

Daytime Autumn

	AIRS				MODIS			
	total	thin (Nε < 0.5)	thick (Nε ≥ 0.5)	opaque (Nε > 0.95)	total	thin (Nε < 0.5)	thick (Nε ≥ 0.5)	opaque (Nε > 0.95)
High Cloud	6429	2176	2954	1299	5878	1396	3742	740
Middle Cloud	259	119	117	23	634	62	570	2
Low Cloud	3374	24	3	3347	3874	0	560	3374
Clear	1441				1117			
total	11503	2319	3074	4669	11503	1458	4872	4116

Nighttime Autumn

	AIRS				MODIS			
	total	thin (Nε < 0.5)	thick (Nε ≥ 0.5)	opaque (Nε > 0.95)	total	thin (Nε < 0.5)	thick (Nε ≥ 0.5)	opaque (Nε > 0.95)
High Cloud	6890	3772	2710	408	6359	2773	3393	193
Middle Cloud	938	445	386	107	1219	169	1050	0
Low Cloud	3074	40	4	3030	3762	0	999	2763
Clear	1007				569			
total	11909	4257	3100	3545	11909	2942	5442	2956

Table 4.4 Number of pixels in the daytime and nighttime for winter (sum of 15th December, January, February) in the selected oceanic region (145-170E, 5S-2N).

Daytime Winter

	AIRS				MODIS			
	total	thin (Nε < 0.5)	thick (Nε ≥ 0.5)	opaque (Nε > 0.95)	total	thin (Nε < 0.5)	thick (Nε ≥ 0.5)	opaque (Nε > 0.95)
High Cloud	9639	4276	4079	1284	8391	3137	4467	787
Middle Cloud	296	214	78	4	748	115	633	0
Low Cloud	1726	27	11	1688	2050	0	669	1381
Clear	264				736			
total	11925	4517	4168	2976	11925	3252	5769	2168

Nighttime Winter

	AIRS				MODIS			
	total	thin (Nε < 0.5)	thick (Nε ≥ 0.5)	opaque (Nε > 0.95)	total	thin (Nε < 0.5)	thick (Nε ≥ 0.5)	opaque (Nε > 0.95)
High Cloud	10740	4691	4600	1449	10188	3860	5295	1033
Middle Cloud	90	57	32	1	609	81	523	5
Low Cloud	936	10	0	926	1030	0	432	598
Clear	63				2			
total	11829	4758	4632	2376	11829	3941	6250	1636

clouds occupy the largest portion for AIRS results, and “thick” clouds are the major element for MODIS results in terms of effective cloud amount.

High and middle clouds increase, and low cloud and clear sky pixels decrease from daytime to nighttime for both AIRS and MODIS. In detail, “thin” clouds in the high, middle and low levels increase, “thick” clouds in the middle and low levels increase, and “opaque” clouds in the high and low levels decrease.

Table 4.4 lists the cloud classification for winter. In the daytime, high clouds comprise a significant portion of the classification. In detail, “thin” and “thick” clouds mainly comprise high clouds for both AIRS and MODIS. The number of high clouds in AIRS results is a little larger than that of MODIS results. The number of clear sky pixels is the smallest, while middle clouds also occupy a very small portion of the classification for both AIRS and MODIS. Overall, “thin” clouds occupy the largest portion, by the effective cloud amount, in AIRS results, while “thick” clouds occupy the largest portion in MODIS results.

At nighttime, high clouds account for the largest portion, and middle cloud and clear sky pixels occupy less than 10% in total of the classification for both AIRS and MODIS, similar to the daytime results. Considering all levels, “thin” clouds are the largest element in AIRS results, and “thick” clouds are the largest one in MODIS results according to the effective cloud amount, which is also similar to the daytime results.

High clouds increase from daytime to nighttime for both AIRS and MODIS. Meanwhile, the other components, middle clouds, low clouds, and clear sky pixels, decrease. All of the elements in high clouds, “thin,” “thick,” and “opaque,” increase

while all of the elements in middle and low clouds decrease for both AIRS and MODIS results, except MODIS "opaque" middle clouds.

Several features are revealed from the analysis of daytime and nighttime cloud properties for the four seasons. (1) The number of high clouds of AIRS is larger than that of MODIS results. *Menzel et al*. [1992] reported that as the size of the observational area for the geostationary VAS [Visible-Infrared Spin Scan Radiometer (VISSR) Atmospheric Sounder] increases from 10 km × 10 km to 40 km × 80 km, the fraction of high clouds (cloud top pressure is less than 440 hPa) increases 10%. In this study, the AIRS results have 6% more high clouds than MODIS results. (2) The number of middle and low clouds of AIRS is smaller than that of MODIS results. (3) Clear sky pixels are decreased from daytime to nighttime. (4) High clouds are the main portion of the cloud classification for both AIRS and MODIS results. Low "thin" clouds are always 0 for MODIS results, while AIRS results have some pixels. (5) High cloud pixels are increased from daytime to nighttime for both AIRS and MODIS results except summer MODIS results. (6) High "thin" cloud pixels are increased from daytime to nighttime for both AIRS and MODIS results except summer MODIS results. (7) "Thin" cloud pixels increase from daytime to nighttime for both AIRS and MODIS results except summer MODIS results. (8) Middle or clear sky pixels occupy the smallest portion of the classification for both AIRS and MODIS results.

Tables 4.5, 4.6, and 4.7 list the high cloud distribution according to the visible optical thickness retrieved from AIRS and corresponding MODIS visible optical thickness, or effective cloud amount of AIRS and MODIS. There are four pre-conditions

to count the number of pixels: 1) the cloud top pressure should be less than 440 hPa, 2) the difference between cloud top pressures from AIRS and MODIS should be less than 50 hPa, 3) the difference between the effective cloud amounts from AIRS and MODIS should be less than 10%, and 4) the effective cloud amount should be larger than 0.1. These four conditions make the number of pixels selected for high clouds smaller than those in tables 4.1, 4.2, 4.3, and 4.4.

In table 4.5, following the ISCCP classification, a cloud optical thickness value of 3.6 is used to divide cloud type for high clouds. The number of pixels from MODIS with optical thickness less than 3.6 is larger than that of AIRS for daytime spring, summer, autumn, and winter. For the optical thicknesses larger than 3.6, it is the opposite. At nighttime, the number of pixels from AIRS with optical thickness less than 3.6 increased compared to daytime results. For autumn, even though the available total numbers from AIRS decreased at nighttime, the number of pixels with optical thickness less than 3.6 increased. Note that the information from MODIS is not available at nighttime because visible and near infrared channels are used to infer cloud optical thickness in the MODIS algorithm.

In table 4.6, a cloud optical thickness value of 1.4 is used to classify the high clouds. *Wylie and Menzel* [1999] used the following two equations, (4.45) and (4.46), to classify the cloud types by effective cloud amount values 0.5 and 0.95. They assumed that there are only transmission and emission with scattering.

$$\tau_{IRW} = -\ln(1 - N\varepsilon), \tag{4.45}$$

$$\tau_{VIS} / \tau_{IRW} = 2. \tag{4.46}$$

Table 4.5 Classification of clouds (above 440 hPa) in the daytime and nighttime by the visible cloud optical thickness (3.6) retrieved from AIRS and corresponding MODIS products.

Daytime

	AIRS			MODIS		
	total	$\tau_{vis} < 3.6$	$\tau_{vis} \geq 3.6$	total	$\tau_{vis} < 3.6$	$\tau_{vis} \geq 3.6$
Spring	1757	199	1558	1754	236	1518
Summer	2075	260	1815	2080	431	1649
Autumn	2481	273	2208	2475	320	2155
Winter	2537	326	2211	2516	662	1854
Total	8850	1058	7792	8825	1649	7176

Nighttime

	AIRS			MODIS		
	total	$\tau_{vis} < 3.6$	$\tau_{vis} \geq 3.6$	total	$\tau_{vis} < 3.6$	$\tau_{vis} \geq 3.6$
Spring	2315	529	1786	NA	NA	NA
Summer	1987	282	1705	NA	NA	NA
Autumn	1864	522	1342	NA	NA	NA
Winter	3299	540	2759	NA	NA	NA
Total	9465	1873	7592	NA	NA	NA

Table 4.6 Classification of high clouds (above 440 hPa) in the daytime and nighttime by the visible cloud optical thickness (1.4) retrieved from AIRS and corresponding MODIS products.

Daytime						
	AIRS			MODIS		
	total	$\tau_{vis} < 1.4$	$\tau_{vis} \geq 1.4$	total	$\tau_{vis} < 1.4$	$\tau_{vis} \geq 1.4$
Spring	1757	68	1689	1754	79	1675
Summer	2075	92	1983	2080	168	1912
Autumn	2481	81	2400	2475	134	2341
Winter	2537	122	2415	2516	282	2234
Total	8850	363	8487	8825	663	8162

Nighttime						
	AIRS			MODIS		
	total	$\tau_{vis} < 1.4$	$\tau_{vis} \geq 1.4$	total	$\tau_{vis} < 1.4$	$\tau_{vis} \geq 1.4$
Spring	2315	102	2213	NA	NA	NA
Summer	1987	90	1897	NA	NA	NA
Autumn	1864	164	1700	NA	NA	NA
Winter	3299	159	3140	NA	NA	NA
Total	9465	515	8950	NA	NA	NA

Table 4.7 Classification of high clouds (above 440 hPa) in the daytime and nighttime by the effective cloud amount (0.5) retrieved from AIRS and corresponding MODIS products.

Daytime						
	AIRS			MODIS		
	total	$N\varepsilon < 0.5$	$N\varepsilon \geq 0.5$	total	$N\varepsilon < 0.5$	$N\varepsilon \geq 0.5$
Spring	1764	218	1546	1764	202	1562
Summer	2086	314	1772	2086	295	1791
Autumn	2488	242	2246	2488	232	2256
Winter	2604	516	2088	2544	505	2039
Total	8942	1290	7652	8882	1234	7648

Nighttime						
	AIRS			MODIS		
	total	$N\varepsilon < 0.5$	$N\varepsilon \geq 0.5$	total	$N\varepsilon < 0.5$	$N\varepsilon \geq 0.5$
Spring	2318	328	1990	2321	301	2020
Summer	1998	303	1695	1998	298	1700
Autumn	1870	494	1376	1873	470	1403
Winter	3308	838	2470	3312	804	2508
Total	9494	1963	7531	9504	1873	7631

If effective cloud amount is 0.5 and there is no scattering, the visible optical thickness is about 1.4, which is used in table 4.6 to classify the cloud types. The AIRS results show small values compared to MODIS products in terms of the optical thickness less than 1.4 for daytime spring, summer, autumn, and winter, and the opposite pattern is shown for optical thickness larger than 1.4, similar to table 4.5. At nighttime (only the AIRS results are available), the number of pixels with optical thickness less than 1.4 increased from daytime, except nighttime summer.

Table 4.7 is a high cloud classification based on the effective cloud amount value, 0.5. In the daytime, the number of pixels from AIRS with effective cloud amount less than 0.5 is larger than that of MODIS for all seasons. The differences between AIRS and MODIS results for each category is small compared to the results in tables 4.5 and 4.6, which is not unexpected since effective cloud amounts of AIRS and MODIS are well correlated. For example, at daytime AIRS has 218 pixels for $N\varepsilon < 0.5$ and 1546 pixels for $N\varepsilon \geq 0.5$, while the corresponding MODIS results are 202 pixels and 1562 pixels, respectively. At nighttime, the pixels with effective cloud amount less than 0.5 increased from the daytime results, except in nighttime summer, similar to table 4.6.

Figure 4.13 shows the relation between AIRS window region (10.4 μm) brightness temperature and effective cloud amount for daytime and nighttime spring, summer, autumn, and winter. For a specific effective cloud amount, the corresponding window region brightness temperatures vary from a few degrees to a few tens of degrees

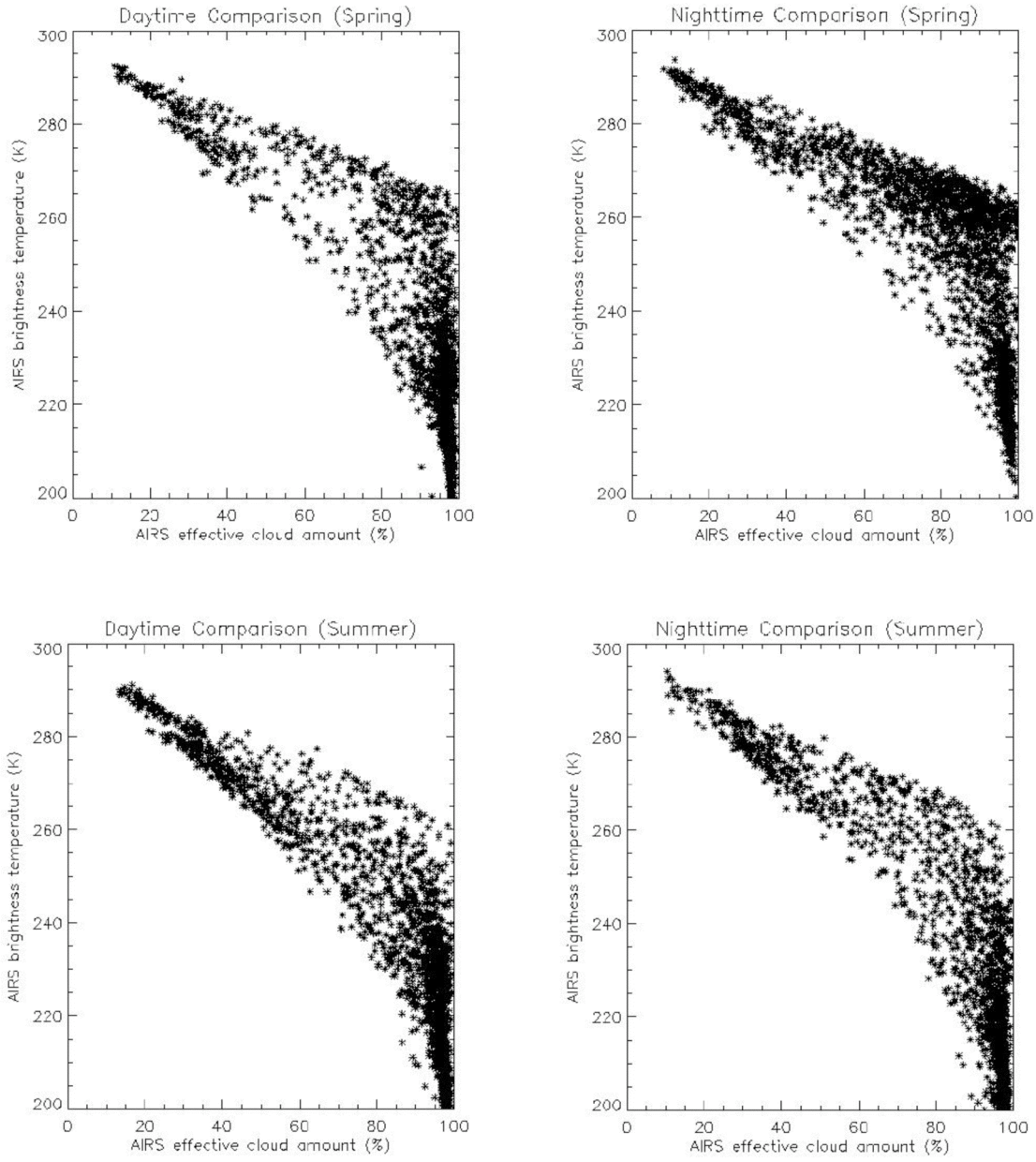

(a)

Figure 4. 13 Distribution of brightness temperature at 10.4 μm as a function of AIRS effective cloud amount. (a) Upper panel is for daytime and nighttime spring (sum of 15 March, 15 April, 15 May 2005), and lower panel is for summer (sum of 16 June, 15 July, 15 August 2005).

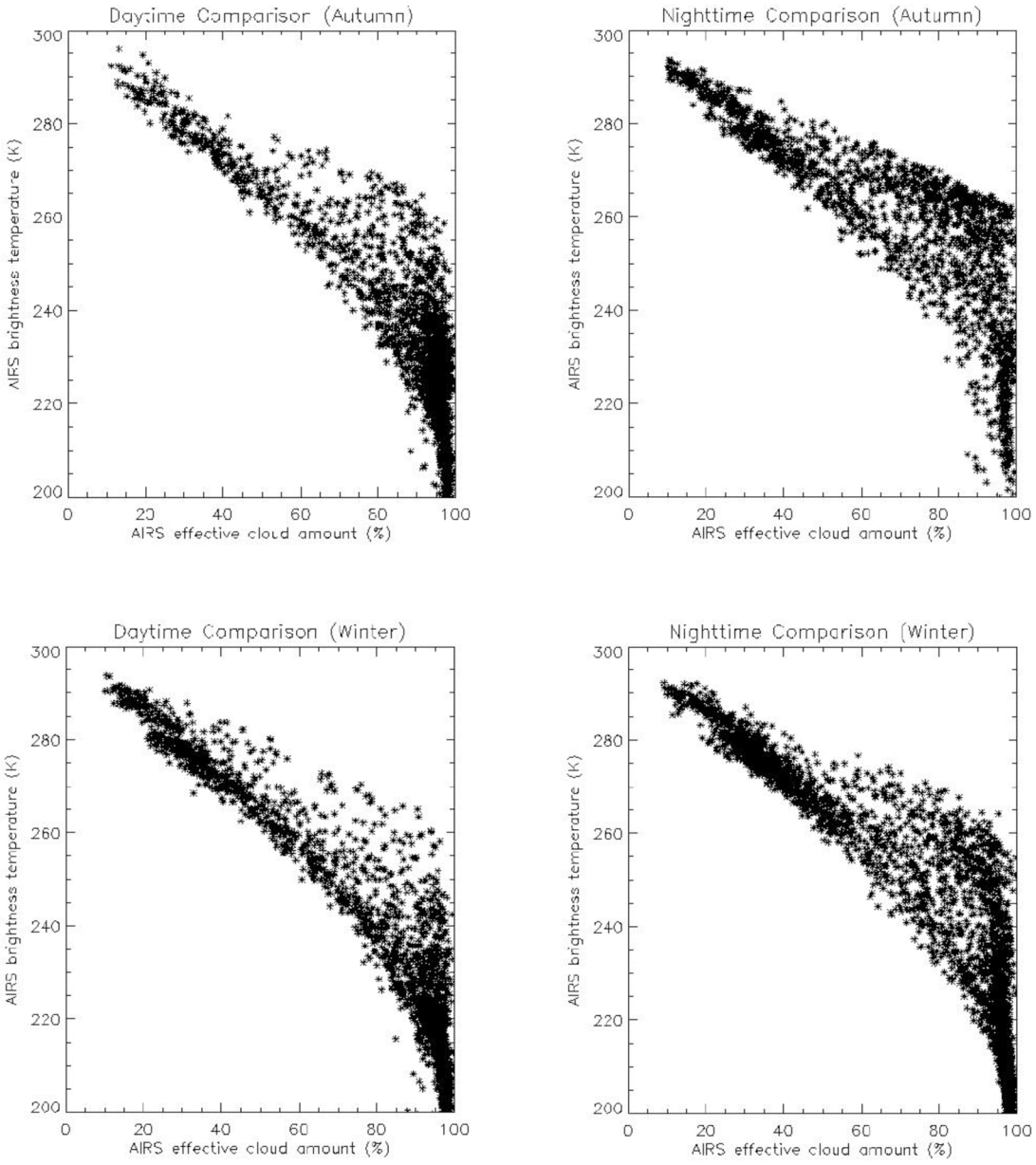

(b)

Figure 4. 13 Continued. (b) Upper panel is for daytime and nighttime autumn (sum of 15 October, 15 November 2004, 15 September 2005), and lower panel is for winter (the sum of 15 December 2004, 15 January, 15 February 2005).

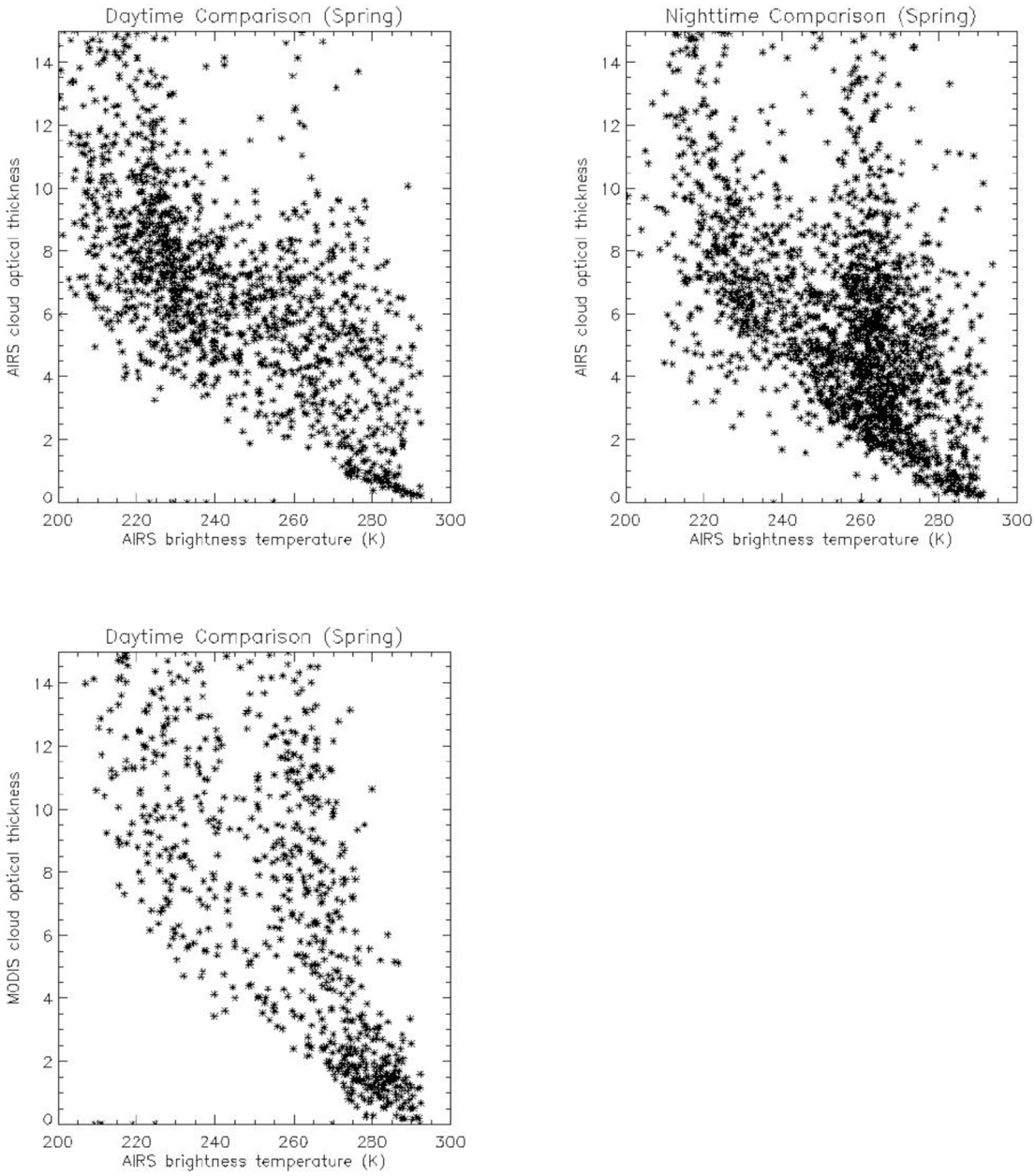

(a)

Figure 4.14 Distribution of cloud optical thickness retrieved from AIRS (upper panel) and MODIS (lower panel) as a function of AIRS brightness temperature at 10.4 μm. (a) For daytime and nighttime spring. Nighttime MODIS is not available.

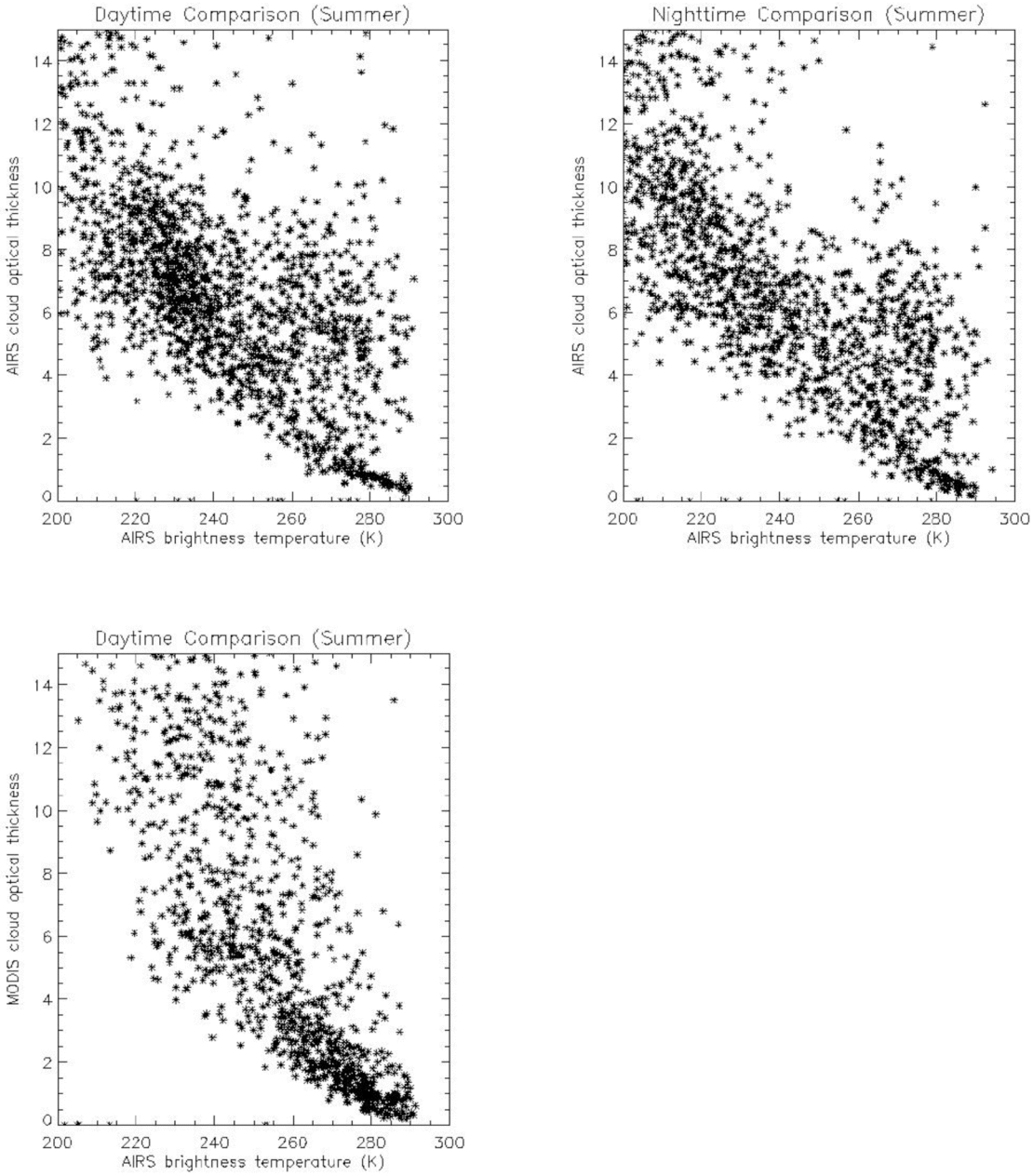

(b)
Figure 4.14 Continued. (b) For daytime and nighttime summer.

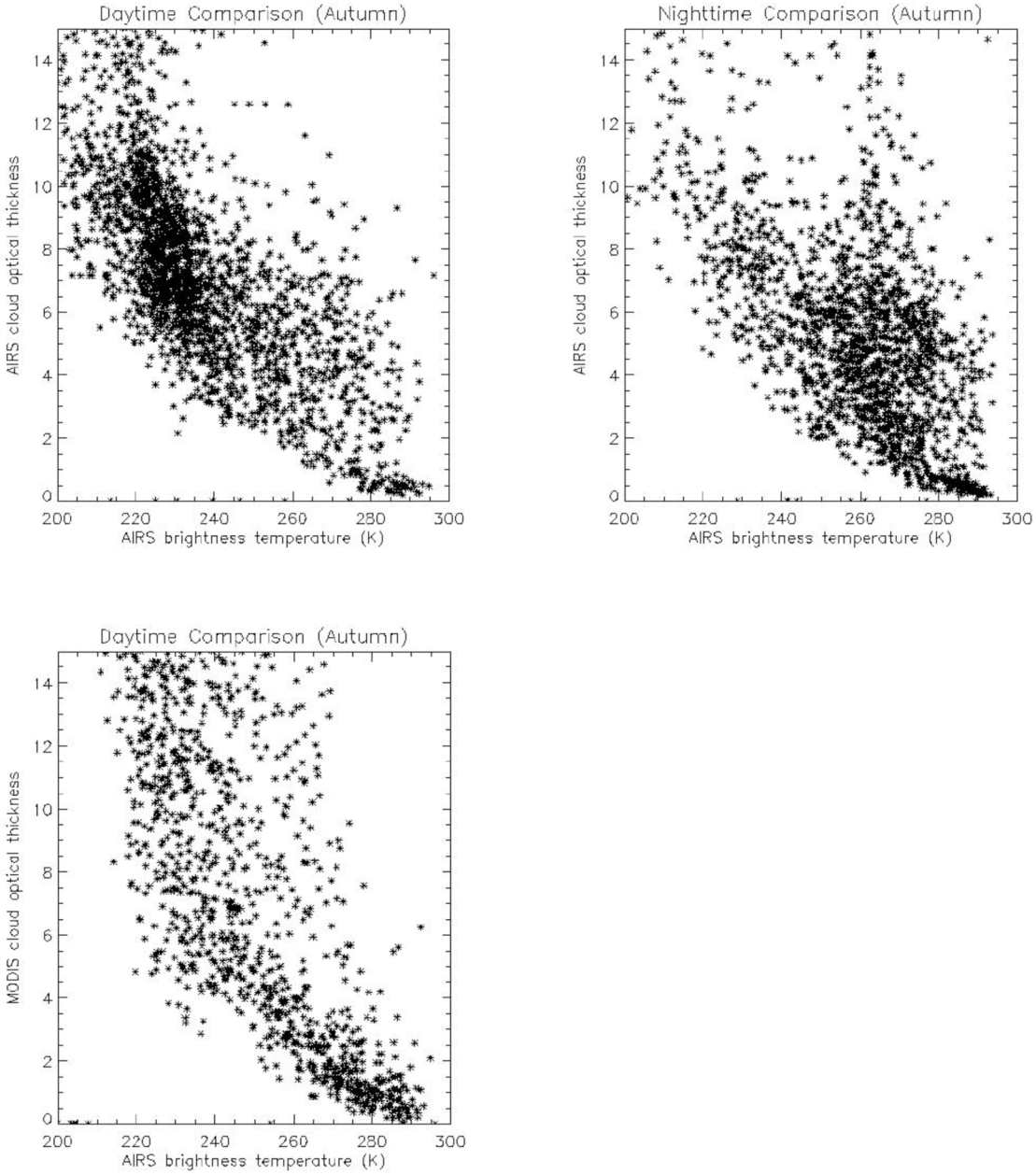

(c)

Figure 4.14 Continued. (c) For daytime and nighttime autumn.

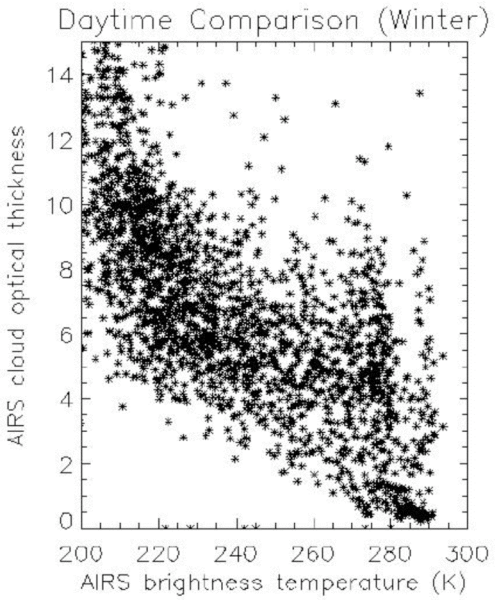

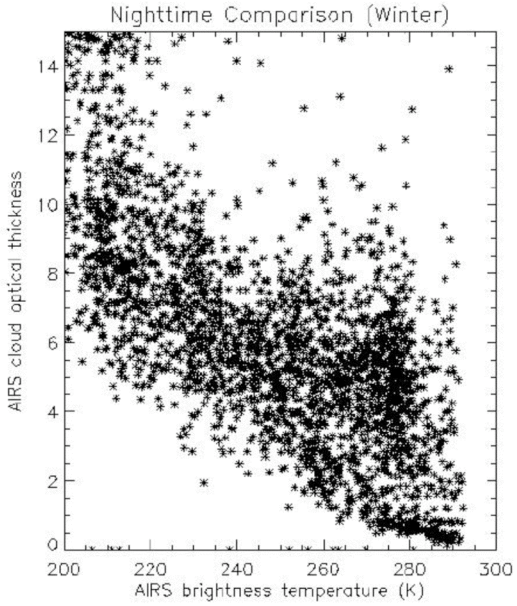

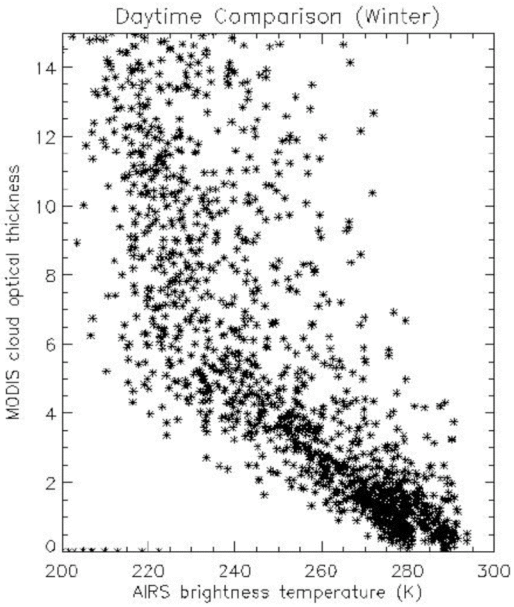

(d)

Figure 4.14 Continued. (d) For daytime and nighttime winter.

As the effective cloud amount increases, the brightness temperature decreases, and the variations of brightness temperature increase. For example, during daytime at an effective cloud amount of 20%, the range of brightness temperature is between 285 K and 290 K, while the brightness temperature varies between 250 K and 280 K with an effective cloud amount 60%. At nighttime spring, more pixels are located around the region where the brightness temperature is above 250 K. At nighttime autumn and winter, more pixels are located in the upper part of the brightness temperature variable range compared to the corresponding daytime results. The variation of the brightness temperature with an effective cloud amount at daytime is similar to the nighttime results for all the seasons.

Figure 4.14 shows the distribution of retrieved cloud optical thickness from AIRS and AIRS window region brightness temperature for the comparison of daytime and nighttime results for all the seasons. Normally, as the brightness temperature decreases, retrieved cloud optical thickness increases. At daytime spring, a cluster of pixels is located in the region where the brightness temperature is between 220 K and 240 K with the cloud optical thickness larger than approximately 5. At nighttime spring, the scattered pattern of optical thickness is changed. The number of pixels with the brightness temperature between 220 K and 240 K decreases, and pixels are densely located between 250 K and 280 K. It seems that the distribution of the optical thickness with respect to the window region brightness temperature has diurnal contrast from the different scattered pattern of daytime and nighttime results. *Tian et al.* [2004] showed that there exists a diurnal phase change in high cloud amount over tropical ocean, and

they mentioned the result is similar for each season. In their study, a high cloud is defined as a cloud that has brightness temperature at 11 μm less than 260 K. They showed that the brightness temperatures at 11 μm have diurnal phases, and the amount of high cloud (brightness temperature at 11 μm less than 260 K) has a maximum between 15 h and 18 h local time, and a minimum before the sunrise (See their Figs. 6 and 8). Since the AIRS granules selected in this study are observed between 12 h and 15 h (local time) at daytime and between 0h and 3h (local time) at nighttime, it is understandable that at daytime, a large number of pixels are located in the brightness temperature region between 220-240 K, and at nighttime, the number of pixels is decrease in the 220- 240 K region, and a dense region is located in the brightness temperature region between 250-280 K. MODIS products are available at daytime only. Pixels of cloud optical thickness of AIRS are denser in the brightness temperature region between 220 and 240 K compared to MODIS daytime results.

At daytime summer, there is a concentration of pixels with cloud optical thickness in the brightness temperature range between 220 K and 240 K. At nighttime summer, the concentration of pixels in the brightness temperature range between 220 K and 240 K becomes weaker. Compared to MODIS daytime results, AIRS results show concentration of pixels in the brightness temperature range between 220 and 240 K, similar to daytime spring.

At daytime autumn, the distribution of optical thickness is not scattered compared to other seasons. A concentration of pixels is located in the brightness temperature region between 220 K and 240 K. At nighttime autumn, the concentration in

the daytime becomes weaker, and a concentration is newly formed in the brightness temperature range between 250 K and 280 K. Compared to MODIS daytime results, AIRS daytime autumn results seem shifted toward smaller brightness temperatures, and a dense region is located in the brightness temperature range 220 K and 240 K.

At daytime winter, there is a concentrated region with pixels shifted slightly toward small brightness temperatures compared to other seasons, and the concentrated region is between 210 K and 240 K in terms of window region brightness temperature. At nighttime winter, the concentration at daytime becomes weaker, and a concentrated area of pixels shows up in the brightness temperature region between 250 K and 280 K, similar to other seasons. Compared to MODIS daytime results, the distribution of AIRS daytime winter cloud optical thickness shifted towards small values of brightness temperature, similar to autumn.

For all the seasons, pixels are densely located in the brightness temperature (at 10.4 μm) region between 220 and 240 K at daytime, and this feature is weakened at nighttime, which can be inferred from the diurnal phase of the brightness temperature at 11 μm of *Tian et al*. [2004].

Figure 4.15 shows the relation between the retrieved cloud optical thickness and effective cloud amount of AIRS. Normally, as the effective cloud amount increases, cloud optical thickness increases. In all the figures, it seems that there is a specific relationship between cloud optical thickness and the effective cloud amount, i.e., logarithmic increase of cloud optical thickness with respect to effective cloud amount.

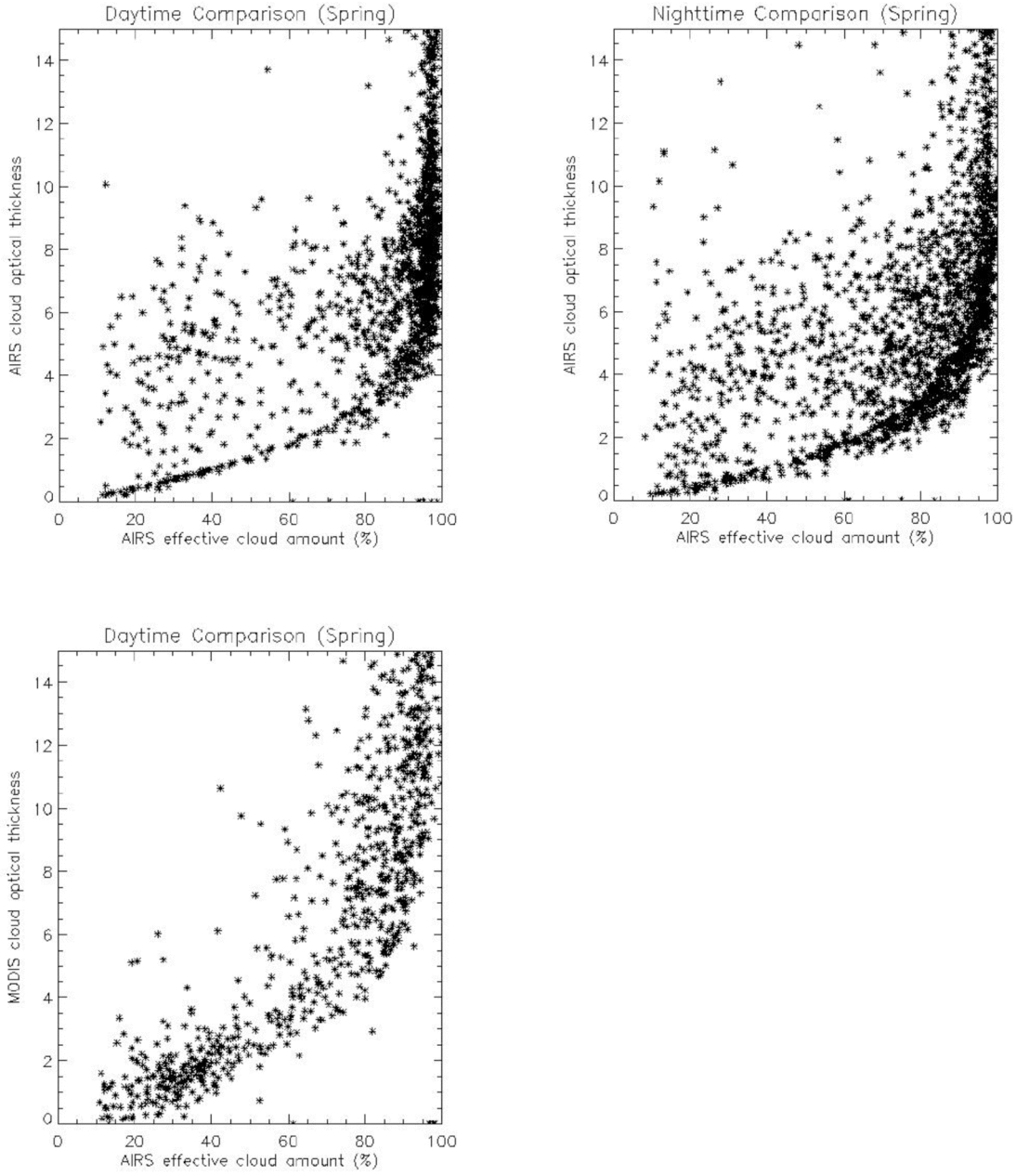

(a)

Figure 4.15 Distribution of cloud optical thickness retrieved from AIRS (upper panel) and MODIS (lower panel) as a function of effective cloud amount. (a) For daytime and nighttime spring. Nighttime MODIS is not available.

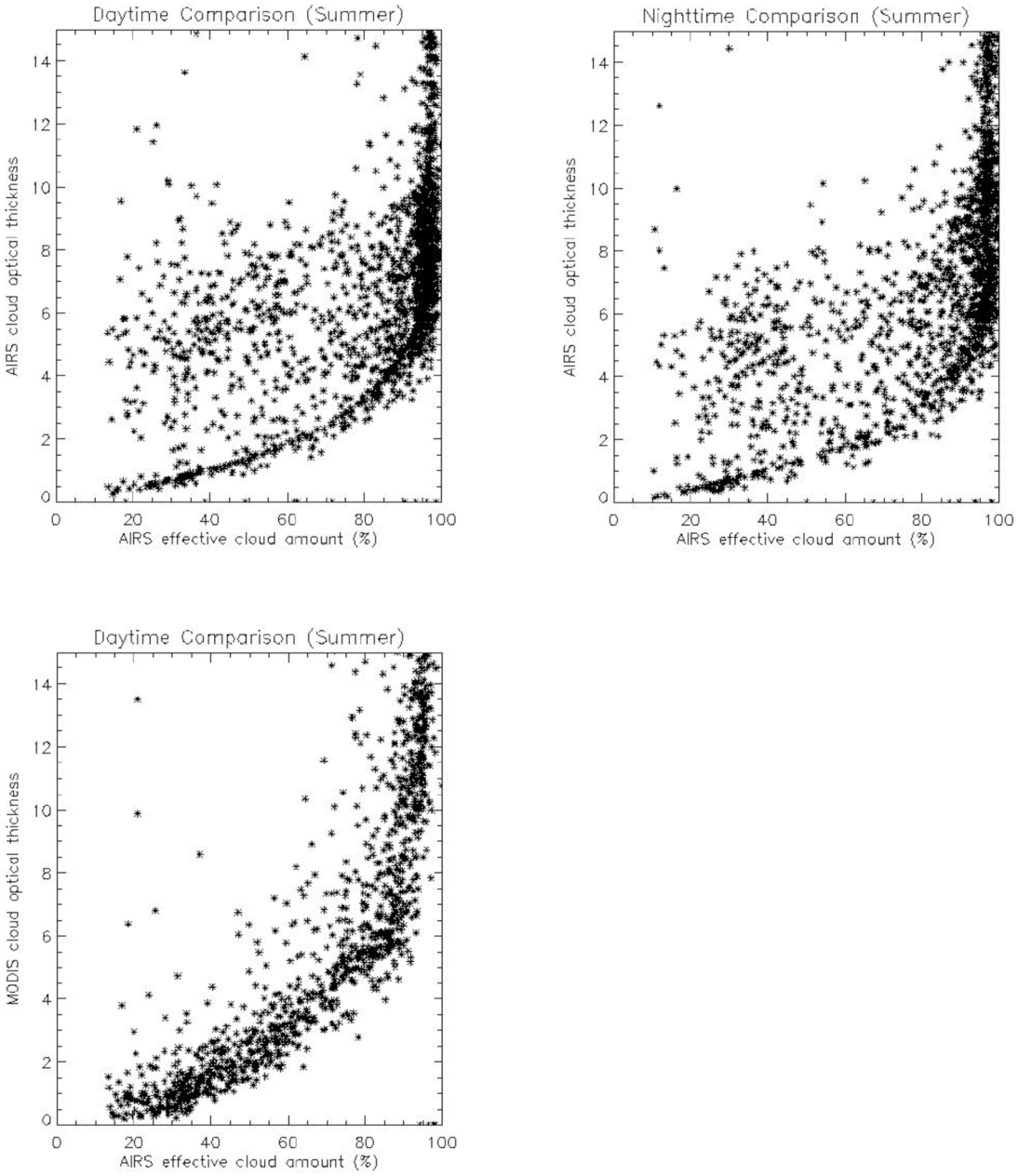

(b)
Figure 4.15 Continued. (b) For daytime and nighttime summer.

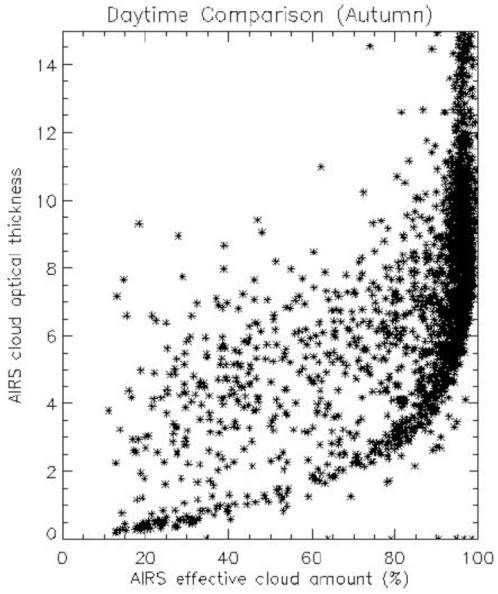

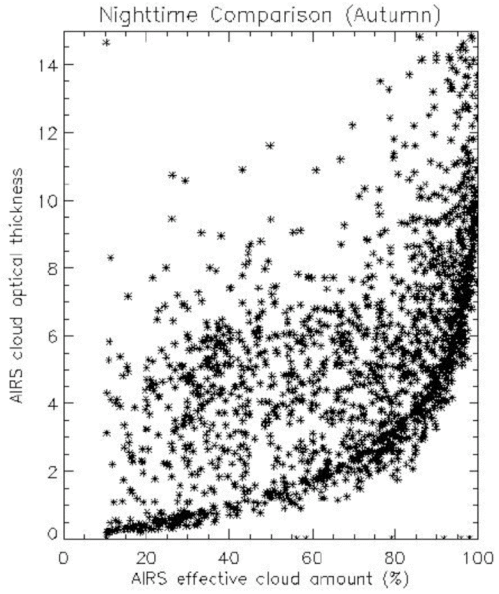

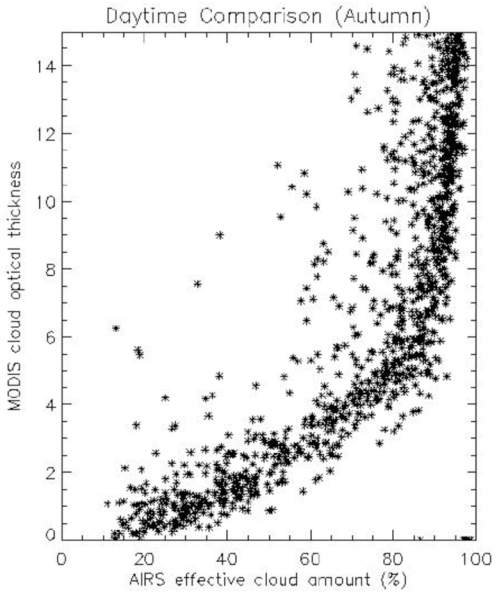

(c)

Figure 4.15 Continued. (c) For daytime and nighttime autumn.

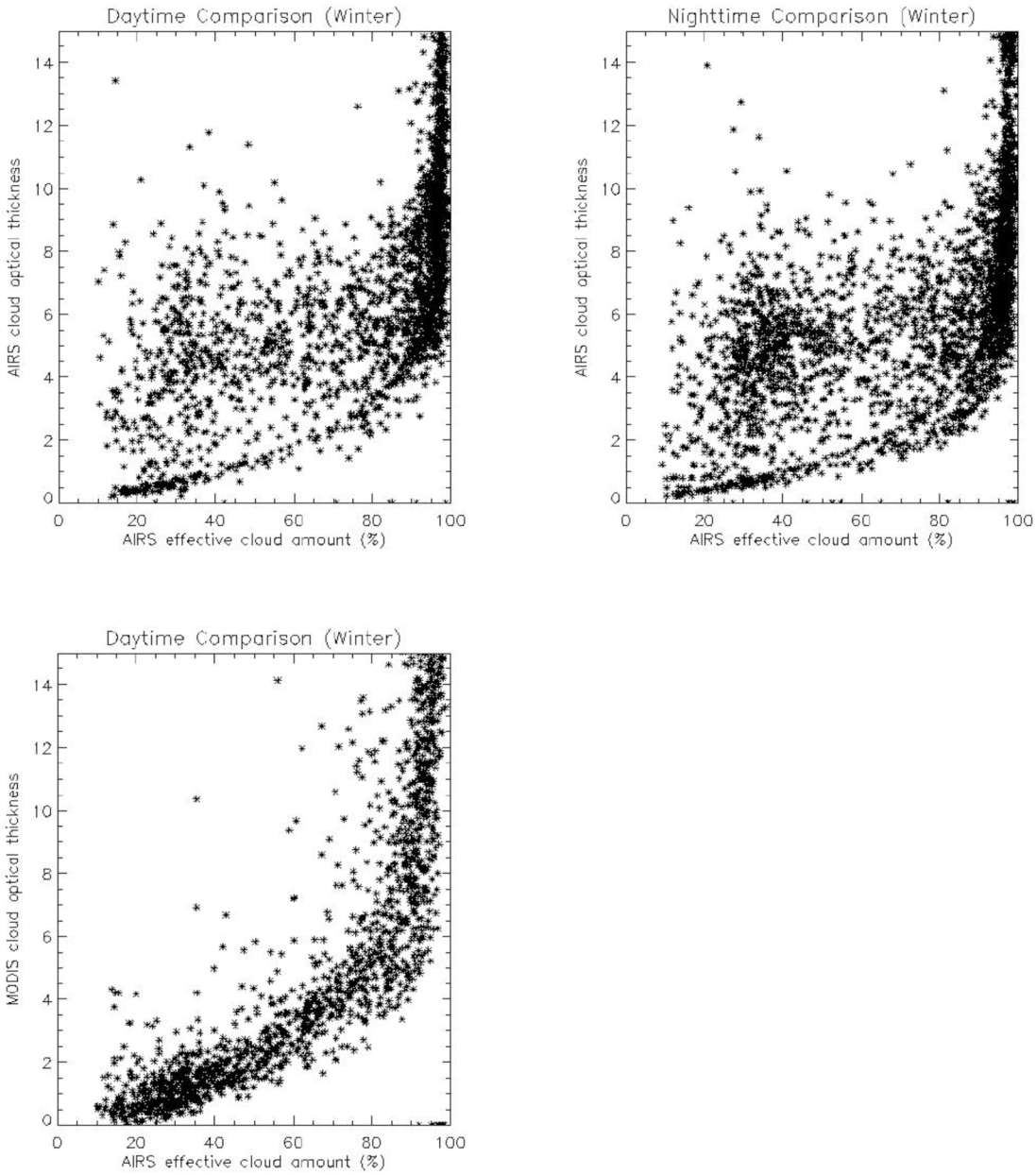

(d)

Figure 4.15 Continued. (d) For daytime and nighttime winter.

Most of the pixels are located above that bottom line. This relationship is given by Eqs. (4.45) and (4.46), and the solid lines in each figure are from those equations.

For daytime spring, pixels are located above the logarithmic relation between cloud optical thickness and effective cloud amount. Pixels are concentrated in the region where effective cloud amount is larger than 0.9. For nighttime spring, the concentration in the region of $N\varepsilon > 0.9$ becomes weaker, while the number of pixels for $N\varepsilon < 0.9$ increases. MODIS daytime spring cloud optical thickness is not scattered compared to the corresponding AIRS results and shows a logarithmic increase in terms of effective cloud amount, but is located above the solid lines from Eqs. (4.45) and (4.46).

In summer, there is no significant change between the daytime and nighttime distribution of optical thickness in terms of effective cloud amount. The coincidence with the solid lines from Eqs. (4.45) and (4.46) does not appear in the MODIS daytime summer results. Also, a concentrated area of pixels in the effective cloud amount region, $N\varepsilon > 0.9$, does not appear in MODIS daytime summer results. In autumn, pixels are thronged in the effective cloud amount of $N\varepsilon > 0.9$ at daytime, a feature that becomes weaker at nighttime. At nighttime, the number of pixels in the effective cloud amount $N\varepsilon < 0.9$ increases compared to daytime results. In winter, the number of pixels in the effective cloud amount range, $0.3 < N\varepsilon < 0.6$, increases at nighttime compared to the daytime results.

MODIS daytime results show that as effective cloud amount increases, cloud optical thickness also increases. For small effective cloud amount, cloud optical

thickness matches, normally in MODIS results, while even for small effective cloud amount, larger cloud optical thickness matches in AIRS results.

Figure 4.16 shows the retrieved cloud fraction as a function of effective cloud amount of AIRS for daytime and nighttime for each season. The cloud fractions vary between 1 (100%) and the value of effective cloud amount. The number of pixels which have cloud fraction between 1 (100%) and effective cloud amount is small compared to those with cloud fraction close to the effective cloud amount or almost 1 (100%). *Wylie and Menzel* [1999] showed that for thick clouds ($N\varepsilon > 0.5$), most of the HIRS pixels were completely covered by clouds, indicating that the change of effective cloud amount is caused by the cloud emissivity; meanwhile, for thin clouds ($N\varepsilon < 0.5$), effective cloud amount also varies with cloud fraction. However, effective cloud amount and cloud fraction show similar values for a significant portion of pixels in this study.

Figure 4.17 shows the retrieved effective particle size distribution in terms of effective cloud amount of AIRS and the corresponding MODIS daytime results. Since effective particle size of cloud strongly depends on the accuracy of retrieved cloud optical thickness, effective particle size is selected when the optical thickness is below 5 and the viewing zenith angle is less than 10°. For each season, there is no significant variation between daytime and nighttime AIRS results. The effective particle size does not depend on the effective cloud amount or daytime and nighttime.

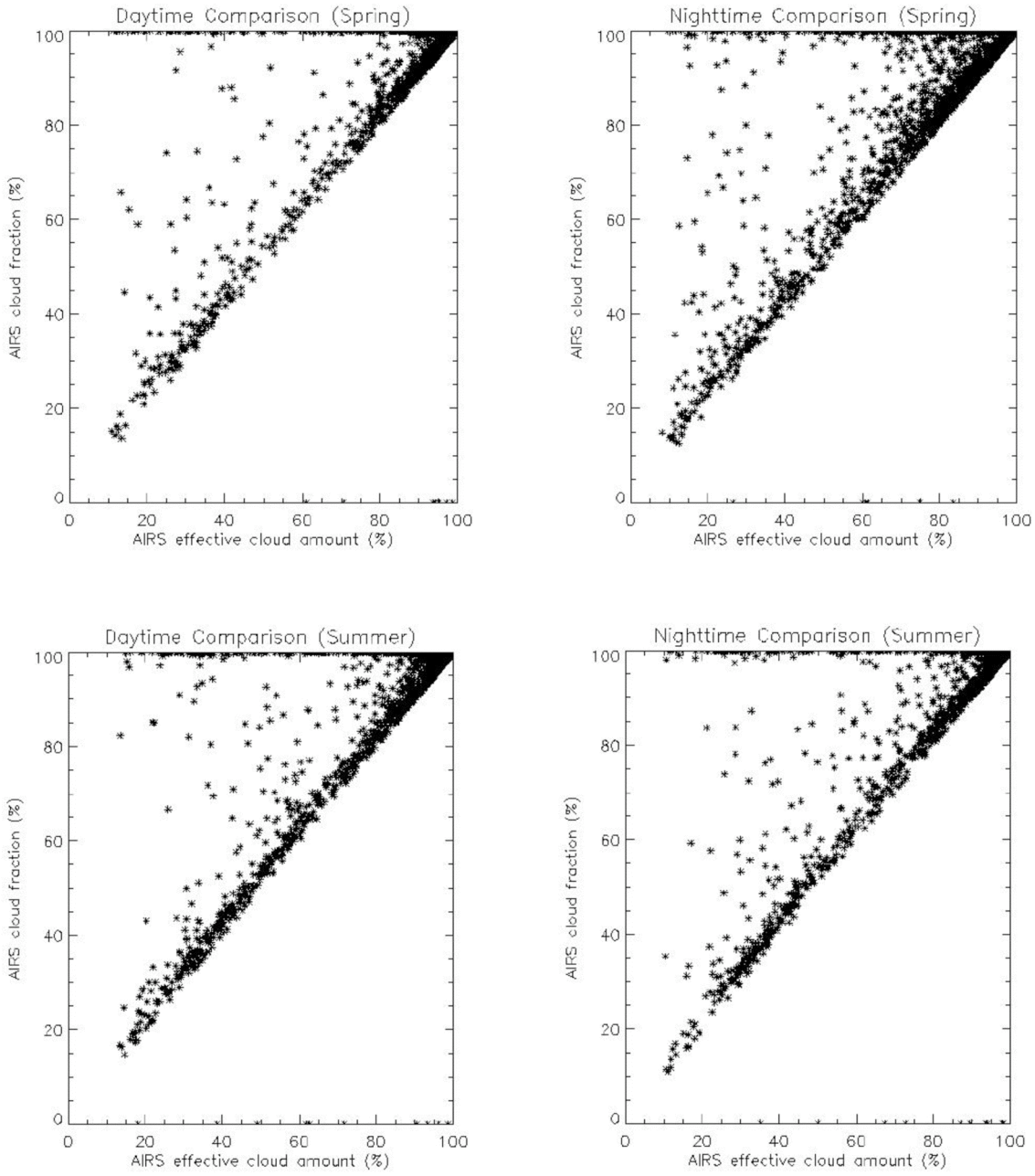

(a)

Figure 4.16 Retrieved cloud fraction from AIRS as a function of effective cloud amount. (a) For daytime and nighttime spring (upper panel) and for daytime and nighttime summer (lower panel).

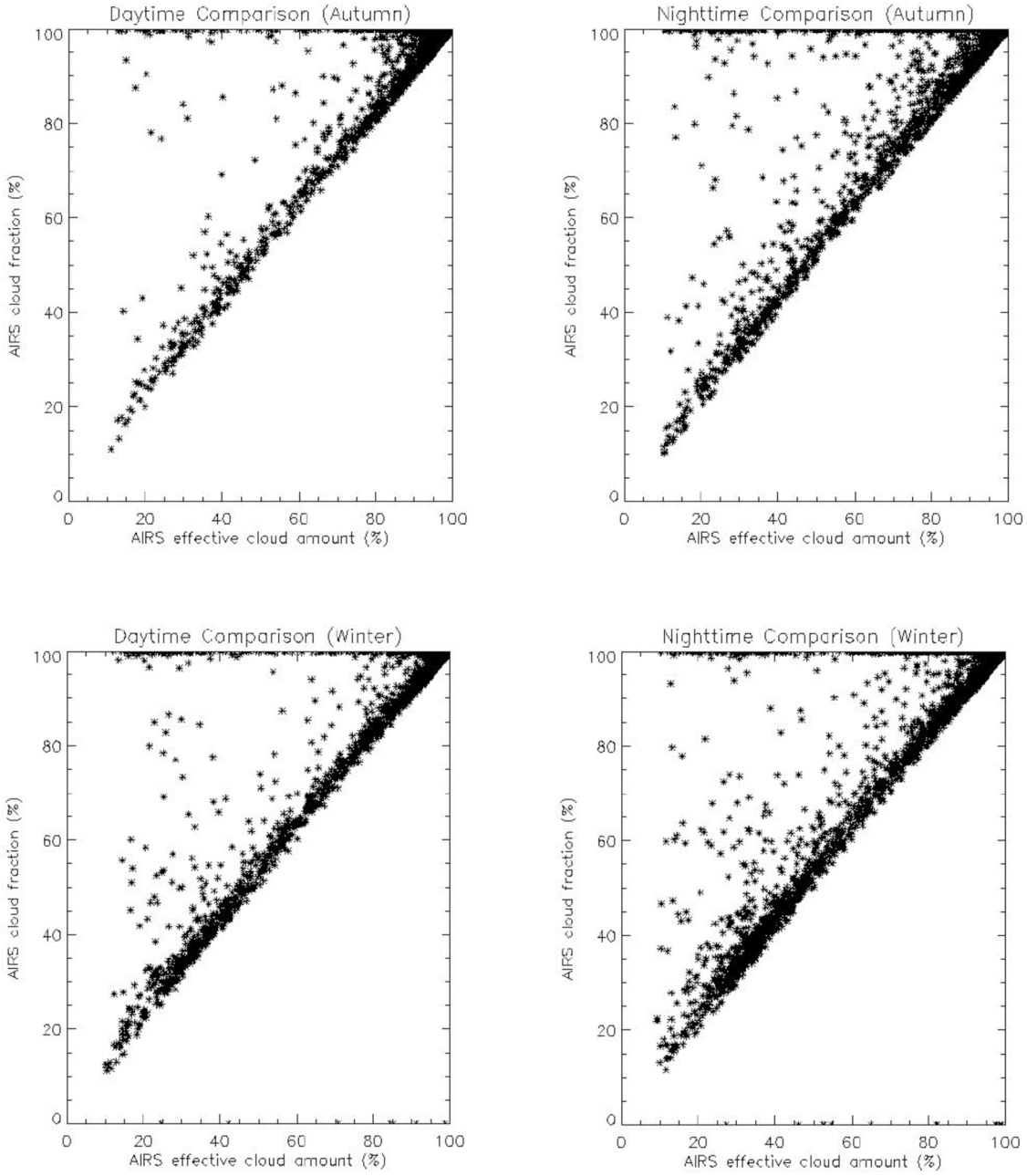

(b)

Figure 4.16 Continued. (b) For daytime and nighttime autumn (upper panel) and for daytime and nighttime winter (lower panel).

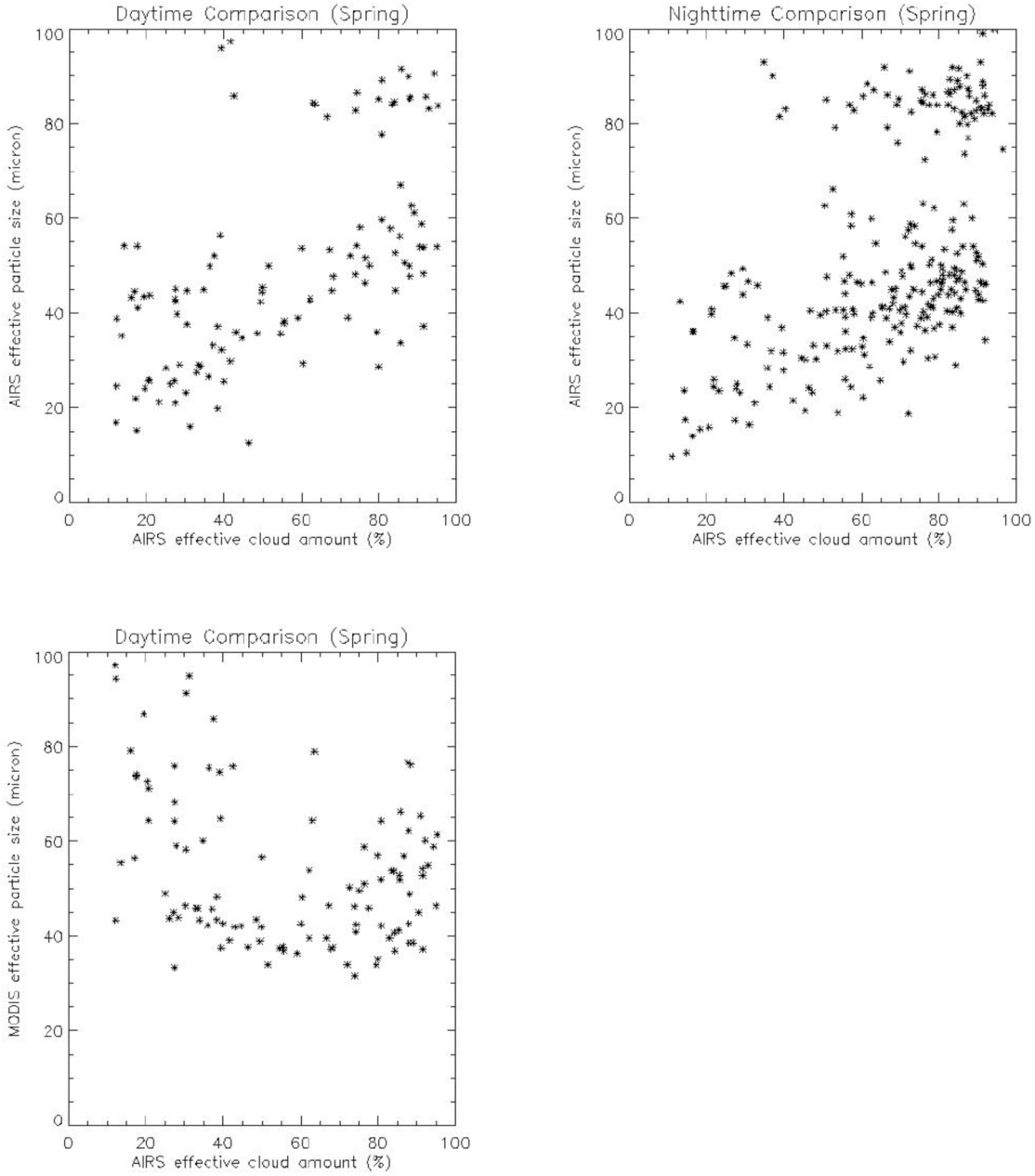

(a)

Figure 4.17 Distribution of cloud effective particle size retrieved from AIRS (upper panel) and MODIS (lower panel) as a function of effective cloud amount. (a) For daytime and nighttime spring. Nighttime MODIS is not available.

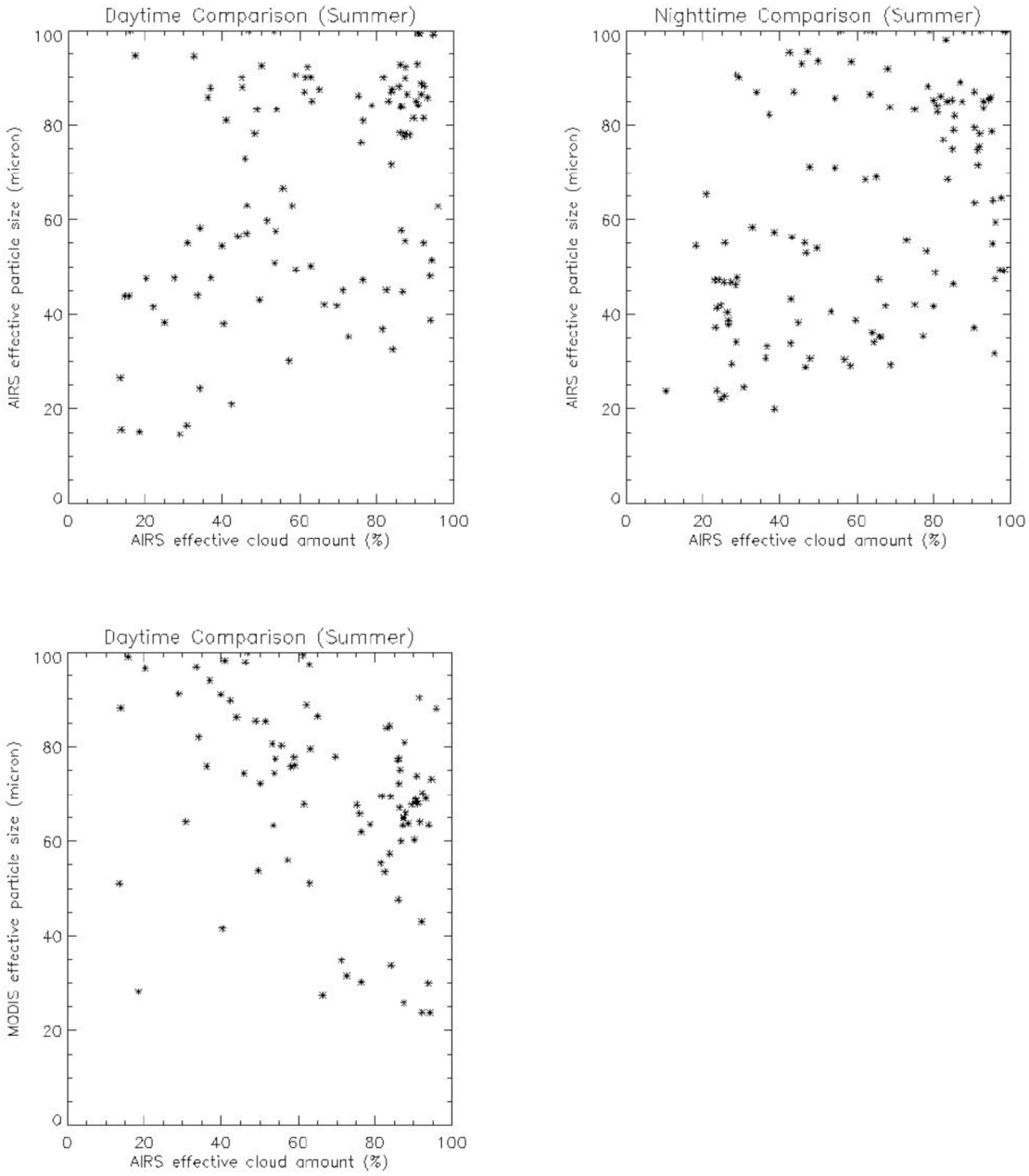

(b)

Figure 4.17 Continued. (b) For daytime and nighttime summer.

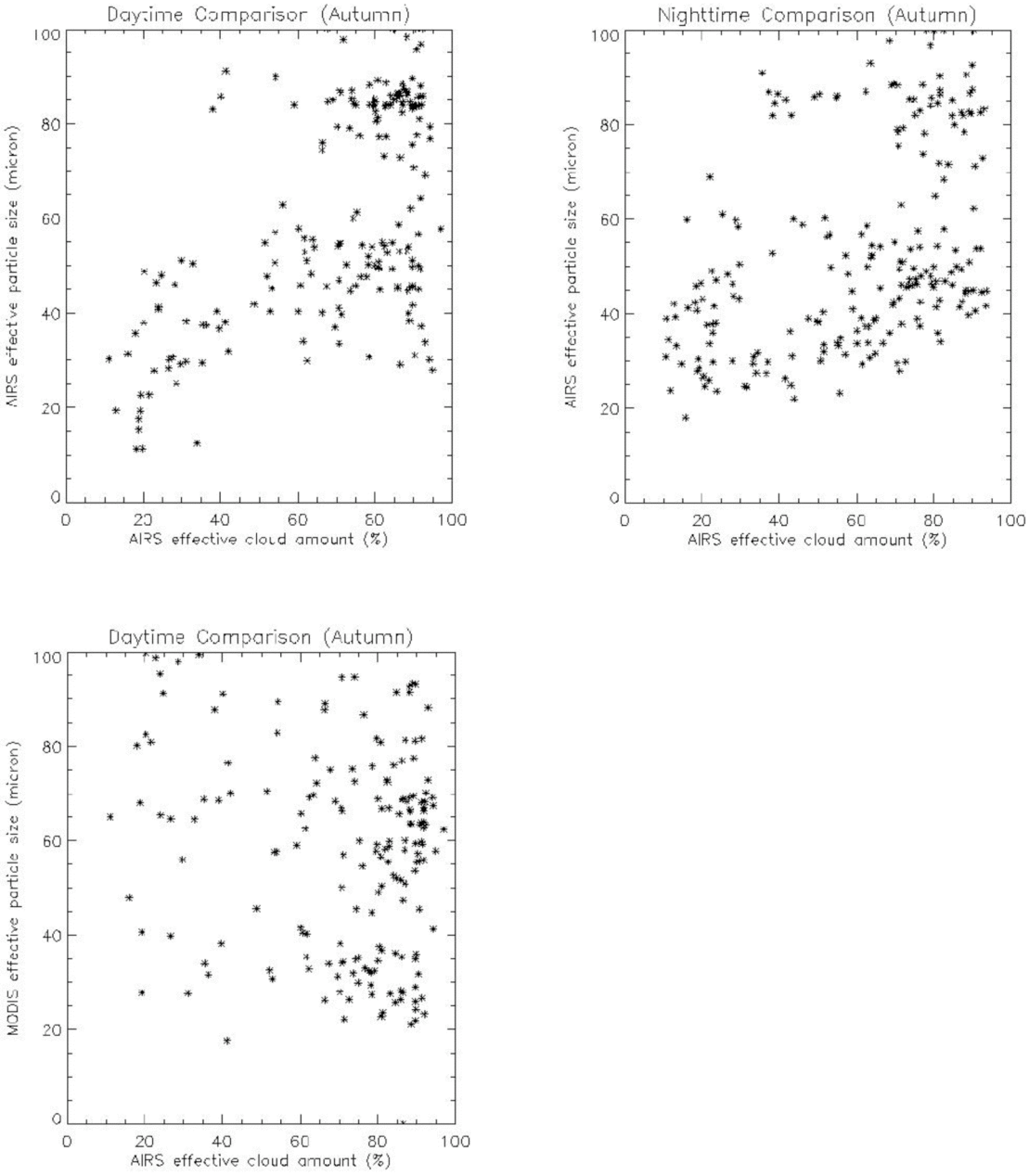

(c)

Figure 4.17 Continued. (c) For daytime and nighttime autumn.

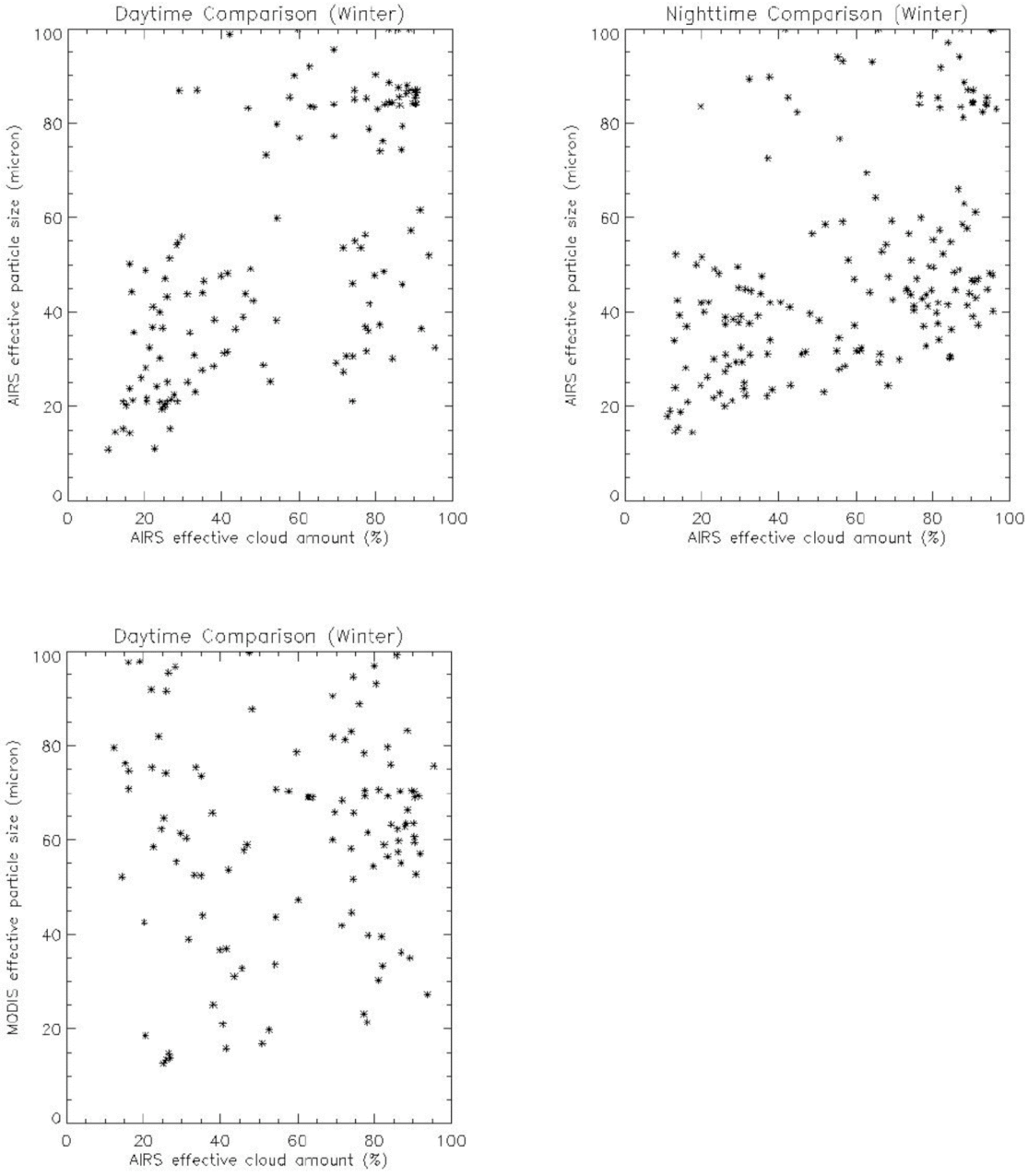

(d)

Figure 4.17 Continued. (d) For daytime and nighttime winter.

CHAPTER V

CONCLUSIONS

5.1 Use of circular cylinders as surrogates for hexagonal pristine ice crystals in scattering calculations at infrared wavelengths

The accuracy of approximating hexagonal crystals as circular cylinders in the computation of the optical properties of pristine ice crystals is investigated in the infrared spectral (8-12 μm) region. Various definitions are used to define the equivalence of the circular cylindrical particle for a hexagonal column. The T-matrix computational program is used to solve for the single-scattering properties of circular cylinders.

For extinction efficiency, absorption efficiency, and asymmetry factor, the differences between the results for the two geometries are less than 10%. In general, the errors for particles having sizes smaller than 20 μm are more significant than the errors for larger particles. For particle sizes larger than 40 μm, the differences are essentially on the order of a few percent. At λ = 8.5 μm, the circular cylinder with an equivalent ratio of the volume to the surface area yields smaller difference in the computation of absorption efficiency, as compared to the cases for the equivalent-volume or equivalent-surface circular cylinders. This difference is particularly pronounced for particle sizes less than 40 μm. At λ = 11 μm, the definition of equivalence for circular cylinder has negligible effect on the calculation of absorption efficiency when particle sizes are larger than 15 μm. Detailed comparison of the numerical computations associated with various

equivalence definitions of circular cylinders indicates that the equivalence based on the ratio of V/A is most suitable for absorption efficiency when the two geometries have the same aspect ratio ($a / L = R / H$), and the volume equivalence is suitable for asymmetry factor or phase function calculations when the two geometries have the same length ($L=H$). The error ranges for equivalence-area, equivalent-volume, and equivalent V/A are slightly different in the computation of extinction efficiency. In general, the errors associated with the use of circular cylinders as surrogates for hexagonal ice crystals in scattering calculations at infrared wavelengths are on the order of a few percent. As such, it quite reasonable to approximate the geometry of pristine ice crystals as circular cylinders in the study of infrared radiation.

It is also shown that it is not proper to approximate a complex aggregate geometry with a simplified geometry such as a hexagonal column for computing the optical properties. Because aggregates and bullet rosettes are common in cirrus clouds, there is a need to include their particle geometry in modeling of the optical properties of cirrus particles even at infrared wavelengths. Future research will explore a surrogate particle that better approximates the more complex crystal geometries found in nature. Particularly, it will be worthwhile to investigate whether it is valid to approximate an aggregate ice crystal by using a number of individual cylinders based on the method developed by *Grenfell and Warren* [1999] who suggested an equivalence of a circular cylinder and a monodisperse sphere (with the same volume-to-surface ratio) system for scattering and radiative transfer computations.

5.2 Potential nighttime contamination of CERES clear-sky fields of view by optically thin cirrus during the CRYSTAL-FACE campaign

A set of 76 CERES FOVs that are deemed to be free of clouds by the operational CERES cloud clearing procedure are investigated. The clear-sky radiances are calculated using a forward radiative transfer model and compared to the measured radiances. The temperature and humidity profiles are taken from the rawinsondes launched during the CRYSTAL-FACE campaign in July 2002. It is found that the calculated LW and WIN channel radiances are larger than those measured by CERES. A possible mechanism for these differences could be the presence of thin cirrus clouds. Clouds with optical thicknesses less than approximately 0.2 to 0.3 are difficult to detect, much less analyze.

In the present analyses of CERES data, the cirrus optical thicknesses range generally between $0.03 < \tau_{vis} < 0.3$. It seems that thin cirrus clouds were ubiquitous in this region around Florida during CRYSTAL-FACE. The results obtained herein are somewhat similar to the result of *Dessler and Yang* [2003] who noticed that about one third of the MODIS pixels flagged as confidently clear actually contained detectible thin cirrus. As their study used the MODIS 1.38 μm band, their approach is not applicable for analyzing nighttime data. The present study is focused on a set of 76 CERES FOVs rather than the large number of daytime MODIS pixels ($>10^7$), and a wide geographical region (tropical area) encompassed in their study. We find that as ice cloud effective diameter increases, the optical thickness inferred from both the LW and WIN channels converges. This study is complementary to *Dessler and Yang* [2003], as they used

daytime MODIS observations, and most of the CERES FOVs used in this study are for nighttime.

The anisotropic factors show some differences between the observed and calculated values at the LW and WIN bands. The comparison shows that the difference decreases with increasing viewing zenith angle to 50°. Since anisotropy factors of the observed radiances are larger than those of the calculated radiances for the viewing zenith angles between 0° and 50°, it is likely possible to underestimate (by a few percent) CERES LW and WIN fluxes that are associated with the scenes that are flagged as cloud free. The difference in the anisotropic factors is small compared to the corresponding large difference in radiance between the CERES observations and the theoretical calculations. The error in flux is related to the error in anisotropic factor. If the CERES anisotropic factor is overestimated by a typical value of 0.2% due to the neglect of the presence of thin cirrus clouds within the CERES FOVs, the LW flux would be underestimated by approximately 0.2%, or 0.6 Wm^{-2}, given a typical clear-sky LW flux of 300 W/m^2. An error would arise in the interpretation of the flux since the FOV is classified as clear sky rather than cloudy.

A sensitivity study showed that even by accounting for the uncertainties caused by several factors (excluding the presence of cirrus), such as in the temperature and humidity profiles, there is still some disagreement between the simulated for both the LW and WIN channel radiances under clear-sky conditions and their CERES observed counterparts.

While *Dessler and Yang* [2003] showed thin cirrus clouds are ubiquitous using a daytime data set, thin cirrus clouds could also be common over the Florida region at nighttime. Therefore, the radiances measured for the FOVs that are identified as "clear-sky" could be contaminated by the existence of thin cirrus clouds with optical thickness less than 0.3. Further research using active measurements during nighttime conditions would be quite useful.

5.3 Retrieval of cloud properties from Atmospheric Infrared Sounder (AIRS) data

Cloud properties, such as cloud top pressure, effective cloud amount, cloud phase, cloud optical thickness, and effective particle size are retrieved from AIRS, a state-of-the-art hyspectral infrared radiometric instrument on the Aqua satellite. These cloud properties are compared with the corresponding MODIS products. In total, 52 granules are selected from the oceanic region (between 5° S and 2° N in latitude, and between 140° E and 170° E in longitude) for every 15th date (except for the 16th of June 2005) in each month between October 2004 and September 2005. Three days are summed for daytime and nighttime contrast and seasonal comparison. The hyspectral infrared channel information from AIRS observation is used in this study, which makes it possible to investigate cloud properties at both daytime and nighttime conditions. The advantages of the developed method in this study are that the cloud property retrieval is available, and thus cloud optical thickness and effective particle size can be compared for daytime and nighttime.

High clouds occupy the largest portion in every season, and both middle clouds and clear sky pixels comprise the smallest portion of the cloud classification using the ISCCP definitions for both AIRS and MODIS. For every season, high clouds increase at nighttime compared to the daytime results for both AIRS and MODIS.

Since the developed method in this study for detecting cloud optical thickness and effective particle size is valid for high clouds (above 440 hPa), cloud optical thickness and effective particle size for high clouds are investigated for high clouds. The accuracy of cloud optical thickness and effective particle size retrievals depends on the viewing zenith angle. The accuracy of the cloud optical thickness significantly affects the retrieval of effective particle size.

Cloud classifications by visible cloud optical thickness, 3.6 and 1.4, or effective cloud amount value of 0.5, are made in this study. The number of cloudy pixels with cloud optical thickness less than 3.6 (or 1.4) increases at nighttime compared to daytime, except for nighttime summer when the cloud optical thickness is 1.4. The number of cloudy pixels with effective cloud amount less than 0.5 also increase during the nighttime compared to the daytime except the nighttime summer.

The brightness temperature at 10.4 μm is related to the effective cloud amount. Between 250 K and 280 K, the number of pixels increases at nighttime for spring, autumn, and winter.

The visible cloud optical thickness appears dense at a window region brightness temperature at 10.4 μm below 240 K in the daytime, and this feature becomes weaker at

nighttime. As the brightness temperature at 10.4 μm decreases, the minimum value of cloud optical thickness increases.

Some of the visible cloud optical thickness is directly related to the effective cloud amount of the pixel with Eqs. (4.45) and (4.46). A large portion of the cloud optical thickness exists above the line from the Eqs (4.45) and (4.46).

The diurnal contrast is clear for the cloud properties, such as cloud optical thickness and effective cloud amount including the brightness temperature at 10.4 μm, and the strength of the diurnal contrast may depend on the season.

REFERENCES

Ackerman, S. A., K. I. Strabala, W. P. Menzel, R. A. Frey, C. C. Moeller, and L. E. Gumley (1998), Discriminating clear sky from clouds with MODIS, *J. Geophys. Res., 103*, 32141-32157.

Antonelli, P., S. A. Ackerman, W. P. Menzel, H.-L. Huang, B. A. Bryan, and W. L. Smith (2001), Retrieval of cloud top height, effective emissivity, and particle size from aircraft high spectral resolution infrared measurements, paper presented at SPIE VIth Conference on Remote Sensing of Clouds and the Atmosphere, Toulouse, France, 17-20 September, 50-61.

Arnott, W. P., Y. Y. Dong, and J. Hallett (1995), Extinction efficiency in the infrared (2-18 μm) of laboratory ice clouds: Observations of scattering minima in the Christiansen bands of ice, *Appl. Opt., 34*, 541-551.

Arnott, W. P., Y. Y. Dong, J. Hallett, and M. R. Poellot (1994), Role of small ice crystals in radiative properties of cirrus: A case study, FIRE II, November 22, 1991, *J. Geophys. Res. 99*, 1371-1381.

Aumann, H. H., M. T. Chahine, C. Gautier, M. D. Goldberg, E. Kalnay, L. M. McMillin, H. Revercomb, P. W. Rosenkranz, W. L. Smith, D. H. Staelin, L. L. Strow, and J. Susskind (2003), AIRS/AMSU/HSB on the Aqua mission: Design, science objectives, data products, and processing systems, *IEEE Trans. Geosci. Remote Sensing, 41*, 253-264.

Baran, A. J., P. Francis, and P. Yang (2003), A process study of the dependence of ice crystal absorption on particle geometry: application to aircraft radiometric

measurements of cirrus clouds in the terrestrial window region, *J. Atmos. Sci. 60*, 417-427.

Baran, A. J., P. N. Francis, P. Yang, and S. Havemann (2002), Simulation of scattering from ice aggregates using size/shape distributions of circular ice cylinders: An application of T-matrix, paper presented at the Sixth Conference on Light Scattering by Nonspherical Particles, Gainesville, FL., 4-10 March, 25-28.

Baran, A. J., and S. Havemann (2000), Comparison of electromagnetic theory and various approximations for computing the absorption efficiency and single-scattering albedo of hexagonal columns, *Appl. Opt. 39*, 5560-5568.

Baran, A. J., P. Yang, and S. Havemann (2001), Calculation of the single-scattering properties of randomly oriented hexagonal ice columns: A comparison of the T-matrix and the finite-difference time-domain methods, *App. Opt. 40*, 4376-4386.

Barber, P. W., and S. C. Hill (1990), Light scattering by particles: Computational Methods, World Scientific, Singapore.

Baum, B. A., A. J. Heymsfield, P. Yang, and S. Thomas (2005a), Bulk scattering models for the remote sensing of ice clouds. 1: Microphysical data and models, *J. Appl. Meteorol. 44*, 1885-1895.

Baum, B. A., D. Kratz, P. Yang, S. C. Ou, Y. X. Hu, P. F. Soulen, and S. C. Tsay (2000), Remote sensing of cloud properties using MODIS airborne simulator imagery during SUCCESS, 1, Data and models, *J. Geophys. Res. 105*, 11767-11780.

Baum, B. A., P. Yang, A. J. Heymsfield, S. Platnick, M. D. King, and S. Thomas (2005b), Bulk scattering models for the remote sensing of ice clouds. 2: Narrowband models, *J. Appl. Meteorol.*, *44*, 1896-1911.

Cess, R. D., M. H. Zhang, W. J. Ingram, G. L. Potter, V. Alekseev, et al. (1996), Cloud feedback in atmospheric general circulation models: An update, *J. Geophys. Res., 101*, 12791-12794.

Cess, R. D., M. H. Zhang, G. L. Potter, V. Alekseev, H. W. Barker, et al. (1997), Comparison of the seasonal change in cloud-radiative forcing from atmospheric general circulation models and satellite observations, *J. Geophys. Res.*, *102*, 16593-16603.

Chahine, M. T. (1974), Remote sounding of cloudy atmospheres. I: The single cloud layer, *J. Atmos. Sci., 31*, 233-243.

Chepfer, H., G. Brogniez, and Y. Fouquart (1998), Cirrus clouds microphysical properties deduced from POLDER observations, *J. Quant. Spectrosc. Radiat. Transfer, 60*, 375-390.

Chepfer, H., P. Goloub, J. Riedi, J. F. De Hann, J. W. Hovenier, and P. H. Flamant (2001), Ice crystal shapes in cirrus clouds derived from POLDER/ADEOS-1, *J. Geophys. Res., 106,* 7955-7966.

Chylek, P., and G. Videen (1994), Longwave radiative properties of polydispersed hexagonal ice crystal, *J. Atmos. Sci. 51*, 175-190.

Dessler, A. E., and P. Yang (2003), The distribution of tropical thin cirrus clouds inferred from Terra MODIS data, *J. Climate*, *16*, 1241-1247.

Ebert, E. E. and J. A. Curry (1992), A parameterization of ice cloud optical properties for climate models, *J. Geophys. Res. 97*, 3831-3836.

Foot, J. S. (1988), Some observations of the optical properties of clouds: II. Cirrus, *Quart. J. Roy. Meteor. Soc. 114*, 145-164.

Francis, P. N., A. Jones, R. W. Saunders, K. P. Shine, A. Slingo, Z. Sun (1994), An observational and theoretical study of the radiative properties of cirrus: Some results from ICE'89, *Quart. J. Roy. Meteor. Soc. 120,* 809-848.

Fu, Q. (1996), An accurate parameterization of the solar radiative properties of cirrus clouds for climate models, *J. Clim., 9*, 2058-2082.

Fu, Q., W. B. Sun and P. Yang (1999), On model of scattering and absorption by cirrus nonspherical ice particles at thermal infrared wavelength, *J. Atmos. Res., 56*, 2937-2947.

Fu, Q., P. Yang, and W. B. Sun (1998), An accurate parameterization of the infrared radiative properties of cirrus clouds for climate models, *J. Climate 11*, 2223-2237.

Gaiser, S. L., H. H. Aumann, L. L. Strow, S. E. Hannon, and M. Weiler (2003), In-flight spectral calibration of the Atmospheric Infrared Sounder, *IEEE Trans. Geosci. Remote Sensing*, *41*, 287-297.

Gao, B.-C., P. Yang, W. Han, R.-R. Li, and W. Wiscombe (2002), An algorithm using visible and 1.38 channels to retrieve cirrus reflectances from aircraft and satellite data, *IEEE Trans. Geosci. Remote Sensing, 40,* 1659-1668.

Garrett, T. J., L. F. Radke, and P. V. Hobbs (2002) Aerosol effects on cloud emissivity and surface longwave heating in the artic, *J. Atmos. Sci., 59*, 769-778.

Geier, E. B., R. N. Green, D. P. Kratz, P. Minnis, W. F. Miller, S. K. Nolan, C. B. Franklin (2003), Clouds and the Earth's Radiant Energy System (CERES) Data Management System: Single Satellite Footprint TOA/Surface Fluxes and Clouds (SSF) Collection Document, http://asd-www.larc.nasa.gov/ceres/collect_guide, 243pp.

Grenfell, T. C. and S. G. Warren (1999), Representation of a nonspherical ice particle by a collection of independent spheres for scattering and absorption of radiation. *J. Geophys Res.,104*, 31697-31709.

Hansen, J. E. (1971), Multiple scattering of polarized light in planetary atmospheres. Part II. Sunlight reflected by terrestrial water clouds, *J. Atmos. Sci., 28,* 1400-1426.

Hansen, J. E., and L. D. Travis (1974), Light scattering in planetary atmosphere, *Space Sci. Rev.*, *16*, 527-610.

Havemann, S. and A. J. Baran (2001), Extension of T-matrix to scattering of electromagnetic plane waves by non-axisymmetric dielectric particles: application to hexagonal ice cylinders, *J. Quant. Spectrosc. Radiat. Transfer 70*, 139-158.

Heidinger, A. (1998), Nadir sounding of clouds and aerosol in the O2 A-band, Atmos. Sci. Pap. 650, 226 pp., Colo. State Univ., Fort Colins, Colo.

Heidinger, A. K. (2003), Rapid daytime estimation of cloud properties over a large area from radiance distributions. *J. Atmos. Oceanic Technol., 20*, 1237-1250.

Heymsfield, A. J. and J. Iaquinta (2000), Cirrus crystal terminal velocities, *J. Atmos. Sci. 57*, 916-938.

Heymsfield, A. J., S. Lewis, A. Bansemer, J. Iaquinta, L. M. Miloshevich, M. Kajikawa, C. Twohy, and M. R. Poellot (2002), A general approach for deriving the properties of cirrus and stratiform ice cloud particles, *J. Atmos. Sci. 59*, 3-29.

Huang, H.-L., P. Yang, H. Wei, B. A. Baum, Y. Hu, P. Antonelli, and S. A. Ackerman (2004), Inference of ice cloud properties from high spectral resolution infrared observation, *IEEE Trans. Geosci. Remote Sensing*, *42*, 842-853.

Jensen, E., D. Starr, and O. B. Toon (2004), Mission investigates tropical cirrus clouds, *Eos Trans. AGU, 85(5)*, 45, 50.

Kahn, B. H., K. N. Liou, S. Y. Lee, E. F. Fishbein, S. Desouza-Machado, A. Eldering, E. J. Fetzer, S. E. Hannon, L. L. Strow (2005), Nighttime cirrus detection using atmospheric infrared sounder window channels and total column water vapor, *J. Geophys. Res., 110(D7),* 07203, doi: 10.1029/2004JD005430.

Kahnert, F. M., J. J. Stamnes, and K. Stamnes (2002), Can simple particle shapes be used to model scalar optical properties of an ensemble of wavelength-sized particles with complex shapes?" *J. Quant. Spectrosc. Radiat. Transfer 19*, 521-531.

King, M. D., W. P. Menzel, Y. J. Kaufman, D. Tanré, B. C. Gao, S. Platnick, S. A. Ackerman, L. A. Remer, R. Pincus, and P. A. Hubanks (2003), Cloud and Aerosol Properties, Precipitable Water, and Profiles of Temperature and Humidity from MODIS, *IEEE Trans. Geosci. Remote Sensing, 41,* 442-458.

King, M. D., S. Platnick, P. Yang, G. T. Arnold, M. A. Gray, J. C.Riedi, S. A. Ackerman, and K. N. Liou (2004), Remote sensing of liquid water and ice cloud

optical thickness, and effective radius in the arctic: Application of air-borne multispectral MAS data, *J. Atmos. and Ocean. Technol., 21*, 857-875.

Kristjansson, J. E., J. M. Edwards, and D. L. Mitchell (2000), The impact of a new scheme for optical properties of ice crystals on the climate of two GCMs, *J. Geophys. Res., 105*, 10063-10079.

Laitinen, H., and K. Lumme (1998), T-matrix method for general star-shaped particles: first results, *J. Quant. Spectrosc. Radiat. Transfer, 60*, 325-334.

Lee, R. B., B. R. Barkstrom, D. A. Crommclynck,G. L. Smith, W. C. Bolden, J. Paden, D. K. Pandey, S. Thomas, L. Thornhill, R. S. Wilson, K. A. Bush, P. C. Hess, and W. L. Weaver (1997), Clouds and the Earth's Radiant Energy System (CERES) Algorithm Theoretical Basis Document: Instrument Geolocate and Calibrate Earch Radiances (Subsystem 1.0), http://asd-www.nasa.gov/ATBD/ATBD.html, 84 pp.

Lee, R. B., B. R. Barkstrom, G. L. Smith, J. E. Cooper, L. P. Kopia, and R. W. Lawrence (1996), The Clouds and the Earth's Radiant Energy System (CERES) sensors and preflight calibration plans, *J. Atmos. Oceanic Tech., 13*, 300-313.

Li, J., W. P. Menzel, W. Zhang, F. Sun, T. J. Schmit, J. J. Gurka, and E. Weisz (2004), Synergistic use of MODIS and AIRS in a variational retrieval of cloud parameters, *J. Appl. Meteorol., 43*, 1619-1634.

Liou, K. N. (1986), Influence of cirrus clouds on weather and climate processes: A global perpective, *Mon. Wea. Rev.*, *114*, 1167-1199.

Liou, K. N. (2002), An introduction to atmospheric radiation, Academic Press, San Diego, CA.

Liou, K. N., and Y. Takano (1994), Light scattering by nonspherical particles: Remote sensing and climatic implications, *Atmos. Res., 31*, 271-298.

Loeb, N. G., S. Kato, K. Loukachine, and N. M. Smith (2005), Angular distribution models for top-of-atmosphere radiative flux estimation from the clouds and the earth's radiant energy system instrument on the Terra satellite. Part I: Methodology, *J. Atmos. Oceanic Tech., 22*, 338-351.

Loeb N. G., K. Loukachine, N. Manalo-Smith, B. A. Wielicki, and D. F. Young (2003a), Angular distribution models for top-of-atmosphere radiative flux estimation from the clouds and the earth's radiant energy system instrument on the tropical rainfall measuring mission satellite. Part II: Validation. *J. Appl. Meteorol.*, *42*, 1748-1769.

Loeb, N. G., K. J. Priestley, D. P. Kratz, E. B. Geier, R. N. Green, B. A. Wielicki, P. O. Hinton, and S. K. Nolan (2001), Determination of unfiltered radiances from the clouds and the earth's radiant energy system instrument, *J. Appl. Meteorol., 40*, 822-835.

Loeb, N. G., N. M. Smith, S. Kato, W. F. Millfer, S. K. Gupta, P. Minnis, and B. A. Wielicki (2003b), Angular distribution models for top-of-atmosphere radiative flux estimation from the clouds and the earth's radiant energy system instrument on the tropical rainfall measuring mission satellite. Part I: Methodology, *J. Appl. Meteorol., 42*, 240-265.

Macke, A. and M. I. Mishchenko (1996), Applicability of regular particle shapes in light scattering calculations for atmospheric ice particles, *Appl. Opt., 35*, 4291-4296.

Mackowski, D. W. and M. I. Mishchenko (1996), Calculation of the T-matrix and the scattering matrix for ensembles of spheres, *J. Opt. Soc. Am. A 13*, 2266-2278.

Mackowski, D. W. (2002), Discrete dipole moment method for calculation of the T matrix for nonspherical particles, *J. Opt. Soc. Am. A 19*, 881-893.

Maltenfort, M. G. and T. M. Hamm (2004) Estimation of the electrical parameters of spinal motoneurons using impedance measurements, *J. Neurophysiol., 92*, 1433-1444.

Mather, J. H., T. P. Ackerman, M. P. Jensen, and W. E. Clements (1998), Characteristics of the atmospheric state and the surface radiation budget at the tropical western Pacific ARM site. *Geophys. Res. Lett., 25*, 4513-4516.

McFarquhar, G. M., A. J. Heymsfield, J. Spinhirne, and B. Hart (2000), Thin and subvisual tropopause tropical cirrus: observations and radiative impacts, *J. Atmos. Sci., 57*, 1841-1853.

Menzel, W. P., D. P. Wylie, and K. I. Strabala (1992), Seasonal and diurnal changes in cirrus clouds as seen in four years of observations with the VAS, *J. Appl. Meteor., 31*, 370-385.

Meyer, K., P. Yang, and B.-C. Gao (2004), Optical thickness of tropical cirrus clouds derived from the MODIS 0.66- and 1.375 channels, *IEEE. Trans. Geosci. Remote Sensing*, *42*, 833-841.

Minnis, P., K. N. Liou, and Y. Takano (1993a), Inference of cirrus cloud properties using satellite-observed visible and infrared radiances. Part I: Parameterization of radiance fields. *J. Atmos. Sci., 50*, 1279-1304.

Minnis, P., P. W. Heck, and D. F. Young (1993b), Inference of cirrus cloud properties using satellite-observed visible and infrared radiances. Part II: Verification of theoretical cirrus radiative properties. *J. Atmos. Sci., 50*, 1305-1322.

Minnis, P., D. F. Young, D. P. Kratz, J. A. Coakley, Jr., M. D. King, D. P. Garber, P. W. Heck, S. Mayor, and R. F. Arduini (1997), Clouds and the Earth's Radiant Energy System (CERES) Algorithm Theoretical Basis Document: Cloud Optical Property Retrieval (Subsystem 4.3), http://asd-www.larc.nasa.gov/ATBD/ATBD.html, 60 pp.

Minnis, P., D. F. Young, S. Sun-Mack, P. W. Heck, D. R. Doelling, and Q. Trepte (2003), CERES Cloud Property Retrievals from Imagers on *TRMM*, *Terra*, and Aqua, Proc. SPIE 10th International Symposium on Remote Sensing: Conference on Remote Sensing of Clouds and the Atmosphere VII, Barcelona, Spain, 8-12 September, 37-48.

Mishchenko, M. I. (1991), Light scattering by randomly oriented axially symmetric particles, *J. Opt. Soc. Am. A 8*, 871-882.

Mishchenko, M. I.,and L. D. Travis (1998), Capabilities and limitations of a current fortran implementation of the T-matrix method for randomly oriented, rotationally symmetric scatterers, *J. Quant. Spectrosc. Radiat. Transfer, 60*, 309-324.

Mishchenko, M. I. and L. D. Travis (1994), T-matrix computations of light scattering by large spheroidal particles, *Opt. Commun., 109*, 16-21.

Mitchell, D. L. (2002), Effective diameter in radiation transfer: General definition, applications, and limitations, *J. atmos. Sci, 59*, 2330-2346.

Mitchell, D. L., A. Macke, and Y. Liu (1996), Modeling cirrus clouds, II, Treatment of radiative properties, *J. Atmos. Sci. 53*, 2967-2988.

Mitchell, D. L. and W. P. Arnott (1994), A model prediction the evolution of ice particle size spectra and radiative properties of cirrus cloud: II. Dependence of absorption and extinction on ice crystal morphology, *J. Atmos. Sci. 51*, 817-832.

Moore, B., W. L. Gates, L. J. Mata, A. Underdal, and R. J. Stouffer (2001), Climate change 2001: The Scientific Basis, Contribution of Working group I to the Third Assessment Report of the Intergovernmental Panel on Climate Change, p. 769-785, Cambridge University Press, New York.

Nakajima, T., and M. D. King (1990), Determination of the optical thickness and effective particle radius of clouds from reflected solar radiation measurements. Part I: Theory, *J. Atmos. Sci., 47*, 1878-1893.

Nelder, J. A., R. Mead (1965), A simplex method for function minimization, *Computer journal, 7*, 308-313.

Niu, J., P. Yang, H,-L, Huang, J. E. Davies, J. Li, B. A. Baum, and Y. X. Hu (2006), A fast radiative transfer model for overlapping cloud (submitted to *J. Quant. Spectrosc. Radiat. Transfer*).

Pagano, T. S., H. H. Aumann, D. E. Hagan, and K. Overoye (2003), Prelaunch and in-flight radiometric calibration of the Atmospheric Infrared Sounder (AIRS), *IEEE Trans. Geosci. Remote Sensing, 41*, 265-273.

Platnick, S., M. D. King, S. A. Ackerman, W. P. Menzel, B. A. Baum J. C. Riedi, and R. A. Frey (2003), The MODIS cloud products: Algorithms and examples from Terra, *IEEE Trans. Geosci. Remote Sensing*, *41*, 459-473.

Prabhakara, C., D. P. Kratz, J. M. Yoo, G. Dalu, and A. Vernekar (1993), Optically thin cirrus clouds: Radiative impact on the warm pool, *J. Quant. Spectrosc. Radiat. Transfer*, *49*, 467-483.

Press, W. H., S. A. Teukolsky, W. T. Vetterling, and B. P. Flannery (1992), Numerical Recipes in Fortran 77, Cambridge University Press, Melbourne, Australia.

Roskovensky, J. K., and K. N. Liou (2003), Detection of thin cirrus from 1.38 μm / 0.65 μm reflectance ratio combined with 8.6-11 μm brightness temperature difference, *Geophys. Res. Lett., 30(19)*, 1985, doi:10.1029/2003GL018135.

Rossow, W. B., and R. A. Schiffer (1999), Advances in understanding clouds from ISCCP, *Bull. Am. Meteorol. Soc.*, *80*, 2261-2287.

Rothman, L. S., C. P. Rinsland, A. Goldman, S. T. Massie, D. P. Edwards, J. -M. Flaud, A. Perrin, C. Camy-Peyret, V. Dana, J. -Y. Mandin, J. Schroeder, A. McCann, R. R. Gamache, R. B. Wattson, K. Yoshino, K. V. Chance, K. W. Jucks, L. R. Brown, V. Nemtchinov, and P. Varanasi (1998), The HITRAN Molecular Spectroscopic Database and HAWKS (HITRAN Atmospheric Workstation): 1997 edition, *J. Quant. Spectrosc. Radiat. Transfer, 60*, 665-710.

Sassen, K., M. K. Griffin, and G. C. Dodd (1989), Optical scattering and microphysical properties of subvisual cirrus clouds and climatic implications, *J. Appl. Meteorol., 28*, 91-98.

Sherlock, V., A. Collard, S Hannon, and R. Saunders (2003), The Gastropod fast radiative transfer model for advanced infrared sounders and characterization of its errors for radiance assimilation, *J. Appl. Meteorol., 42*, 1731-1747.

Sinha, A., and K. P. Shine (1995), Simulated sensitivity of the earth's radiation budget to changes in cloud properties, *Quart. J. Roy. Meteor. Soc.*, 121, 797-819.

Smith, G. L., N. Manalo-Smith, L. M. Avis (1994), Limb-darkening models from along-track operation of the ERBE scanning radiometer, *J. Appl. Meteorol., 33*, 74-84.

Smith, G. L., B. A. Wielicki, B. R. Barkstrom, R. B. Lee, K. J. Priestly, T. P. Charlock, P. Minnis, D. P. Kratz, N. Loeb, and D. F. Young (2004), Clouds and earth radiant system: an overview, *Adv. Space Res., 33*, 1125-1131.

Smith, W. L., H. M. Woolf, P. G. Abel, C. M. Hayden, M. Chalfant and N. Grody (1974), Nimbus 5 sounder data processing system Part I: Measurement characteristics and data reduction procedures, NOAA Tech. Memo., NESS 57, 99pp.

Stamnes, K., S. C. Tsay, W. Wiscombe, and K. Jayaweera (1988), A numerically stable algorithm for discrete-ordinate-method radiative transfer in multiple scattering and emitting layered media, *Appl. Opt., 27*, 2502-2509.

Stephens, G. L., and P. J. Webster (1981), Clouds and climate: Sensitivity of simple systems, *J. Atmos. Sci., 38*, 235-247.

Stephens, G. L., S. C. Tsay, J. P. W. Stackhouse, and P. Flatau (1990), The relevance of the microphysical and radiative properties of cirrus clouds to climate and climatic feedback, *J. Atmos. Sci., 47*, 1742-1753.

Strow, L. L., S. E. Hannon, S. De Souza-Machado, H. E. Motteler, and D. Tobin (2003a), An overview of the AIRS radiative transfer model, *IEEE Trans. Geosci. Remote Sensing*, *41*, 303-313.

Strow, L. L., S. E. Hannon, M. Weiler, K. Overoye, S. L. Gaiser, and H. H. Aumann (2003b), Prelaunch spectral calibration of the Atmospheric Infrared Sounder (AIRS), *IEEE Trans. Geosci. Remote Sensing*, *41*, 274-286.

Stubenrauch, C. J., A. D. Del Genio, and W. B. Rossow (1997), Implementation of subgrid cloud vertical structure inside a global circulation model and its effect on the radiation budget, *J. Climate*, *10*, 273-287.

Susskind, J., C. D. Barnet, and J. M. Blaisdell (2003), Retrieval of atmospheric and surface parameters from AIRS/AMSI/HSB data in the presence of clouds, *IEEE Trans. Geosci. Remote Sensing*, *41*, 390-183.

Szczodrak, M., P. J. Minnett, N. R. Nalli, and W. F. Feltz (2005), Measurement of temperature and humidity profiles over the ocean: Comparisons of AIRS retrievals with ship-based remote sensing, in situ measurements and ECMWF analysis, *J. Geophys. Res.,* (submitted).

Taflove, A. (1995), Computational Electrodynamics: The Finite-Difference Time-Domain Method, Artech House, Boston.

Takano, Y. and K. N. Liou (1989a), Radiative transfer in cirrus clouds. II. Theory and computation of multiple scattering in an anisotropic medium, *J. Atmos. Sci., 46*, 20-36.

Takano, Y. and K. N. Liou (1989b), Solar radiative transfer in cirrus clouds. Part I: single-scattering and optical properties of hexagonal ice crystals, *J. Atmos. Sci., 46*, 3-19.

Tian, B., B. J. Soden, and X. Wu (2004), Diurnal cycle of convection, clouds, and water vapor in the tropical upper troposphere: Satellites versus a general circulation model, *J. Geophys. Res., 109*, D10101, doi:10.1029/2003JD004117.

Tobin, D. C., F. A. Best, P. D. Brown, S. A. Clough, R. G. Dedecker, R. G. Ellingson, R. K. Garcia, H. B. Howell, R. O. Knuteson, E. J. Mlawer, H. E. Revercomb, J. F. Short, P. F. W. van Delst, and V. P. Walden (1999), Downwelling spectral radiance observations at the SHEBA ice station: Water vapor continuum measurements from 17 to 26 μm, *J. Geophys. Res., 104*, 2081-2092.

Trepte, Q., Y. Chen, S. Sun-Mack, P. Minnis, D. F. Young, B. A. Baum, and P. W. Heck (1999), Scene identification for the CERES cloud analysis subsystem, paper presented at the American Meteorological Society 10th Conference on Atmospheric Radiance, Madison, WI., 28 June - 2 July, 169-172.

Turner, D. D., S. A. Ackerman, B. A. Baum, H. E. Revercomb, and P. Yang (2003), Cloud phase determination using ground-based AERI observationat SHEBA, *J. Appl. Meteorol, 42*, 701-715.

Wang, P.-H., M.P. McCormick, L. R. Poole, W. P. Chu, G. K. Yue, G. S. Kent, and K. M. Skeens (1994), Tropical high cloud characteristics derived from SAGE II extinction measurements, *Atmos. Res., 34*, 53-83.

Warren, S. G. (1984), Optical constants of ice from the ultraviolet to the microwave, *Appl. Opt.*, *23*, 1206-1225.

Waterman, P. C. (1965), Matrix formulation of lectromagnetic scattering, *Proc. IEEE 53*, 805-812.

Wei, H., P. Yang, J. Li, B. A. Baum, H.-L. Huang, S. Platnick, Y. Hu, and L. Strow (2004), Retrieval of semitransparent ice cloud optical thickness from Atmospheric Infrared Sounder (AIRS) measurements, *IEEE Trans. Geosci. Remote Sensing, 42,* 2254-2267.

Wielicki, B. A., B. R. Barkstrom, E. F. Harrison, R. B. Lee III, G. L. Smith, and J. E. Cooper (1996), Clouds and the earth's radiant energy system (CERES): An earth observing system experiment, *Bull. Am. Meteorol. Soc., 77*, 853-868.

Wilber, A. C., D. P. Kratz, and S. K. Gupta (1999), Surface emissivity maps for use in satellite retrievals of longwave radiation, NASA/TP-1999-209362, NASA, Washington, DC, 35 pp.

Winker, D. M., and C. R. Trepte (1998), Laminar cirrus observed near the tropical tropopause by LITE, *Geophys. Res. Lett., 25*, 3351-3354.

Wiscombe, W. J., and A. Mugnai (1986), Scattering from nonspherical Chebyshev particles. 2: Means of angular scattering patterns, *Appl. Opt. 27*, 2405-2421.

Wriedt, T., and A. Doicu (1998), Formulations of the extended boundary condition method for three-dimensional scattering using the method of discrete sources, *J. Mod. Opt., 45*, 199-213.

Wylie, D. P., and W. P. Menzel (1989), Two years of cloud cover statistics using VAS, *J. Climate*, *2*, 380-392.

Wylie, D. P., and W. P. Menzel (1999), Eight years of high cloud statistics using HIRS, *J. Climate*, *12*, 170-184.

Xu, L., J. Ding, and A. Cheng (2002), Scattering matrix of infrared radiation by ice finite circular cylinders, *Appl. Opt., 41*, 2333-2348.

Yang, P., B. A. Baum, A. J. Heymsfield, Y. X. Hu, H.-L. Huang, S.-C. Tsay, S. Ackerman (2003a), Single-scattering properties of droxtals, *J. Quant. Spectrosc. Radiat. Transfer, 79-80*, 1159-1169.

Yang, P., B.A. Baum, H.-L. Huang, S. Platnick, Y. X. Hu, D. M. Winker, A. J. Baran, and P. N. Francis (2002), Single and multiple scattering/absorption properties of pristine ice crystals and polycrystals in the terrestrial window region, paper presented at the Sixth Conference on Light Scattering by Nonspherical Particles, Gainesville, FL., 4-10 March, 369-372.

Yang, P., B. C. Gao, B. A. Baum, Y. X. Hu, W. J. Wiscombe, S. C. Tsay, D. M. Winker, and S. L. Nasiri (2001), Radiative properties of cirrus clouds in the infrared (8-13μm) spectral region, *J. Quant. Spectrosc. Radiat. Transfer, 70*, 473-504.

Yang, P. and K. N. Liou (1998), Single-scattering properties of complex ice crystals in terrestrial atmosphere, *Contr. Atmos. Phys., 71*, 223-248.

Yang, P., K. N. Liou, and W. P. Arnott (1997), Extinction efficiency and single-scattering albedo of ice crystals in laboratory and natural cirrus clouds, *J. Geophys. Res., 102*, 21825-21835.

Yang, P., M. G. Mlynczak, H, Wei, D. P. Kratz, B. A. Baum, Y. X. Hu, W. J. Wiscombe, A. Heidinger, and M. I. Mishchenko (2003b), Spectral signature of ice clouds in the far-infrared region: Single-scattering calculations and radiative sensitivity study, *J. Geophys. Res., 108(D108)*, 4569, doi:10.1029/2002JD003291.

Yang, P., H. Wei, H.-L. Haung, B. A. Baum, Y. X. Hu, G. W. Kattawar, M. I. Mishchenko, and Q. Fu (2005), Scattering and absorption property database for nonspherical ice particles in the near- through far-infrared spectral region, *Appl. Opt. 44*, 5512-5523.

Zhang, Z. B., P. Yang, G. W. Kattawar, S.-C. Tsay, B. A. Baum, Y. X. Hu, A. J. Heymsfield, and J. Reichardt (2004), Geometric optics solution to light scattering by droxtal ice crystals, *Appl. Opt., 43*, 2490-2499.

VITA

Yong-Keun Lee received a bachelor degree in Atmospheric Sciences from Seoul National University, Seoul, Korea in February 1994. He continued to study in Seoul National University until February 1996 when he received a master's degree in Atmospheric Sciences.

Mr. Lee entered the Ph. D. program in the Department of Atmospheric Sciences at Texas A&M University in January 2002, and received a Ph. D. degree in August 2006.

Mr. Lee can be reached by email at yklee0305@hanmail.net, or by contacting Dr. Ping Yang at pyang@ariel.met.tamu.edu in Department of Atmospheric Sciences, Texas A&M University.